San Diego, April 12, 2018

Author response to the reviewers' comments on "The influence of layering and barometric pumping on firn air transport in a 2D model"

We would like to thank Stephen Drake and an anonymous reviewer for their detailed and insightful comments on our manuscript. Reviewer comments are shown in red below, with our responses in black. We have revised the manuscript following their advice and present a marked-up version of the manuscript and supplementary information at the end of this document.

Best regards,
Benjamin Birner, Christo Buizert, Till Wagner and Jeff Severinghaus

Changes to the model
A minor numerical mistake in the spacing of layers (layers were separated by slightly more than 1 annual layer thickness) was corrected. The amplitude of surface pressure variability in the model was changed to accurately reflect the time step dependence of the pressure forcing and the attenuation of the amplitude f barometric pumping in the model was removed. These corrections mostly compensate each other.
The modifications implemented did not change any of our results appreciably, but all figures were updated in the text.

First reviewer, Stephen Drake

Overview
This manuscript addresses firn air mixing stimulated by barometric pumping. The authors have developed a 2D model that simulates advection, convection, dispersion, and diffusion of air through firn that has discontinuous, low-permeability layers. They apply this model to investigate the relative impacts of diffusion and dispersion with depth for several noble gas isotopologues. Improved understanding of firn air mixing will enable more accurate assessments of ancient atmospheric composition and climate change chronology derived from firn and ice cores.
I recommend this manuscript for publication once the following items have been addressed.

General Comments
A result of Buizert and Severinghaus (2016) is that pressure changes above the snowpack manifest with full amplitude down to the lock-in zone after ~ 1 hr. This one hour timescale means that mesoscale and diurnal pressure variations may also influence firn air mixing. Synoptic pressure changes have more spectral power than mesoscale and diurnal pressure changes, however, mesoscale and diurnal pressure changes are more frequent. So, there is an interplay between frequency and amplitude that was not addressed in either this manuscript or in Buizert and Severinghaus (2016). Also, it is relevant to note that synoptic pressure changes do not always yield storms. These complicating factors perhaps would have been better addressed in Buizert and Severinghaus (2016). I leave it to the editor to decide whether they should be addressed in this (already substantial) manuscript.

We agree with the reviewer that there is a complex interplay between frequency and amplitude that controls barometric pumping in firn. The rate of change in surface pressure determines the airflow velocity in firn and therefore the resulting dispersive mixing. Fast flows can be induced by rapid pressure variations of small amplitude or by slower changes with larger amplitude. In addition, the frequency-dependent attenuation of pressure waves with depth further complicate the situation. This is illustrated by the surface mixed zone (also called the "convective zone") where pressure variability on short time scales makes an appreciable contribution to mixing and reduces gravitational fractionation but the vertical extent of this region is limited. Unfortunately, our model cannot resolve pressure variability on such short time scales due to computational constraints. Thus, we believe that the role of mesoscale and diurnal pressure changes is beyond the scope of this study and would better be addressed in separate publication. Note that Buizert and Severinghaus (2016) in fact used 6h resolution data surface pressure forcing for their 1D model, so that in principle diurnal pressure variability should have been accounted for.

The authors did not attempt to assess the error that could be attributed to barometric pumping when dating the composition of the atmosphere using ice cores. It would be instructive to a broader audience if they speculate as to what other information is needed to bound this problem.
We thank the reviewer for raising this point. Barometric pumping typically causes deviations from gravitational equilibrium that are orders of magnitude smaller than the analytical precision of CO_2 and CH_4 measurements. We therefore assume that the effect of barometric pumping on these records may safely be neglected and is not discussed in the text. Barometric pumping could reduce $\delta^{15}N$ below the gravitational equilibrium by a small amount; $\delta^{15}N$ is commonly used to infer gas age-ice age differences. In that sense it may influence the dating. However, in most sites this $\delta^{15}N$ effect is very small, certainly much smaller than other uncertainties such as the past thickness of the surface mixed zone.

Clarity
Overuse of "here" especially to begin a sentence.
Thank you. The use of "here" was considerably reduced.

It would be helpful if, rather than intermixing "impermeable" and "(near-) impermeable", the authors choose one term, define its meaning in the introduction and use it throughout the text (with the exception of the references to model layers, which are explicitly and accurately defined as impermeable).
We now use the terminology "reduced permeability" to describe the influence of layers in nature and reserve the term "impermeable" for layers in the model realm. Details on the numerical implementation of layers may be found in the Supplementary Information (SI).

Throughout most of the manuscript, the vertical dimension is referred to as "depth". But on pages 14 and 15 it is referred to as "height". I prefer that they use "depth" throughout.
"Height" was replaced by "depth".

The authors and others have demonstrated that interstitial air mixing near the snow surface is driven both convectively (by temperature gradients) and dynamically (through pressure changes). This is an opportunity to rename the upper layer as a "mixed" zone (or some-such) rather than "convective" zone so as not to perpetuate the overly simplistic convective zone terminology.
We thank the reviewer for this comment and fully agree. We renamed the "convective zone" to "surface mixed zone" throughout the manuscript to highlight this important dual nature of mixing in the near-surface region. A brief rational for this change was added to the introduction.

It is easier to parse the history of scientific discovery when multiple references are listed chronologically in the manuscript.

References are now in chronological order. Reordering of references is not highlighted in the attached marked-up version of the document to maintain easy readability.

Specific Comments

Page 1
Line 9: "impermeable" do you mean low permeability?
Yes (manuscript corrected).

Line 16: "Moreover, we find that…" This is a confusing sentence, consider re-wording. Do you mean: As observed in nature, simulated barometric pumping does not substantially change the differential fractionation of fast and slow moving gases?
There is little impact of barometric pumping on the differential fractionation of fast and slow-moving gases in our model. However, this modelling result does not agree with some preliminary observations from 5 different Antarctic ice coring sites which indicate that there is a coherent correlation between the amplitude of pressure variability at a site and the measured krypton excess (Buizert, unpublished). The sentence was restructured to better reflect this connection.

Line 18: "This suggests that…" what is "This" ?
We mean the shortcoming of the model described in the previous sentence (see comment above).

Page 2
Figure 1: consider brightening/enhancing this image so the layers are easier to distinguish
The contrast of the image was improved.

Page 3
Line 11: "…smoothing out any concentration gradients…" As shown in Drake et al. (The Cryosphere, 2017) snow inhomogeneities provide preferred pathways for airflow. So, remove the "out any".
Done

Line 13: "Such convective mixing…" The authors are convolving convection with a non-convective pressure-driven process.
The sentence was changed to better reflect the distinction between the two processes.

Fig 2a: This idealized medium is not non-dispersive. The streamlines, as drawn, are not realistic. Airflow around one sphere has close to an equal chance of going around the next sphere on either side with the net effect that particles will spread out both in the streamwise and transverse directions.
That is correct. We have decided to remove the figure from the manuscript since the figure was previously published and we would like to shorten the overall length of the paper

Page 4
Line 3: Why do the pressure-induced air flows need to be fast? Are you suggesting turbulent mixing? How fast is fast?
Buizert and Severinghaus (2016) have demonstrated the fast propagation of pressure waves in firn returning the column to hydrostatic balance. These readjustment flows are fast compared to other air flows in firn (see Fig. 4 in the text) but generally <10^-4 m/s. Therefore, we do not expect to see turbulent mixing in the porous firn medium as the Reynolds number of the flow is very small (Re<<1).

Line 5: "…emergent macroscale phenomenon…" what is emergent about dispersion?

We appreciate that this was not fully clear. We are referring to dispersion emerging when you have interactions of the fluid with the porous medium. On scales smaller than the pore-scale, only advection and diffusion control tracer distributions.

Line 7: is dispersion added to the governing equation or is it rather not removed from a simplified form of the governing equation?
The full governing equation indeed should contain dispersion but traditionally this term has been neglected in firn. The text was changed accordingly.

Line 18: "…hindering effect…" how about "diminishing effects"?
Manuscript corrected.

Page 5
Line 10: "Most current 1D firn air models…" does Buizert et al. (2012) contain a review of other 1D firn air models?
Yes, Buizert et al. (2012) is a model intercomparison study and discusses different implementations of the lock-in zone in a range of firn air models.

Line 17: "…discontinuous layers of zero diffusivity and barometric pumping" how about, "…by barometric pumping and discontinuous layers that have nominal diffusivity"?
Thank you, we followed the reviewer's recommendation.

Line 21: "the driving force for gravitational settling is effectively zero during horizontal transport…" need to reword because the gravitational force is not zero regardless of horizontal transport.
We modified the sentence to "[…] vertical settling of isotopes is greatly reduced during horizontal transport along layers […]".

Page 6
It would be more complete to also define the term on the LHS of Eq (2).
The LHS terms is now included.

Fig 4c: Why is the maximum in barometric pumping at ~15m depth?
The amount of air displaced by barometric pumping decreases monotonically with depth in the firn column. However, if we scale velocity by the size of the pores (as shown in the figure), velocity becomes a function of volume transport and cross-sectional area (i.e., open porosity). The velocity per area is largest around 15 m depth because the firn is considerably more porous above and less total volume transport occurs in the regions below. Slower velocities in the top few meters of the firn correspond to more total volume transport but the transport is offset by higher porosity. We plot the velocity per area pore space as this velocity is responsible for causing dispersion.

Page 7
Line 5: "…assuming a constant snow and ice mass flux at all depths" How does this assumption bias your results (if at all)?
We assume that firn properties such as density, open porosity and accumulation are constant in time. Furthermore, we assume conservation of mass when snow accumulates. Therefore, a constant snow/ice mass flux and increasing firn density with depth implies decreases in the downward advection of firn (w_{firn}). This is a very common assumption in the firn air transport modelling community, and generally insufficient data on past conditions are available to deviate from it.

We expect that changes in accumulation and firn density on different time scales would modify the porosity and permeability of firn and change the vertical distance of (annual) layers. In fact, the difference in density between summer and winter ice is one observation that motivated the present study of layering in firn.

Page 8

Line 13: "…barometric pumping in the more tortuous, deep firn" barometric pumping occurs throughout the firn column, not just in deep firn

Correct. What we mean is that barometric pumping induces airflows throughout the firn column but the impact of barometric pumping on trace gas concertation profiles is most prominent near the surface and in the deep firn. Barometric pumping leads to substantial air exchange between the near-surface firn and the unfractionated atmosphere above. Additionally, in the deep firn, the dispersivity of the firn medium is considerably higher than in the shallower sections of the column, therefore barometric pumping yields the strong dispersive mixing in this region despite slower flow velocities. The sentence was changed to reflect this.

Page 9

Line 3: "…longitudinal to-flow and transverse to-flow" how about "streamwise and cross-stream"?

Based on our reading of the literature (e.g., Freeze and Cherry, 1979) "longitudinal" and "transverse to-flow" are the commonly used direction terms in the context of dispersion. We have decided to follow this convention.

Page 10

Line 5: Is there a quantifiable basis for the assumption of 10x difference between horizontal and vertical molecular diffusivities?

The reviewer raises an important point. The molecular diffusivity is determined by the tortuosity of firn at the subgrid scale and therefore obtained by tuning. Although it is clear that firn pores are better connected in the horizontal than vertical direction, selecting a factor of 10x difference between horizontal and vertical molecular diffusivities is a somewhat arbitrary choice.

As a sensitivity test, we repeated the numerical experiments with a modified version of the model in which we set this factor to 1x and reduced the horizontal width of impermeable layers by a factor of $\sqrt{10}\sim3.2$ to compensate for the reduction in effective vertical transport caused by changing horizontal diffusivity. This yields qualitatively similar results to previous model runs (Fig. RW1). The observed strength of barometric pumping is slightly reduced in these model runs because less air is forced to flow through the horizontal layers in response to surface pressure changes (barometric pumping flows through layers effectively scale with the area-integrated density change in the regions of the model below a layer).

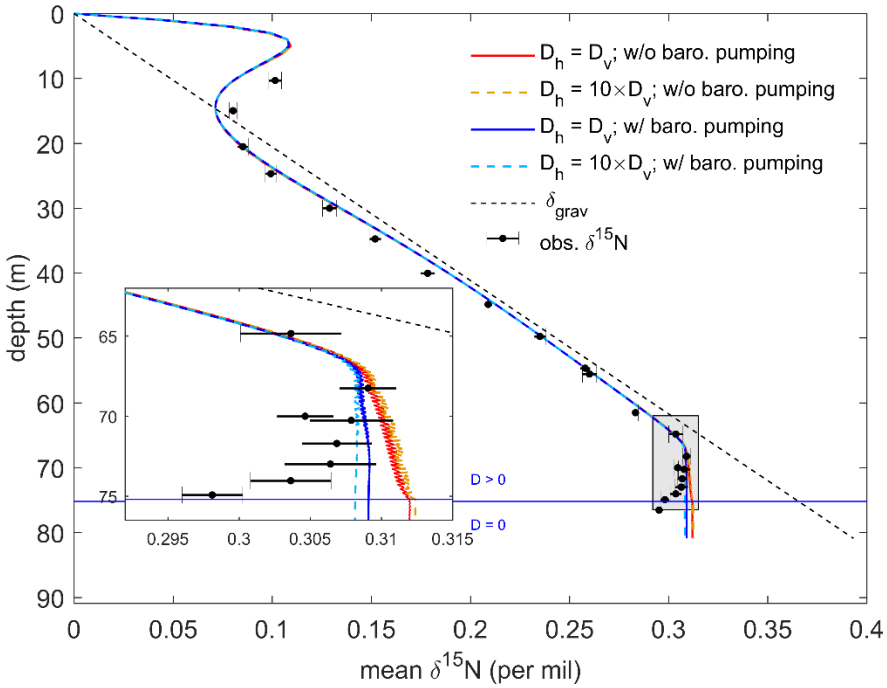

Figure RW1. $\delta^{15}N$ profiles simulated by the model with and without barometric pumping and different choices of horizontal diffusivity (D_h). The vertical diffusivities (D_v) remain identical, but the horizontal length of layers was scaled by a factor of $\sqrt{10}$~3.2 to compensate for differences in horizontal diffusivity.

Page 11

Fig 7. Comment on two CO2 (diamond) anomalies as it appears they are ignored in the curve fits.

Two samples at ~15 m and ~50 m depth were presumably contaminated with modern air based on high CO_2 and CH_4 and thus ignored in the curve fit. We have added a comment to the respective figure captions.

Page 12

Line 2: "In line with observations,…" the authors previously indicated an anthropogenic signal in CO2 and CH4 that could be repeated here for clarity

Thank you for this suggestion. The observed and simulated profiles are now explained in a little more detail.

Fig. 8: what do error bars with missing end caps mean relative to the error bars that have end caps?

This was simply a figure resolution problem in the pre-production document. All error bars should have end caps in all post-production, high-resolution images.

Page 14

Line 20: "A lack of alternative pathways" could be stated as "Fewer alternative pathways" or "Limited number of alternative pathways" or similar

The sentence was rephrased.

Line 32: If thermal effects are neglected then why is it called the convective zone? Perhaps rephrase sentences in lines 31 and 32.

The "convective zone" was renamed to "surface mixed zone" throughout the document.

Page 15

Line 11: "Constraining the convective zone… much larger than at the more recently sampled WAIS site." need citations

Citation for data added.

Page 16
Fig 11: Do the 2D simulations include impermeable layers? What is the meaning of missing error bar caps?
Both plotted simulations include impermeable layers. This has been clarified in the caption. Missing end caps on error bars were again an image resolution problem.

Page 17
Line 9: "Advection and mass-independent mixing…" is this the authors' theory or is a citation needed?
Citation added

Page 18
Line 7: "Therefore, ratios of heavier elements are more susceptible to kinetic fractionation." This sentence needs unpacking/rephrasing.
The sentence was rephrased.

Page 19
Eq 13: Since this is not strictly a Péclet number you could reference it as a modified (enhanced?, dispersive?) Péclet number.
We are now using the terminology of a "modified Péclet number" throughout the manuscript.

Page 20
Line 20: how are these values chosen?
These values approximately represent the present-day atmosphere. Since we report $\delta^{13}C$ values in the firn relative to the atmosphere, the choice of any constant atmospheric ratio does not influence our results.

Page 22
Lines 21-22: "Downward advection…" It should be clarified that these two sentences are based on previously reported results rather than new insights derived from this investigation. For example, "Previous studies (citations) have shown that…"
Citations were added.

Page 23
Line 2: explicitly specify the correction or explain the correction in more detail
The correction is outlined in more detail now and the total magnitude of the effect estimated following previously published methods (Bereiter et al., 2018).

Line 20: source for the solution found in Eq (A3) to Eq (A2)?
We added a more explicit statement of the boundary conditions but feel reluctant to include a full derivation of the solution in the manuscript since space is limited. The curious reader may verify the validity of the solution by plugging Eq. (A3) into Eq. (A2).

Page 24
Line 2: "Nevertheless…" Need citation or rationale for why Eq (A2) can be used to calculate $\delta^{15}N$
Thank you, an explanation is now included.

Technical Corrections
Page 1
Line 14: "supresses" → suppresses
corrected

Page 2
Line 2: “…unconsolidated snow…” I think of firn as consolidated snow.
corrected

Line 10: “processes which” → processes, which
sentence changed

Line 14: “high resolution” → high-resolution
corrected

Page 3
Line 15: remove “the same amount of”
corrected

Page 4
Line 1: “Last” → Lastly
corrected

Line 3: “gradients and induce” → gradients that induce
corrected

Line 17: “DZ but the effective” → DZ but effective
corrected

Page 9
Line 7: change “ becomes” to “simplifies to” (even though you already have “simplifies to” in the text just above)
corrected

Page 11
Line 6: “Kawamura (unpublished)”- might as well leave this out since you have another citation
corrected

Page 12
Line 4: “In the following we” → In the following discussion we
corrected

Page 13
Line 9: “Isotopes ratios are higher” → Simulated isotope ratios are higher
corrected

Page 15
Line 1: “the dispersivity” → dispersivity
corrected

Line 4: “estimate is within” → estimate of 2.8 m is within
corrected

Page 17
Line 17: "…2013)as" → …2013) as
corrected

Page 20
Line 13: "the isotopologues" → remove the "the"
corrected

Page 21
Line 20: "at WAIS Divide" → at the WAIS Divide
corrected

Line 23: "75.9% almost" → 75.9%, almost
corrected

Page 22
Line 22: remove the "This"
corrected

Line 23: remove "clearly"
corrected

Page 23
Line 1: "these relationships" → these scaling relationships
corrected

Page 26
Line 10: "Movment" → Movement
corrected

Line 11: "seperation" → separation
corrected

Technical Corrections for Supplement
Page 2
Line 2: "q is a Nx1 vectors" → q is an Nx1 vector
corrected

Line 5: "off diagonals" → off-diagonals
corrected

Page 5
Line 1: "at all depth" → at all depths
corrected

Page 4
Fig S3: Does this figure indicate that there is a ~35 year delay in the response of the $\delta^{15}N$ profile due to the 3-day time step relative to the 3 day/5 ~14 hr time step?
~35 years is the adjustment time scale of the deep firn, i.e., the time it takes to bring the firn back into steady state if the firn conditions are changed slightly. For the plot, the model is initialized with the WAIS Divide

isotope profile simulated for 2006 and run for another 50 years with a 5x shorter time step. Note that in the previous version of the manuscript there was a small numerical problem with this initialization that has now been corrected. After this correction was implemented, the error now remains smaller than 0.1 per meg (previously 0.5 per meg) and converges after ~15 years to a level where further increase becomes undetectable compared to the interannual variability seen in the plot.

Page 6
Line 3: "Eularian" → Eulerian
corrected

Page 9
Fig S6: "Plot is shown at reduced grid resolution for clarity." Is this plot in reduced grid resolution or is it a subset of the domain at the original resolution (or both)?
The plot shows a selected region in the lock-in zone. A problem with the x-tick labels was corrected and the caption edited for clarity.

Page 11
Note: there is a gap in the text partway down the page
corrected

Page 12
Line 4: "firnf"?
Corrected

Line 6: is there a reference for equation S28?
A reference was added.

Page 13
Line 1: "serval harmonic"?
Corrected to read "several harmonics"

Table S1: for the WAIS Divide the daily pressure change is 5hPa. Does this mean that for a 3-day time step the pressure change is 15hPa? Or is the 3-day pressure change no more than 15hPa and is quasi-randomly attenuated to match a red-shifted spectra? Or ?
The observed pressure variability at WAIS Divide is ~7hPa per day. (In the updated version of the model the amplitude attenuation was removed.) This forcing is implemented as random pressure changes every 3.5 days. The amplitude of this pressure variability must be increased by a factor of $\sqrt{\Delta t/day}$ to account for the longer time step of the model.

Second, anonymous review

General comments

The submitted manuscript analyses the influence of impermeable layer and barometric pumping (driven by surface pressure variability) on firn air transport using a 2D trace gas advection-diffusion-dispersion model accounting for discontinuous horizontal layers of reduced permeability. The simulated results are compared with field measurements from WAIS Divide and Law Dome DSSW20K and show good agreements.

Specific comments

The manuscript is well written and shows interesting results which are sufficient to be published. However, I would suggest to add some minor comments to make the manuscript clearer:

We thank the reviewer for the positive assessment of this study.

1. In the Figures, I would mention the time step you used for the plots. Are they consistent with the field measurements?

The time step for all model runs is 3.5 days unless otherwise noted owing to the high computational cost of running the 2D model. This is now mentioned in the main text. Sensitivity tests using a shorter time step are shown in the supplementary information.

2. In the 'supplementary information' you show a table with some simulation parameters, however some information is missing or is unclear, respectively. (e.g. simulation time, time range of the simulations, resolutions, etc.)

We agree that the table was not easily accessible. Item names in the table were edited for clarity (see also detailed comments below).

3. I would recommend to also show plots of the boundary conditions at the surface, like temperature, pressure, etc.

An exemplary time series of surface pressure fluctuations at WAIS Divide over the course of one year was added to the supplementary information.

We elect not to show a surface temperature history in the manuscript because we do not wish to suggest that our temperature histories are necessarily accurate reconstructions of past surface conditions at the site (shown here only for completeness). Our forcing histories are based on previously published temperature reconstructions (Dahl-Jensen et al., 1999; Van Ommen et al., 1999; Orsi et al., 2012) but adjusted slightly (in the case of WAIS Divide) to yield thermal gradients consistent with borehole temperature observations in our computationally simplified temperature model based on Alley and Koci, 1990 (Fig. RW2). Thermal diffusion only has a small effect on the simulated isotope profile below the surface mixed zone, therefore the details of the temperature forcing are mostly inconsequential.

Atmospheric CO_2 and CH_4 histories used to drive the model are presented in the supplementary information (Fig. S4).

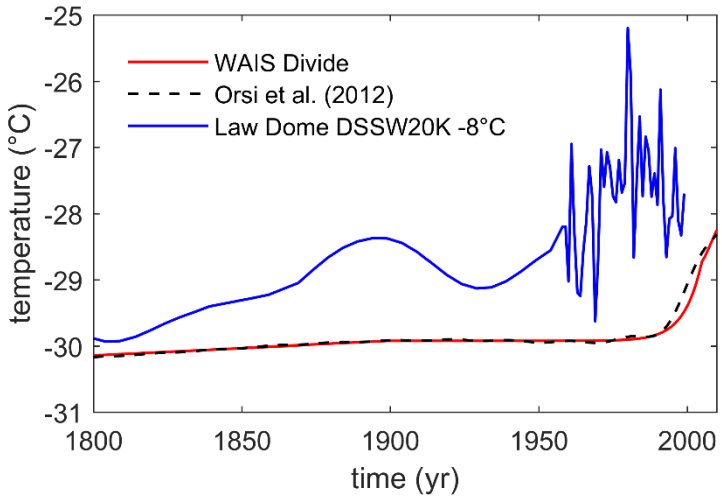

Figure RW2. Surface temperature forcing of the model at WAIS Divide and Law Dome DSSW20K (offset by -8°C) without the seasonal cycle component. Our forcing generally agrees well with the more robust surface temperature reconstruction for WAIS Divide by Orsi et al. 2012.

Detailed comments manuscript

Page 3, Line 5 – 6: I would recommend to make 'z', 'T', and 'R' italic to make it consistent.
Font changed to italic

Page 7, Line 2 – 3: Have you checked the influence of airflow due to temperature changes, especially in the convective zone? Normally, in the top 10-15 meters you have a high variation in the temperature profile due to the changing temperature at the top. This variation in the temperature profile can cause an airflow.
We do not explicitly simulate temperature-driven convection in the surface mixed zone. Instead, convection and wind-driven mixing is represented by mass-independent "eddy" mixing. This follows common practice in the firn modeling community.

Page 11, Line 4: '…assumed to be temperature independent if the temperature sensitivity is unknown.' → Where does this temperature sensitivity appear?
Omega is a function of temperature as described by eq. (11). The sentence was edited for clarity.

Page 11, Figure 7: There are two outliers in the observed CO2 concentrations at around 15 and 50 meters. Is there a reason for this?
These samples were likely contaminated with modern air before analysis and a comment on this issue has been added (see response to Review 1).

Page 11, Figure 7 caption: You refer to Fig. S9 to illustrate the differences in the CO2 and CH4 profiles between the 1D and the 2D model with or without barometric pumping which is not visible at the resolution of this Figure 7. However, Fig. S9 shows the same figure like Fig. 6 but only for Law Dome DSSW20K. Where can I find the Figure of the differences in the CO2 and CH4 profiles between the 1D and the 2D model with or without barometric pumping?
The Figure reference was changed to now correctly reference Figure S11 in the Supplementary Information (numbering of Figures changed).

Page 12, Line 10: See my comment to Page 11, Figure 7 caption.
corrected

Page 17, Line 13 – 14: What could be the reason that the simulated 86Kr excess is significant lower than the observed one?
In the discussion (section on the modified Péclet number), we explore the hypothesis that some unresolved subgrid-scale physics may be critical for obtaining larger ^{86}Kr excess. Alternatively, a different representation of the surface mixed zone could lead to larger ^{86}Kr excess simulated by the model than in the current setup. If the surface mixed zone was extended to great depth but the strength of mixing reduced to maintain agreement with the observed CO_2 profile, ^{86}Kr excess below the surface mixed zone would increase in the model for example (the dark gray area in Figure 14 would expand). The importance of correctly representing the surface mixed zone will need to be further explored elsewhere.

Page 18, Line 6 – 7: 'Heavy, slow-diffusing isotopes approach gravitational equilibrium more slowly than lighter, faster-diffusing isotopes.' -> Maybe it is a silly question but is it not the opposite around? If the isotopes are heavy you have a faster settlement due to stronger gravitational force?
The reviewer is correct in that, heavier isotopes are indeed more gravitationally fractionated than lighter isotopes in firn because they experience a larger gravitational pull; the gravitational enrichment scales linearly with the mass difference between isotopes. However, isotopes approach gravitational equilibrium by diffusion (molecular diffusion drives the system towards chemical equilibrium. In firn air transport, chemical equilibrium must include the potential energy associated with the gravitational field of Earth) and the diffusivity of a gas typically decreases with it molecular weight. Therefore, heavy isotopes approach gravitational equilibrium more slowly.

Page 22, Line 24: 'However, our experiments fail to …' -> Which experiments? I cannot see in your manuscript that you did experiments, just simulations.
Wording changed to "numerical experiments".

Page 24, Line 3 and 9: I think you want to refer to Eq. (A3) instead to Eq. (A4).
The text was changed accordingly.

Detailed comments supplementary information

Page 2, Equation S5: 'q' on the left-hand side of the equation is missing.
Corrected

Page 4, Line 15 – 20: Does it mean that snow accumulation is included?
Snow accumulation is constant in time and represented in the model as the vertical migration of the firn matrix including its gases and layers. Further details on the treatment of advection may be found in the SI.

Page 10, Line 4: How long does it take to run one simulation with time steps of around 3 days?
The runtime is approximately 2 days on 10 CPUs per simulation (with Δt = 3.5 days). A mention of this has been added.

Page 11, Section 'Thermal model': Can you show a figure of the temperature profile to get an impression of the boundary condition?
We added a borehole temperature profile with the simulated thermal gradient to the SI.

Page 11/12: The line break is wrong.
corrected

Page 12, Line 4: The line break is wrong and it should mean 'firn'
corrected

Page 12, Line 10: Please show a figure of the surface temperature histories.
See response to specific comments above.

Page 13, Table S1: Are the parameters the same for WAIS Divide and Law Dome DSSW20K if you only show one number, e.g. the 'Horizontal' or 'Vertical grid spacing'?
If only one number is show the value is the same for both sites. The table has been reformatted to clarify this.

Page 13, Table S1, Row 'Width': Does this mean there is a variation of the width? What are the exact values for WAIS Divide and Law Dome DSSW20K you used in the simulations?
The width of the model is different for each model to maintain a constant ratio between the thickness of annual layers and the width of the model. Exact values were added to the table.

Page 13, Table S1, Row 'Depth of first layer': Can you provide an exact value?
values added to table

Page 13, Table S1, Row 'Temperature': Did you use a fix temperature value at the top? No daily or seasonal variations?
The model includes anthropogenic warming and a seasonal temperature cycle (see SI Section 3). Diurnal temperature changes are neglected. The item in the table is the observed annual mean temperature at each site (item name corrected).

Page 13, Table S1, Row 'Surface Pressure: Did you use a fix pressure value at the top? No daily or seasonal variations?
Table S1 only provides the mean surface pressure and the daily variability of pressure at each location. A plot of surface pressure was added to the SI (Fig. S8) and the table item name edited for clarity.

Page 13, Table S1, Row 'Free air relative diffusivities to CO2': Can you show the value you cited from the Paper?
Because the model requires a considerable number of these free air diffusivity values, instead of reproducing them in the SI we now specifically reference the table in the original publication by Buizert et al. (2012).

Page 15, Line 5: '… using q-values.' -> please change it to '*q*-values'.
Manuscript corrected.

The influence of layering and barometric pumping on firn air transport in a 2D model

Benjamin Birner[1], Christo Buizert[2], Till J.W. ~~Wagner[1]~~ Wagner[3] and Jeffrey P. Severinghaus[1]

[1]Scripps Institution of Oceanography, University of California San Diego, La Jolla, CA 92093, USA
[2]College of Earth, Ocean and Atmospheric Sciences, Oregon State University, Corvallis, OR 97331, USA
[3]Department of Physics and Physical Oceanography, University of North Carolina at Wilmington, NC 28401, USA

Correspondence to: Benjamin Birner (bbirner@ucsd.edu)

Abstract. Ancient air trapped in ice core bubbles has been paramount to developing our understanding of past climate and atmospheric composition. Before air bubbles become isolated in ice, the atmospheric signal is altered in the firn column by transport processes such as advection and diffusion. However, the influence of low~~im~~ permeabi~~l~~le~~i~~ity layers and barometric pumping (driven by surface pressure variability) on firn air transport is not well understood and cannot be captured in conventional 1-dimensional firn air models. Here we present a 2-dimensional (2D) trace gas advection-diffusion-dispersion model that accounts for discontinuous horizontal layers of reduced permeability. We find that layering ~~and~~ or barometric pumping individually yield too small a reduction in gravitational settling to match observations. In contrast, ~~a combination of both effects more strongly supresses gravitational fractionation~~when both effects are active, the model's gravitational fractionation is suppressed as observed. Layering ~~locally~~ focuses airflows in certain regions in the 2D model ~~and thus~~which acts to ~~amplifies~~ amplify the dispersive mixing resulting from barometric pumping. Hence, the representation of both factors is needed to obtain a ~~more natural~~realistic emergence of the lock-in zone. ~~Moreover~~In contrast to expectations, we find that the addition of barometric pumping in the layered 2D model does not substantially change the differential kinetic fractionation of fast and slow diffusing trace gases~~, which is observed in nature~~. ~~This suggests~~However, like 1D models, the 2D model substantially underestimates the amount of differential kinetic fractionation seen in actual observations, suggesting that further subgrid-scale ~~physics~~ processes may be missing in the current generation of firn air transport models. ~~However~~In spite of this deficiency, we find robust scaling relationships between kinetic isotope fractionation of different noble gas isotope and elemental ratios. These relationships may be used to correct for kinetic fractionation in future high precision ice core studies and can amount to a bias of up to 0.45 °C in noble gas based mean ocean temperature reconstructions at WAIS Divide, Antarctica.

1 Introduction

In the upper 50-130 m of ~~un~~consolidated snow above an ice sheet, known as the firn layer, atmospheric gases gradually become ~~gradually~~ entrapped in ~~secluded~~ occluded pores and are eventually preserved as bubbles in the ice below. Antarctic ice core records containing these trapped gases have been critical in informing our understanding of the interplay of past climate and atmospheric trace gas variability over the past 800,000 years (Petit et al., 1999; Lüthi et al., 2008). As atmospheric gases migrate through the firn, they are modified in elemental composition and isotopic signatures~~composition~~ by several competing physical processes~~ which may alter elemental concentrations and isotopic signatures~~ (Schwander et al., 1988, 1993; Trudinger et al., 1997; Buizert et al., 2012; Kawamura et al., 2013; Mitchell et al., 2015). Therefore, appropriate corrections must be applied to firn and ice core records to accurately reconstruct atmospheric trace gas histories.

Box 1| Porous media terminology

Porosity: the fraction of (firn) volume filled by gas

Permeability: the degree to which a porous medium permits viscous flow to pass through

Fickian diffusion: molecular diffusion that is proportional to the concentration gradient as described by Fick's first law

Tortuosity: measure of the twistedness of pathways through a porous medium

Firn is a layered medium, in which the denser layers can impede vertical diffusion and transport~~Abundant evidence shows from field observations, high-resolution firn density measurements, and comparisons of summer and winter ice, that (near-) impermeable horizontal layers exist in polar firn~~ (Hörhold et al., 2012; Mitchell et al., 2015; Orsi et al., 2015) (Fig. 1). The~~ir~~ significance of these layers for firn gas transport remains unclear and motivates this work. Readers who are familiar with the structure of firn and its air transport processes may wish to skip ahead to the last paragraph of this section. To build some intuition about firn transport processes, a simple analytical model of firn air transport is provided in Appendix A.

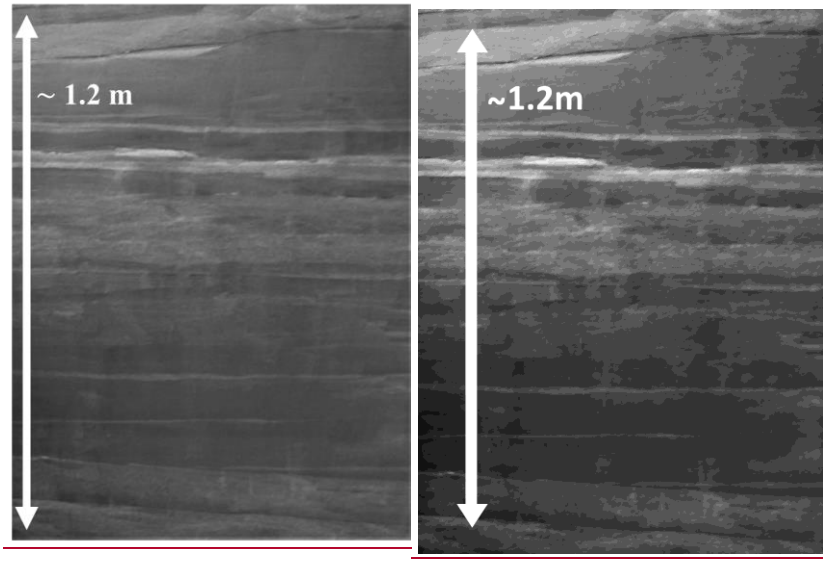

Figure 1. Layering of firn photographed in a surface pit at WAIS Divide. Image courtesy of Anaïs Orsi.

We distinguish four main processes affecting the composition of air in firn: diffusion, advection, dispersion and convective mixing. Molecular ~~Fickian d~~diffusion, driven by concentration gradients in the firn, is the primary mode of horizontal and vertical transport. Molecular diffusion also enables gravitational fractionation, or "settling", of trace gases in proportion to their masses (Schwander, 1989; Sowers et al., 1989; Schwander et al., 1993; Trudinger et al., 1997). Gravitational settling leads to an enrichment of heavy isotopes with depth that is described in equilibrium by the barometric equation (Schwander, 1989; Sowers et al., 1989; Craig et al., 1988):

$$\delta_{grav} = \left[\exp\left(\frac{g\Delta m}{R\,T} z\right) - 1\right] \times 1000\ ‰, \quad (1)$$

where $\delta \equiv \frac{r_{sample}}{r_{standard}} - 1 \equiv q - 1$, with r being~~is~~ the isotope ratio (unitless), z the depth (m), T the absolute temperature (K), Δm the isotope mass difference (kg mol^{-1}), g the gravitational acceleration (m s^{-2}), and R the fundamental gas constant (J mol^{-1} K^{-1}).

Gradual accumulation of snow and air bubble trapping leads to a slow, downward advection of the enclosed air. The net air advection velocity is slower than the snow accumulation rate (yet still downward in the horizontal average in an Eulerian framework) because compression of the porous firn medium produces a ~~return~~ flow of air ~~from the firn column to the atmosphere~~upward relative to the firn matrix (Rommelaere et al., 1997).

Buoyancy-driven convection and brief pressure anomalies associated with wind blowing over an irregular topography cause strong mixing between the near-surface firn and the unfractionated atmosphere, smoothing ~~out any~~ concentration gradients (Colbeck, 1989; Severinghaus et al., 2010; Kawamura et al., 2013). This mixing ~~Such convective mixing is usually observed only in the top few meters of the firn column. Convective mixing~~ causes ~~a~~ substantial deviations from the gravitational settling equilibrium (i.e., the solution to Eq. (1)) and leads to varying degrees of kinetic isotope fractionation because faster diffusing isotopes more ~~easily overcome the same amount of mass-independent mixing~~readily return to thermal-gravitational equilibrium by diffusion (Buizert et al., 2012; Kawamura et al., 2013).

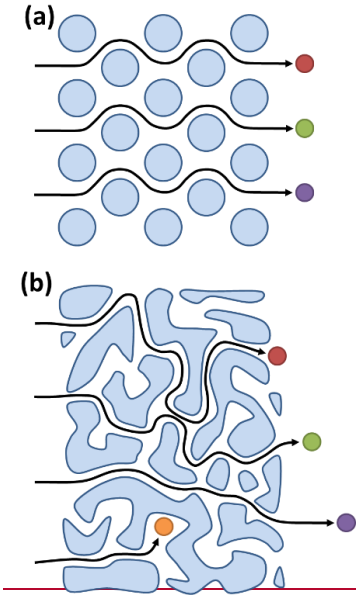

Figure 2. Schematic of (a) a non-dispersive medium and (b) a highly dispersive medium such as the deep firn. Figure reproduced from Buizert and Severinghaus, (2016).

Lastly, surface barometric pressure variability on longer timescales (> 1 hour) drives air movement down to the firn-ice transition. Building on work by Schwander et al. (1988), Buizert and Severinghaus (2016) suggest that migrating storm centressurface pressure variability may produce significant pressure gradients in the firn thatand induce fast airflows in firn. Porous firn has a high tortuosity, i.e., two points are typically connected by strongly curved paths, and the deep firn also contains many cul-de-sacs (Buizert and Severinghaus (2016), their Fig. 2)(Fig. 2). Airflow through such a medium produces mass-independent, dispersive mixing. Dispersion in this context is an emergent macroscopic phenomenon that describes microscopic velocity deviations of the flow from Darcy's law of bulk fluid flow through porous mediain different pores (Buizert and Severinghaus, 2016). This process may be accounted for by adding additional a dispersive mixing termon to the governing advection-diffusion equation traditionally used for of trace gas transport in firn (e.g., Buizert and Severinghaus, 2016).

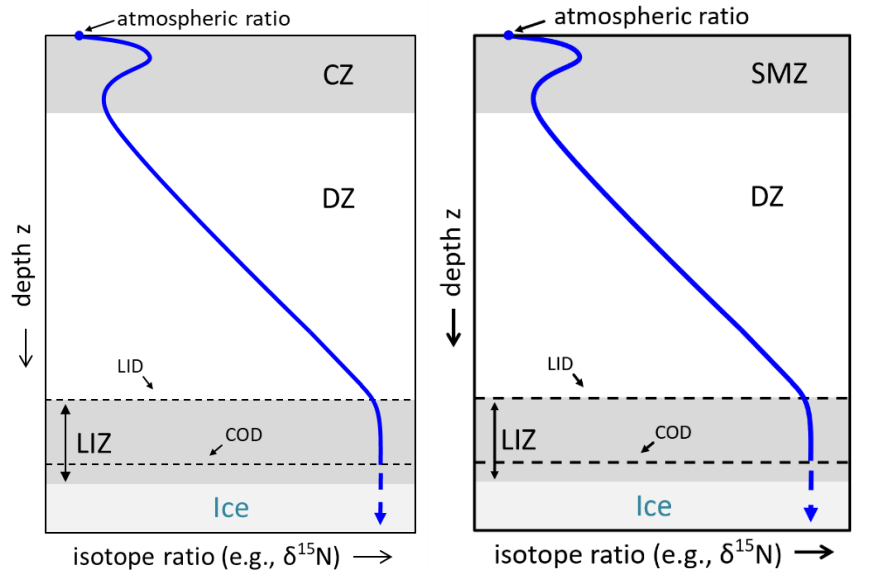

Figure 2~~3~~. Schematic depiction of a typical isotope profile. The ~~convective~~ surface mixed zone (~~CZ~~SMZ), the diffusive zone (DZ), the lock-in zone (LIZ) and the ice below are indicated by shading. Further indicated are the lock-in depth (LID) and the close-off depth (COD) (see text).

Together, these four processes yield a firn column that is ~~typically~~ split into a ~~convective~~ surface mixed zone (~~CZ~~SMZ, which has historically been labelled the convective zone), a diffusive zone (DZ) and a lock-in zone (LIZ) (Fig. 2~~3~~). The close-off depth (COD) occurs where the air content becomes fixed and pressure in open porosity increases above hydrostatic pressure. We prefer the term "surface mixed zone" over the more commonly used terminology "convective zone" to acknowledge the dual nature of mixing driven by convection and high-frequency pressure variability in this region. The SMZ~~CZ~~ is rather well-mixed with a trace gas composition similar to the atmosphere. Nevertheless, large seasonal thermal gradients can lead to isotopic fractionation which is only partially attenuated ~~by convective mixing~~ (Severinghaus et al., 2001, 2010; Kawamura et al., 2013). Molecular diffusion dominates in the DZ but ~~the~~ effective firn diffusivity decreases with depth ~~to represent~~due to the ~~hindering~~ increasing influence~~effect~~ of tortuosity ~~on~~ hindering diffusion. Throughout the DZ, gravitational settling leads to an enrichment of all isotopes heavier than air in proportion to their mass difference. The top of the LIZ, the somewhat ~~ill-~~poorly defined lock-in depth (LID) horizon, is commonly deduced from a rather sudden change in the slope of the $\delta^{15}N$, CO_2 or CH_4 profiles. Gravitational enrichment of isotopes ceases in the LIZ and isotope ratios remain constant with depth. We term any such deviation from gravitational equilibrium "disequilibrium" (without implying that such a situation is not in steady-state).

The physical mechanism responsible for the cessation of gravitational enrichment in the deep firn is still not fully understood. Since CFCs and other anthropogenic tracers have been detected in firn air measurements from the LIZ well below the depth expected from pure advection, it is clear that some amount of vertical transport by molecular diffusion or dispersion continues in the LIZ (Severinghaus et al., 2010; Buizert et al., 2012; Buizert and Severinghaus, 2016). However, no further

gravitational settling of isotopes occurs in the LIZ as indicated by constant $\delta^{15}N$ values. Furthermore, the vertical transport in the LIZ appears to be at least to some degree mass- and diffusivity-dependent ~~because~~ since the faster diffusing CH_4 advances further in the LIZ than the slower diffusing gases CFC-113 or CO_2 (Buizert et al., 2012). Therefore, transport in the LIZ cannot be explained by either mass-indiscriminate dispersive mixing or molecular diffusion alone. Most current 1D firn air models use a greatly reduced molecular diffusivity in the lock-in zone and simultaneously introduce a mass-independent mixing term tuned to match measured trace gas profiles (Buizert et al., 2012). A physical mechanism to justify these numerical methods remains elusive. An attempt at a physical explanation was given by Buizert and Severinghaus (2016), who ~~Buizert and Severinghaus (2016)~~ introduced barometric pumping in a 1D firn model. ~~The authors observed a significant effect of barometric pumping on the $\delta^{15}N$ profile but needed to invoke a highly idealized parametrization of firn layering to match observations due to the intrinsic difficulties of representing layers in 1D.~~

Here, we explore the possibility that non-fractionating trace gas mixing in deep firn may be explained by the combination of barometric pumping and discontinuous horizontal layers that have nominal diffusivity~~by discontinuous layers of zero diffusivity and barometric pumping~~. High density layers are empirically linked to low vertical permeability (and thus diffusivity),~~porosity, diffusivity and permeability,~~ increasing the firn's tortuosity and forcing extensive horizontal transport. The influence of layering ~~and horizontal inhomogeneity~~ on firn gas transport is mostly untested in numerical models so far since previous firn air models were generally limited to one dimension. In particular, we will test two mechanisms by which density layering could influence isotope ratios in firn air: (i) Layering may ~~(i)~~ reduce gravitational settling of isotopes because ~~the driving force for gravitational settling is effectively zero~~vertical settling of isotopes is absent during horizontal transport along layers; (ii) L~~and l~~ayering may ~~(ii)~~ modulate the mass-independent dispersive mixing effect of barometric pumping. Our analyses will focus on two Antarctic high-accumulation sites, WAIS Divide and Law Dome DSSW20K (Trudinger et al., 2002; Battle et al., 2011).

2 Methods

2.1 Governing equation and firn properties

We model 2D trace gas transport in firn ~~is simulated~~ by numerically solving the advection-diffusion-dispersion equation, known from hydrology (Freeze and Cherry, 1979), adapted to firn (following Schwander et al., 1993; Rommelaere et al., 1997; Trudinger et al., 1997; Severinghaus et al., 2010; Buizert et al., 2012; Kawamura et al., 2013;Buizert and Severinghaus, 2016),

$$\tilde{s}\frac{\partial q}{\partial t} = \vec{\nabla}\cdot\left[\tilde{s}\boldsymbol{D}_m\left(\vec{\nabla}q - \frac{\Delta m\,\vec{g}}{R\,T}\,q + \Omega\frac{\partial T}{\partial z}q\,\hat{k}\right) + \tilde{s}\boldsymbol{D}_d\vec{\nabla}q\right] - (\tilde{s}\,\vec{u})\cdot\vec{\nabla}q \qquad (2)$$

with $q \equiv \delta + 1$ the ratio of any isotope to $^{28}N_2$ compared to a standard material, $\tilde{s} \equiv s_{op}\exp\left(\frac{\Delta mgz}{RT}\right)$ the pressure-corrected open porosity ($m^3\ m^{-3}$), T temperature (K), Ω thermal diffusion sensitivity (K^{-1}), and $\vec{u}$ the advection velocity ($m\ s^{-1}$). $\boldsymbol{D}_m$ and

$\boldsymbol{D}_d$ are the 2D molecular diffusion and dispersion tensors ($m^2\ s^{-1}$). $\vec{\nabla} q$ is the concentration gradient and $\vec{\nabla} \cdot$ denotes the 2D divergence operator. From left to right, the terms of Eq. (2) represent the rate of change in concentration/isotope ratio, Fickian diffusion, gravitational fractionation, thermal fractionation, dispersive mixing and advection. Since Eq. (2) is only valid for the binary diffusion of a trace gas into a major gas, ratios of any two isotopes of masses x and y are obtained by separately simulating the ~~diffusion~~ transport of each isotope into the major gas $^{28}N_2$ and using the relationship

$$q_{x/y} = \frac{q_{x/28}}{q_{y/28}} \tag{3}$$

to calculate the isotope ratios of interest (Severinghaus et al., 2010).

Isotope ratios are assumed to be constant at the surface (Dirichlet boundary) and reconstructions of atmospheric CO_2 and CH_4 concentrations over the last 200 years are used to force runs of these anthropogenic tracers (see Supplementary Information (SI)). The model time step is 3.5 days; smaller time steps make the model impractical to run due to computational costs. The bottom boundary is implemented by allowing only the advective flux to leave the domain (Neumann boundary). Diffusion and dispersive mixing cease below the COD. A periodic boundary condition is used in the horizontal direction. The horizontal extent of the model is varied between sites with differing snow accumulation rates to maintain a constant ratio of annual layer thickness to the model's spatial extent, which affects barometric pumping velocity. Firn density (Fig. ~~4a~~3a) is prescribed from a fit to the measured density profile at each site. Following Severinghaus et al. (2010) and Kawamura et al. (2013), empirical relationships are used to derive open and closed porosities from the density profile (Fig. ~~4b~~3b). The pressure-corrected open porosity $\tilde{s}$ is assumed to be time independent.

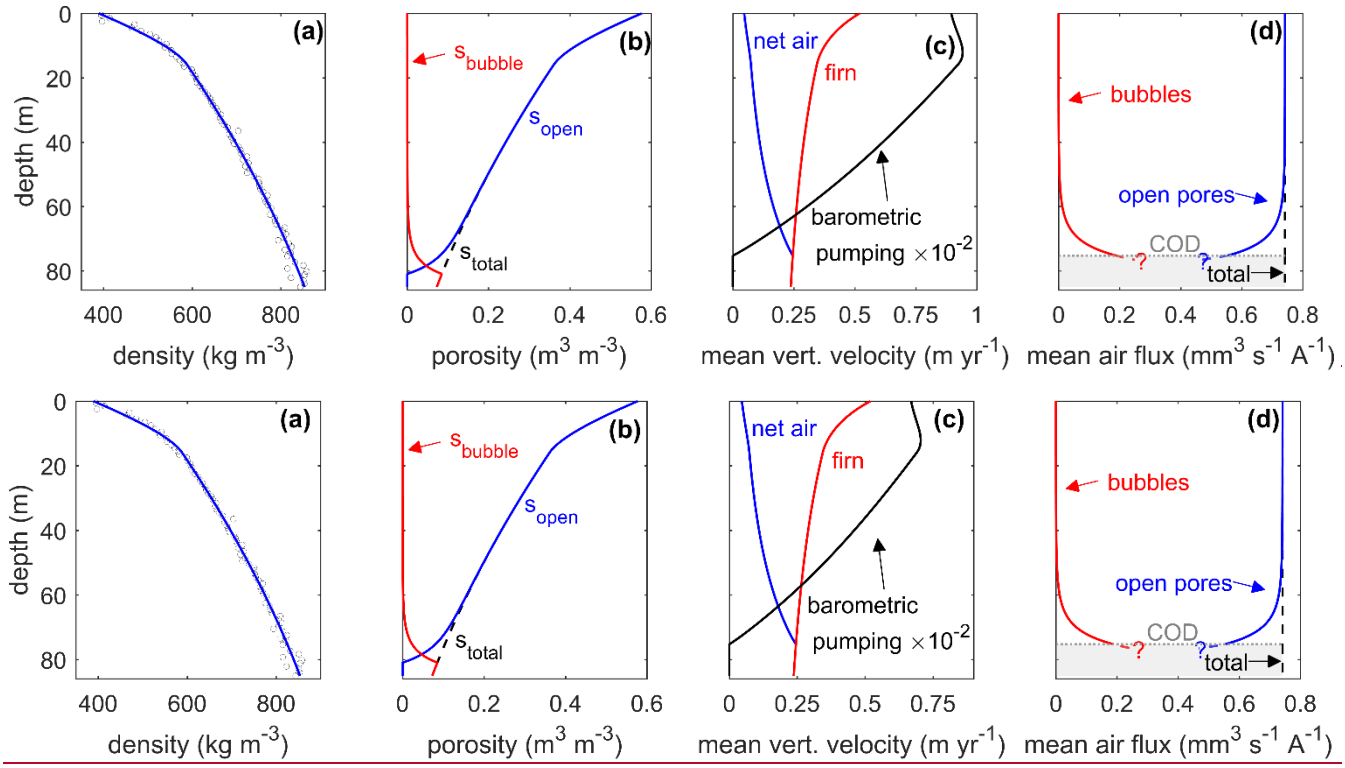

Figure 34. Firn conditions and modelled velocities profiles at WAIS Divide. (a) Density fit to observed data (data from Battle et al., 2011)~~,~~ (b) open, bubble (i.e., closed) and total porosity~~,~~ (c) horizontally averaged barometric pumping ~~strength~~ velocity (i.e., time-mean horizontal average of $|\vec{u}_b|$, black), and horizontally averaged net air velocity($\vec{w}_{firn} + \vec{u}_r$, blue) and firn velocity ($\vec{w}_{firn}$, red)~~, and~~; (d) mean air flux in open pores (blue) and bubbles (red).

2.2 Advection velocity and barometric pumping

The 2D velocity field $\vec{u}$ is a result of a combination of (i) air migration with the firn ($\vec{w}_{firn}$), (ii) return flow of air $\vec{u}_r$ ~~from~~ the firn to the atmosphere due to the gradual compression of pores ($\vec{u}_r$), and (iii) airflow resulting from barometric pumping $\vec{u}_b$ (Figs. ~~4c~~ 3c & ~~5~~4). Details on the~~ir~~ derivation of these velocities are provided in the SI. In short, $\vec{w}_{firn}$ ~~is the vertical advection of snow and air in the firn column and~~ is constrained by assuming a time-constant snow and ice mass flux at all depths. ~~The return flow~~ $\vec{u}_r$ is calculated based on the effective export flux of air in open and closed pores at the close-off depth (COD), imposing a constant mean vertical air flux throughout the firn column (Fig. ~~4d~~3d) (Rommelaere et al., 1997; Severinghaus and Battle, 2006). ~~Finally, the barometric pumping flow~~ $\vec{u}_b$ is the airflow needed to re-establish hydrostatic balance in the firn in response to any surface pressure anomaly. Surface pressure variability is represented by (pseudo-) red noise, mimicking observed pressure variability at both sites. The near-coast location Law Dome is more strongly affected by storm activity than WAIS Divide with pressure variability ~11.2 hPa day^{-1} compared to ~7 hP day^{-1} at WAIS Divide. $\vec{u}_r$ and $\vec{u}_b$ follow Darcy's law of flow through porous media (Darcy, 1856):

$$\vec{u} = -\frac{\kappa}{\tilde{s}\,\mu}\nabla P, \tag{4}$$

with ∇P the pressure gradient, κ the permeability of firn, and μ the viscosity of air (Fig. ~~5~~4).

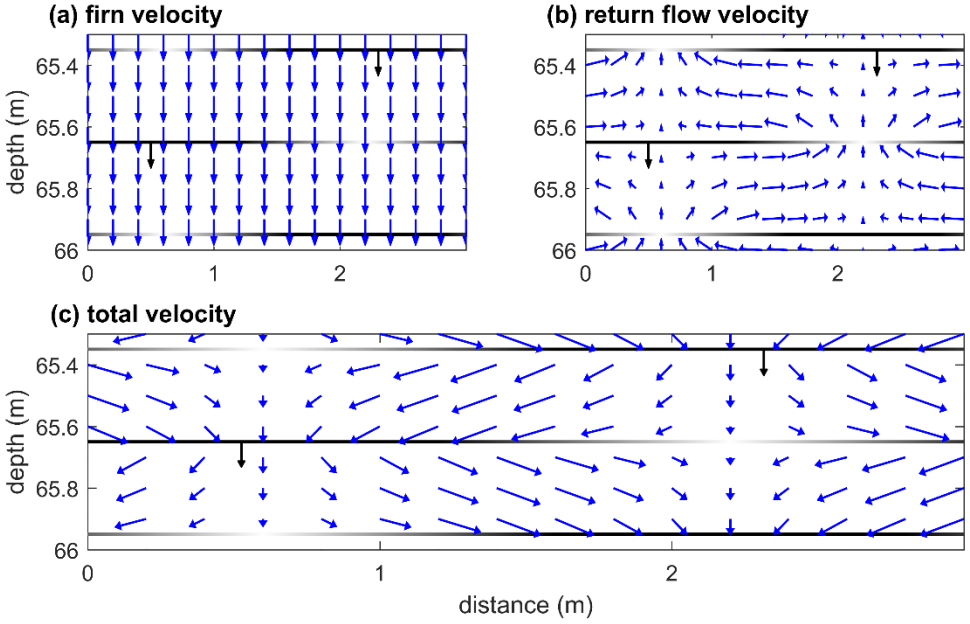

Figure ~~4~~5. The different components of the velocity field. ~~A linear combination of~~ (a) ~~the~~ firn velocity ~~and~~; (b) the velocity of air return flow to the atmosphere due to pore compression ~~yield~~; (c) ~~the~~ net firn air advection velocity ~~used in the model for a certain layer configuration~~(a linear combination of the fields in panels a ad b). Because of its alternating direction, barometric pumping yields no net flow but instantaneous flow field patterns look similar to panel (b). Black arrows indicate the ~~slow~~ downward advection of layers at the firn velocity.

2.3 Firn layering

Idealized firn layering is implemented by forcing the vertical velocity components u_r and u_b, as well as all vertical diffusive fluxes between the grid boxes on either side of a layer to be zero. Only the advection of air with the firn ($\vec{w}_{firn}$) remains active at~~for~~ these grid box boundaries. Layering limits vertical gas transport and yields almost exclusively horizontal transport between layers. ~~Here, we~~We ~~represent~~ assign layers ~~to have~~an infinitesimal thickness~~,~~ because of the computationally limited spatial resolution of the model. Layers are repeatedly introduced at a specific depth and migrate down with the velocity of the firn. The vertical distance between layers is set to correspond to the snow accumulation of one year and the horizontal extent of layers increases linearly with depth until they cover the entire domain at the close-off depth (COD). The mean layer opening size is held proportional to the annual layer thickness ~~at all sites~~ to make the vertical advection velocities independent of the arbitrary horizontal extent of the model. To obtain more realistic flow fields, the permeability of layers ~~tapers off at~~increases gradually towards both ends of a layer.

2.4 Dispersive mixing

The dispersion tensor $\boldsymbol{D}_d$ is made up of two components, (i) ~~convective~~ non-fractionating mixing of air in ~~a shallow region near the surface~~the SMZ and (ii) dispersive mixing caused by barometric pumping in the tortuous firn medium ~~in the more tortuous, deep firn~~. First, the ~~well-mixed convective zone~~SMZ is commonly represented by mass-independent ("eddy") diffusion acting in the vertical and horizontal directions. The corresponding diffusivity profile ~~of convective mixing $D_e = D_{eSMZ}(z)$~~ is pre~~de~~scribed as an exponential decay away from the snow-atmosphere interface (Kawamura et al., 2013). Its maximum surface value and the decay constant are chosen to match observed $\delta^{15}N$ values in the deep firn. After reaching a specified maximum depth of 8 m ~~or 14 m~~ at WAIS Divide and 14 m at Law Dome DSSW20K, D_{SMZ} ~~respectively, the diffusivity~~ tapers linearly to zero over 2 m.

Second, airflow through any dispersive medium leads to mixing in the directions longitudinal and transverse to the flow~~longitudinal-to-flow (i.e., along the flowline) and transverse-to-flow (i.e., across the flowline) mixing~~. Because barometric pumping velocities are orders of magnitude faster than the return flow, dispersive mixing is dominated by barometric pumping. ~~The 2D dispersion tensor becomes:~~

~~$$\boldsymbol{D}_d = \begin{bmatrix} D_L \frac{u_n^2}{v^2} + D_T \frac{w_n^2}{v^2} + D_e & \frac{u_n w_n}{v^2}(D_L - D_T) \\ \frac{u_n w_n}{v^2}(D_L - D_T) & D_T \frac{u_n^2}{v^2} + D_L \frac{w_n^2}{v^2} + D_e \end{bmatrix}, \quad (5)$$~~

~~where $u_n \equiv u_r + u_b$ and $w_n \equiv w_r + w_b$ are the sum of the return and barometric pumping velocity components in the x- and the y-directions with $v \equiv (u_n^2 + w_n^2)^{0.5}$. D_L and D_T are the longitudinal- and transverse-dispersion coefficient ($m^2\ s^{-1}$), respectively. D_L and D_T are commonly approximated as linear functions of velocity (Freeze and Cherry, 1979)~~

~~$$D_L = \alpha_L v \quad (6)$$~~

~~$$D_T = \alpha_T v \quad (7)$$~~

~~where the proportionality factors α_L and α_T are the longitudinal- and transverse-to-flow dispersivity (m).~~

The degree of dispersive mixing in firn presumably depends on the direction of flow and ~~probably also~~ differs between the longitudinal-to-flow and transverse-to-flow direction. However, the treatment of anisotropic media is complex and only one parametrization for vertical, longitudinal-to-flow dispersion in firn is currently available (Buizert and Severinghaus, 2016). Therefore, we assume that the dispersivity α of firn is isotropic ~~(i.e., $\alpha_L = \alpha_T \equiv \alpha$).~~and linearly dependent on the magnitude of the flow velocity vector ($v \equiv |\vec{u}_b + \vec{u}_r|$). ~~In this case, the 2D dispersion tensor becomes~~This simplifies ~~$\boldsymbol{D}_d$~~ to

$$\boldsymbol{D}_d = (\alpha\, v + D_{eSMZ})\, \boldsymbol{I}, \quad (8)(5)$$

with $\boldsymbol{I}$ the second order identity matrix (Freeze and Cherry, 1979; Buizert and Severinghaus, 2016). The dispersion flux term in Eq. (2) ~~becomes~~simplifies to

$$\tilde{s}\boldsymbol{D}_d\vec{\nabla}q = \tilde{s}\,[\alpha\, v + D_{eSMZ}]\,\vec{\nabla}q. \qquad (9)(6)$$

The dispersivity parametrization of Buizert and Severinghaus (2016) is based on direct measurements of cylindrical firn samples from Siple Station, Antarctica, performed by Schwander et al. (1988). The parameterization relates dispersivity to open porosity s_{op} as

$$\alpha(s_{op}) = \tilde{s}\,[1.26 \cdot \exp(-25.7\, s_{op})]. \qquad (10)(7)$$

~~Here, the~~A factor of $\tilde{s}$ was added to the original parameterization by Buizert and Severinghaus (2016) because α relates dispersive mixing to the velocity components u_n and w_n, that denote flow velocities per unit pore cross-section (w_{pores}). Schwander et al. (1988), however, originally measured the considerably slower bulk airflow per unit firn cross-section (i.e., $w_{bulk} = \frac{w_{pores}}{\tilde{s}}$). Since dispersivity is a scale dependent property, it is important to use parametrizations that are compatible with the resolution of the numerical model. The sample size of Schwander et al. (1988) (i.e., 30 mm diameter & 50 mm length) approximately matches the resolution of our numerical model (i.e., 30 x 40 mm) and thus should adequately approximate subgrid-scale (i.e., pore-scale) mixing processes that currently cannot be resolved. Spatial inhomogeneity of subgrid-scale firn dispersivity that was not captured by the sampling of Schwander et al. (1988) cannot be accounted for in the model. Dispersion on larger scales such as the interaction of flow and layers is explicitly represented in the model by the interplay of advection and diffusion. Thus, dispersive mixing is ~~completely~~ fully constrained in the model and based on empirical parameterizations that are not subject to ~~any~~ tuning.

2.5 Molecular diffusion

The (effective) molecular diffusivity profile is established by simultaneously fitting the simulated CO_2 and CH_4 profile to real firn measurements at both sites. Effective vertical diffusivity decreases with depth to represent the subgrid-scale effect of decreasing pore connectivity and increasing firn tortuosity, which is not fully represented by the explicit macroscopic layers in our model. A spline function ~~defines~~ is used to obtain the effective vertical diffusivity profile, which decreases monotonically from the surface to zero at the COD (Fig. ~~6~~5). Diffusivities for other trace gases are calculated by scaling the tuned CO_2 diffusivity by the free air diffusivity of each gas relative to CO_2 (Trudinger et al., 1997). The diffusivity tuning presents an underconstrained problem because horizontal and vertical molecular diffusivities are essentially free parameters. It is qualitatively evident from firn air sampling that horizontal connectivity/diffusivity is much higher than vertical diffusivity in ~~the~~ deep firn, but ~~this observation is incompletely quantified~~no satisfactory quantification of this anisotropy is available. As a best guess estimate, we set ~~Here,~~ horizontal molecular diffusivities ~~are fixed to 10x~~equal to 10x the vertical diffusivity at the

same depth. ~~and annual layers represented some fraction of the total tortuosity explicitly in the model.~~ There are many degrees of freedom in tuning molecular diffusivities and ~~the~~ our diffusivity parameterization is therefore not unique~~.~~ However, sensitivity tests with equal horizontal and vertical diffusivity in the model (compensated by shorter horizontal layers) yield comparable results.

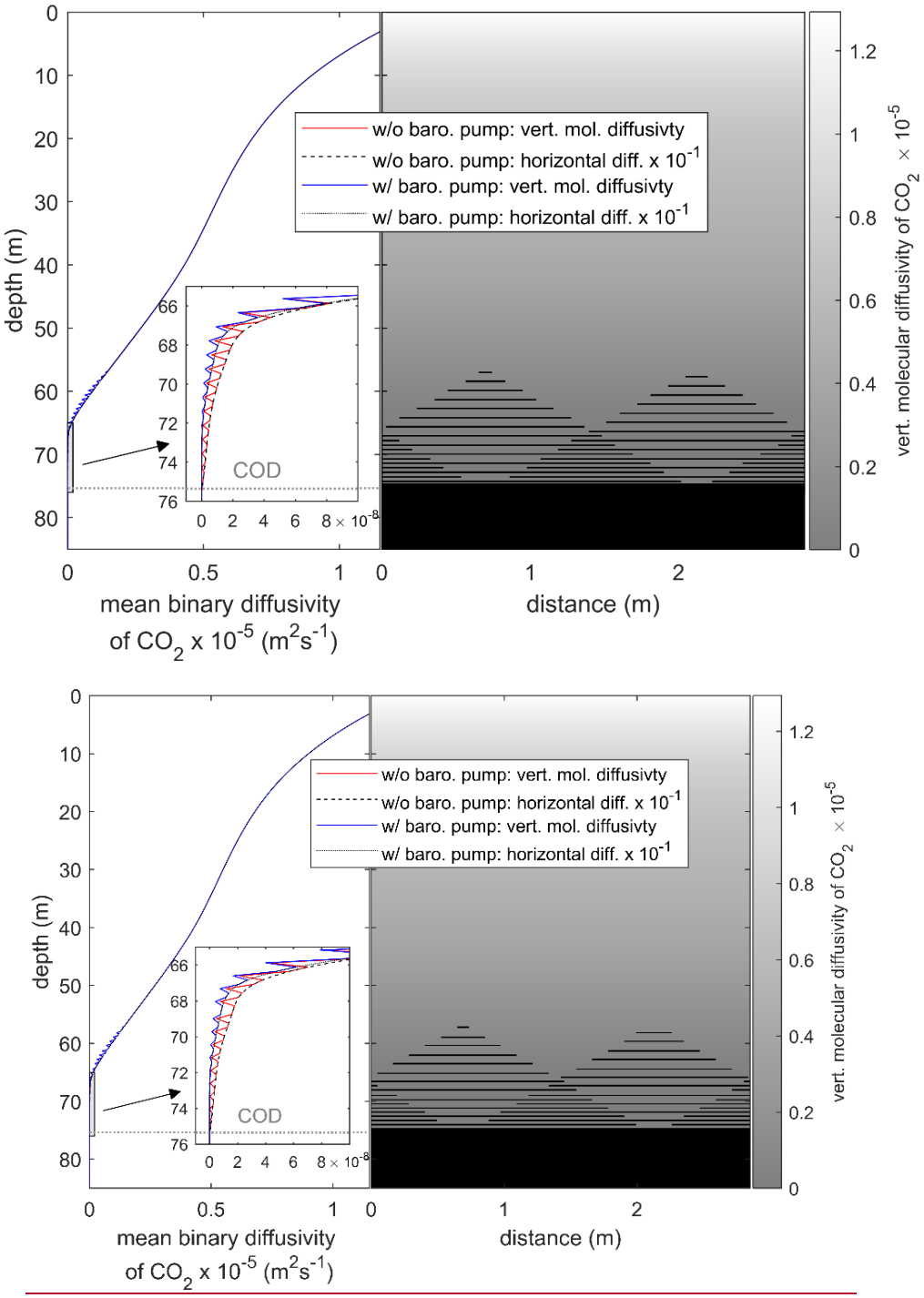

Figure 5~~6~~. The CO_2 diffusivity profile at WAIS Divide. Left panel: Horizontally averaged, vertical and horizontal diffusivity in the model with and without barometric pumping. Right panel: map of diffusivity in the 2D model without barometric pumping. Only every third layer present in the model is shown here for clarity.

2.6 Thermal fractionation and ~~the~~ temperature model

Finally, a 1D vertical thermal model by Alley and Koci (1990) is run separately to simulate the temperature evolution of the firn. The model is forced by a long-term surface temperature trend based on published records by Van Ommen et al. (1999), Dahl-Jensen et al. (1999) and Orsi et al. (2012). A ~~generic~~ mean Antarctic seasonal cycle derived from a ~8-10-year climatology of automatic weather station observations at WAIS Divide and Law Dome (Lazzara et al., 2012) is superimposed on this trend. Alley and Koci's temperature model is based on the heat transport equation for firn (Johnsen, 1977) with parametrizations for firn thermal properties from Weller and Schwerdtfeger (1977). Horizontal temperature gradients in firn are small at both sites and neglected in this study.

Considerable temperature gradients can exist in present-day firn because of recent global atmospheric warming and these gradients can lead to increased isotope thermal fractionation, in particular of $\delta^{15}N$. The sensitivity of isotopes to diffuse in response to temperature gradients is captured by the thermal diffusion sensitivity Ω. ~~Values of~~The temperature dependence of Ω ~~are~~ is approximated as a function of the effective average temperature T in Kelvin:

$$\Omega = \frac{a}{T} - \frac{b}{T^2} \qquad \text{~~11)~~(8)}$$

or Ω is assumed to be temperature independent if the ~~temperature sensitivity is~~coefficients a and b are unknown for a specific isotope ratio (Severinghaus et al., 2001). Coefficients a and b were determined experimentally for different isotope ratios by Grachev and Severinghaus (2003a, 2003b) and~~,~~ Kawamura et al. (2013) ~~and Kawamura (unpublished)~~.

A ~~detailed overview of further~~table of all model parameters and further details of the numerical realization of 2D gas transport ~~may be found~~is provided in the SI ~~(SI Sect. 1-4)~~.

3 Results

3.1 WAIS Divide

3.1.1 CO_2 and CH_4

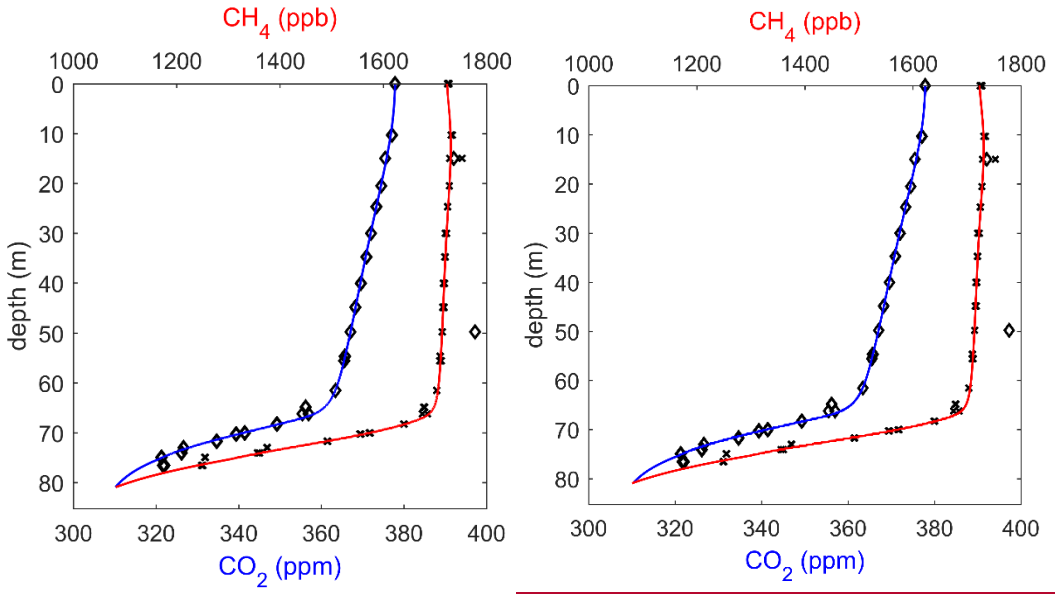

Figure 6~~7~~. Simulated and observed CO_2 and CH_4 concentrations in the firn at WAIS Divide. The model is initialized with the recorded atmospheric trace gas concentrations in 1800 CE at all depths and is forced at the surface with histories of atmospheric CO_2 and CH_4 concentrations (Etheridge et al., 1996, 1998; Keeling et al., 2001; Buizert et al., 2012; Dlugokencky et al., 2016a, 2016b). Markers indicate observed CO_2 (diamonds) and CH_4 (crosses) concentrations (Battle et al., 2011). Based on high CO_2 and CH_4, two samples at ~15 m and ~50 m depth were likely compromised by modern air during analysis and are thus ignored in the curve fit. Differences in the CO_2 and CH_4 profiles between the 1D model and the 2D model with or without barometric pumping are not visible at the resolution of this figure but are illustrated in the SI (Fig. S12~~9~~).

A comparison of simulated and observed CO_2 and CH_4 profiles shows good agreement at WAIS Divide, supporting the plausibility of our layered diffusivity parameterization (Fig. ~~7~~6). In line with observations, both CO_2 and CH_4 concentrations decrease slowly with depth until ~68 m below the surface due to the gradually increasing gas age and the anthropogenic rise in atmospheric CO_2 and CH_4 concentrations. ~~where they begin to~~The more rapid decrease ~~more rapidly~~of CO_2 and CH_4 below ~68 m is explained by a much slower vertical penetration of air and a faster increase of the gas age with depth in the LIZ.

In the following discussion we will examine and compare results from four different ~~permutations~~ versions of the 2D model: with or without impermeable layers and with activated or deactivated barometric pumping. In versions without layering, our 2D model loses all horizontal heterogeneity and will thus be referred to as a ~~'~~"1D ~~model'~~ model" in what follows~~throughout the text~~. Since the explicitly implemented tortuosity from layering in the 2D model affects molecular diffusion and dispersion equally it is represented by ~~equally~~ lowering the effective molecular diffusivity and dispersivity equally in the layered region of the 1D version instead. Diffusivities are tuned such that the CO_2 profiles are (nearly) identical. The small remaining

deviations in CO_2 and CH_4 concentrations between model ~~permutations~~ versions (< ±0.~~5~~ 8 ppm and < ±~~5~~ 9 ppb, respectively) are illustrated in ~~the SI (~~Fig. S~~9~~12~~)~~.

3.1.2 $\delta^{15}N$ and thermal fractionation

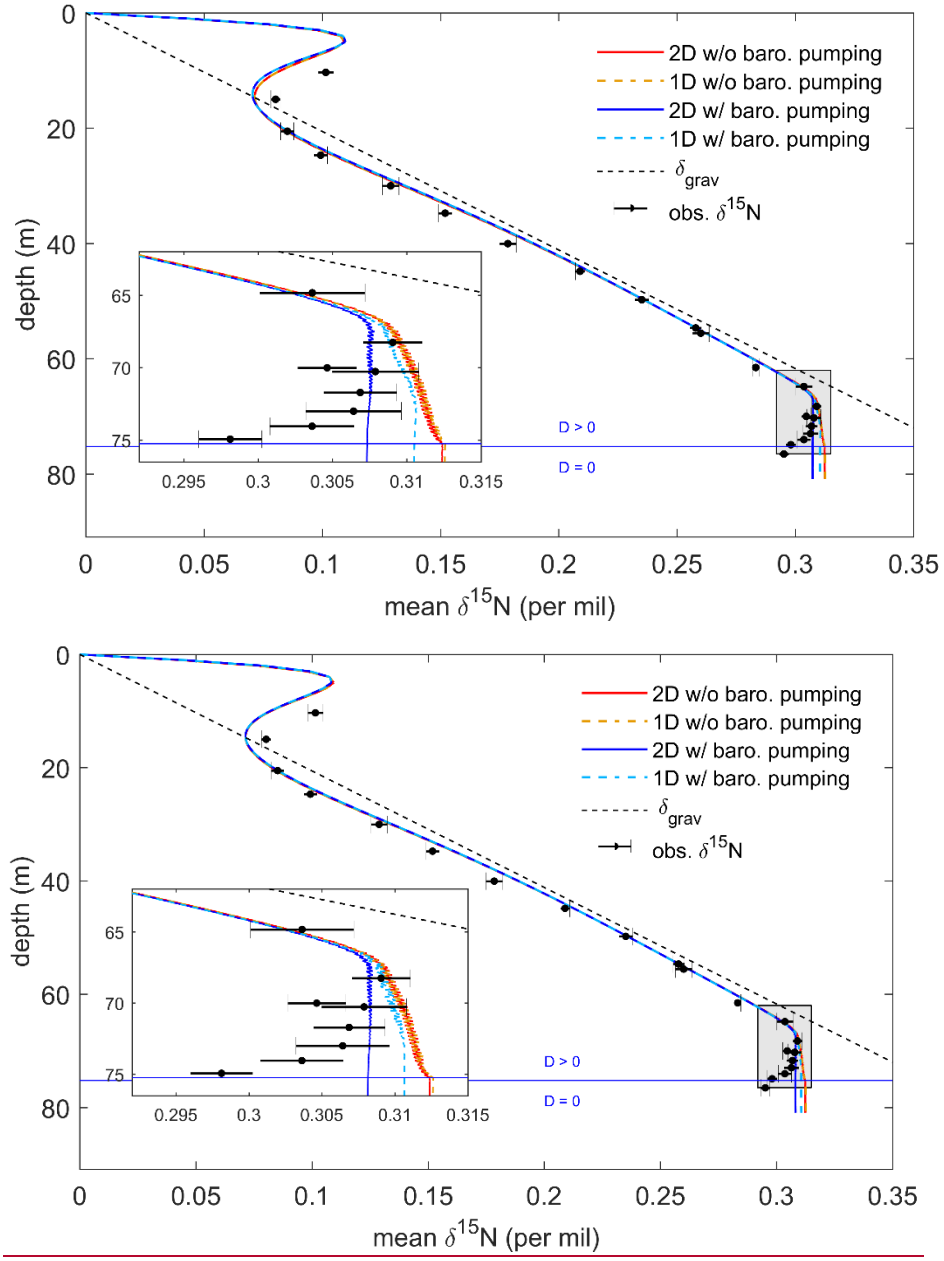

Figure ~~7~~8. Horizontally averaged $\delta^{15}N$ at WAIS Divide. Model output is shown from four different versions of the 2D model (see text). Black circles with error bars indicate the observed firn $\delta^{15}N$ (Battle et al., 2011). The dashed black line represents the equilibrium solution

for pure gravitational settling (δ_{grav}). The horizontal blue line marks the depth where vertical diffusivity reaches zero. The ~~inlay~~ inset shows a magnification of the lock-in zone.

In all four model setups, the seasonal cycle of temperature dominates the shape of the $\delta^{15}N$ profiles in the top ~30 m (Fig. ~~8~~7). Warm summer temperatures drive the migration of heavy isotopes into the colder firn below and produce a $\delta^{15}N$ summer peak just below the surface (Severinghaus et al., 2001). In contrast, a minimum of $\delta^{15}N$ occurred in this region during the previous winter season when the thermal gradients were reversed. The remnants of this winter minimum are still visible in the gas record as anomalously low $\delta^{15}N$ values below the summer peak. The differences between observations and simulated $\delta^{15}N$ values in the top of the firn column are likely caused by ~~the~~ our idealized representation of the seasonal cycle in the model. ~~Anomalous temperature gradients associated with extraordinary weather events just before firn air sampling will modify the observed $\delta^{15}N$ at the site but are unaccounted for in the model.~~

3.1.3 Impact of ~~(near-) impermeable~~reduced-permeability layers

In the layered 2D model without barometric pumping, the simulated $\delta^{15}N$ values are close to observations at the top of the LIZ but continue to increase with depth (Fig. ~~8~~7). This is contradicted by observational data even when the unusually low $\delta^{15}N$ values ~~right on~~at the COD and below are not taken into consideration (near the COD, firn air ~~pumping~~ sampling becomes more difficult in the field and the potential for fractionation during sampling is increased). A closer inspection of the lock-in zone in Figs. ~~8~~ 7 and ~~9~~ 8 reveals a zigzag pattern in the $\delta^{15}N$ profile where impermeable layers are present. Simulated ~~I~~isotope ratios are higher just above horizontal layers, where heavy isotopes can accumulate, and are anomalously low below layers where ~~they~~ heavy isotopes are more readily removed than supplied by gravitational settling. Gravitational settling through gaps in the layers sets up small horizontal concentration gradients that drive horizontal Fickian diffusion. Layering increases the effective travel path length for molecules and reduces the effective vertical diffusivity by increasing the tortuosity. However, layering alone appears to be insufficient to prevent gravitational settling completely, ~~because~~ with continued gravitational enrichment beingis observed in the LIZ in this model version.

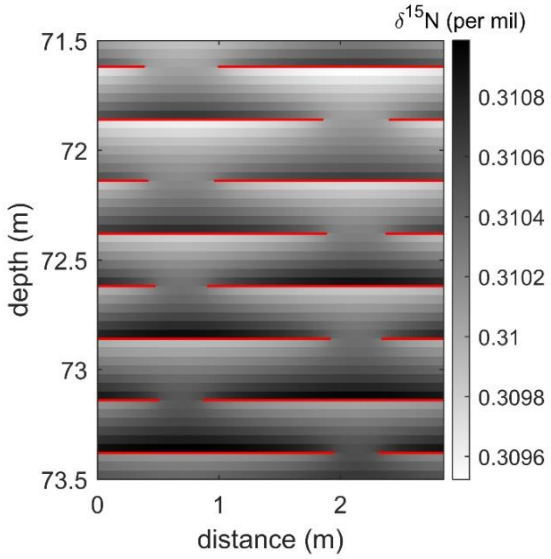

Figure ~~8~~9. Simulated $\delta^{15}N$ in a part of the lock-in zone at WAIS Divide from the 2D model not including barometric pumping. Impermeable horizontal layers are shown in red. The ~~openings sizes~~size of the openings in the layers shrink with increasing depth.

Is the impact of layers on the firn trace gas profile larger for isotopes such as $\delta^{15}N$ than for anthropogenic tracers such as CO_2, CFCs, or CH_4? All three gases have experienced large atmospheric variability in the industrial era. Therefore, the migration of these gases into the firn is dominated by vertical and horizontal Fickian diffusion~~. in contrast to~~ For $\delta^{15}N$, on the other hand, ~~where~~ the effect of gravity is critical for transport. To answer the above question, we compare output from the layered 2D model to the 1D model without layers. We find that $\delta^{15}N$ values in the 1D and 2D model without barometric pumping are almost identical (Fig. ~~8~~7). Layering in the 2D model increases the effective transport distance ~~of~~ for CO_2 just as much as for $\delta^{15}N$ and there is no disproportional impact of layering on gravitationally fractionated isotope ratios. Differences in explicitly represented tortuosity are automatically compensated in the 1D model during tuning to the same CO_2 profile by reducing molecular diffusivities. Therefore, we conclude that layering alone cannot simultaneously explain the observed CO_2 and $\delta^{15}N$ patterns.

3.1.4 Barometric pumping and the emergence of the LIZ

$\delta^{15}N$ values simulated by the 1D and 2D model with barometric pumping are lower in the LIZ than in both model versions without barometric pumping (Fig. ~~8~~7). Accounting for barometric pumping improves the agreement with observations throughout the lock-in zone. However, the reduction of gravitational fractionation is substantially stronger when layers are present. Only when both layering and barometric pumping are accounted for in the model simultaneously, does the $\delta^{15}N$ profile correctly indicate no further gravitational enrichment in the LIZ and ~~closely~~ match~~es~~ observations more closely. Dispersive mixing is nearly independent of molecular mass and does not lead to gravitational fractionation, but rather acts to eliminate the concentration gradients associated with gravitational settling. Although barometric pumping velocities are largest near the

surface (Fig. ~~4c~~3c), significant dispersive mixing is generally limited to the LIZ because ~~the~~ dispersivity of firn is inversely related to the open porosity in the parameterization of Buizert and Severinghaus (2016) and dispersion is overwhelmed by molecular diffusion in the DZ. Furthermore, molecular diffusivities drop rapidly in the LIZ ~~when barometric pumping is active~~ in the model (Fig. ~~6~~5). Because dispersion provides an additional transport mechanism for trace species, even less molecular diffusion is needed to match observed CO_2 and CH_4 concentrations in the LIZ when barometric pumping is active. Layering amplifies the importance of barometric pumping because gravitational fractionation between annual layers is restricted into the small gaps in the LIZ (Fig. ~~9~~8). Narrow pathways~~A lack of alternative pathways~~ ~~amplifies~~ amplify barometric pumping flow~~s~~ velocities and thus dispersive mixing in these regions (Fig. ~~5~~4), thus overwhelming the influence of gravitational fractionation more readily than in the 1D model. This effect is responsible for the larger differences between the $\delta^{15}N$ profiles obtained from the two model~~s~~ versions with barometric pumping in Fig. ~~8~~7. The strength of dispersive mixing in our layered 2D model is physically motivated; thus, barometric pumping and layering together lead to a more natural emergence of the $\delta^{15}N$-defined lock-in zone in the 2D model.

3.1.5 The ~~convective~~ surface mixed zone ~~height~~depth

We estimate the depth of the ~~convective~~ SMZ~~zone~~ at WAIS Divide to be ~2.8 m. Multiple different procedures have been used to estimate ~~convective zone~~SMZ ~~heights~~ thickness in the past, many of which rely on $\delta^{15}N$ data in the deep firn near the LIZ (Battle et al., 2011). However, if the deep firn is affected by dispersive mixing due to barometric pumping, these estimates may be falsely attributing some fraction of the dispersive mixing in the deep firn to the SMZ~~convective zone~~. To address this problem, we follow the method of Severinghaus et al. (2010) in calculating SMZ~~convective zone~~ thickness. This approach compares the depth where $\delta^{15}N$ reaches a certain value in two different model configurations with ~~and without convection~~zero and non-zero values of D_{SMZ}. Thermal effects are neglected. The first setup is the 2D model with barometric pumping as presented above but the dispersivity is set to zero everywhere without retuning the model. The ~~convective zone~~SMZ ~~height~~ thickness is calculated from the depth difference between this model run and a second model run where barometric pumping is deactivated, $D_{SMZ} = 0$~~and the convective zone are deactivated~~, and thus only advection and gravitational fractionation shape the profile of $\delta^{15}N$. Our ~~height~~ depth estimate of 2.8 m is within the range of values from 1.4 to 5.2 m published previously (Battle et al., 2011).

3.2 Law Dome DSSW20K

At Law Dome DSSW20K, the firn thickness is ~20 m less than at WAIS Divide. Accumulation rates are comparable, but annual-mean temperatures are ~10 K warmer. The ~~convective zone~~SMZ is slightly deeper and barometric pumping is stronger at Law Dome, yielding more ~~convective~~near-surface and dispersive mixing. Constraining the ~~convective zone height~~ SMZ depth at DSSW20K is ~~complicated~~ more difficult because ~~less~~ fewer $\delta^{15}N$ measurements are available for this site, and their associated uncertainty is, at $\pm$15 per meg, much larger than at the more recently sampled WAIS Divide site (Trudinger et al., 2002). Molecular diffusion generally takes a less important role at DSSW20K and molecular diffusivities obtained by tuning

are about half or less than those at WAIS Divide for most of the firn column. Thermal fractionation has a weaker impact on the isotope record near the surface at Law Dome due to the smaller amplitude of the seasonal cycle and stronger ~~convective~~ near-surface mixing compared to WAIS Divide. Figures of molecular diffusivity, advection velocities and other firn properties at site DSSW20K are ~~available~~ provided in the SI ~~Sect. 5~~.

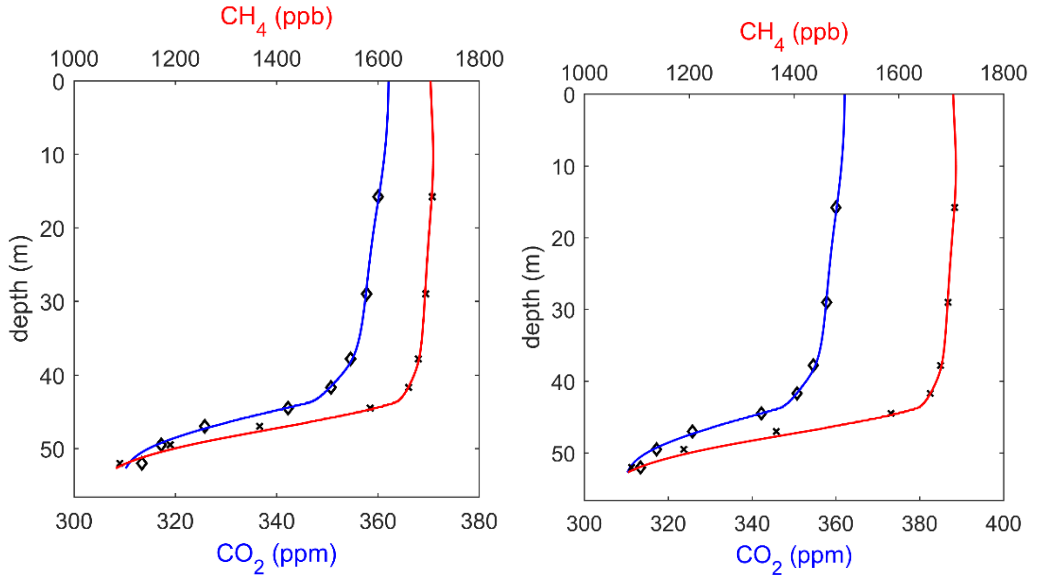

Figure ~~9~~10. Simulated CO2 and CH4 concentrations in the firn at Law Dome DSSW20K. The model is forced with histories of atmospheric CO_2 and CH_4 concentrations from 1800 to 1998 CE (the date of sampling). Markers indicate observed CO_2 (diamonds) and CH_4 (crosses) concentrations (Trudinger et al., 2002).

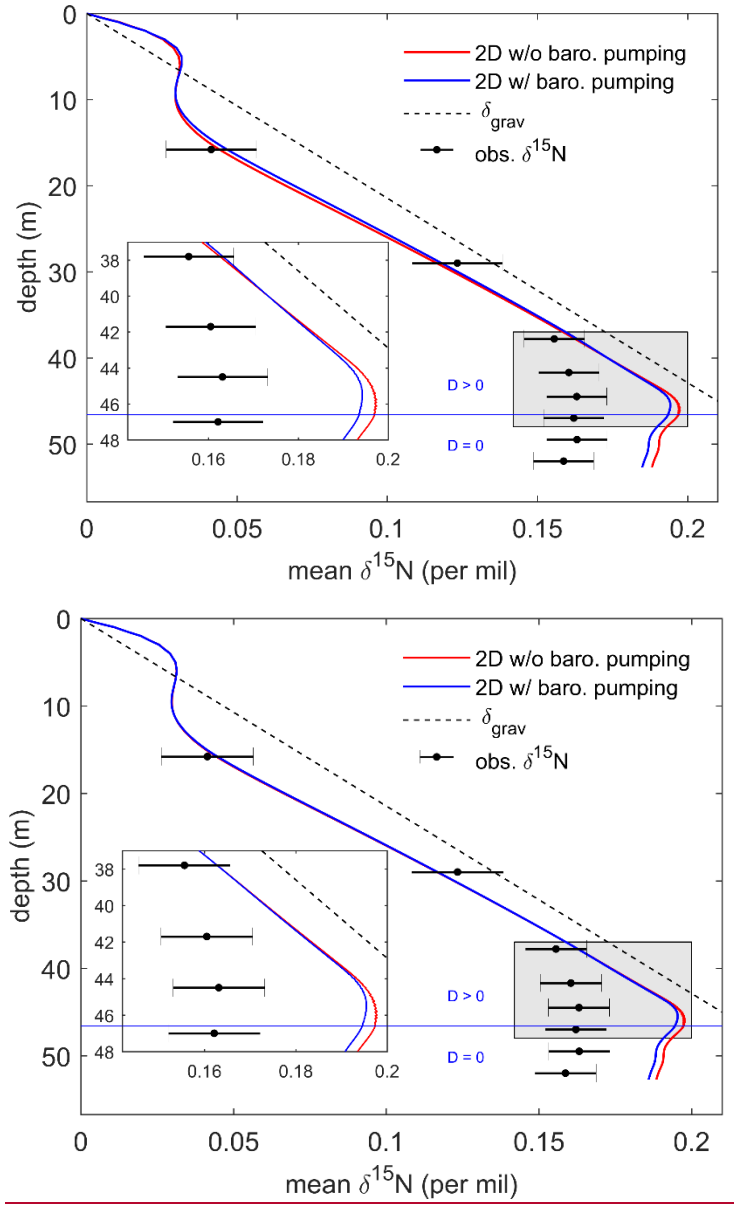

Figure 10~~11~~. Horizontally averaged δ^{15}N at Law Dome DSSW20K. The solid ~~blue and red~~ lines show the results of the 2D model (with layers), for the cases with (blue) and without (red) ~~including and excluding~~ barometric pumping~~, respectively~~. Black circles with error bars indicate the observed firn δ^{15}N (Trudinger et al., 2002, 2013). The dashed black line represents the equilibrium solution for pure gravitational settling (δ_{grav}). The horizontal blue line marks the depth where vertical diffusivity reaches zero. The ~~inlay~~ inset shows a magnification of the lock-in zone.

Simultaneously matching the δ^{15}N, CO_2 and CH_4 profile at Law Dome DSSW20K has proven difficult in the past (Trudinger et al., 2002; Buizert and Severinghaus, 2016). Simulated δ^{15}N in the LIZ is typically ~~significantly~~ substantially higher than in observations. Buizert and Severinghaus (2016) suggested that barometric pumping in the deep firn may be able to reconcile this contradiction. However, the mixing obtained from theoretical predictions was insufficient to ~~obtain the~~

~~anticipated results~~achieve a satisfactory fit. Buizert and Severinghaus (2016) hypothesized that firn layering may play a critical role in amplifying the impact of barometric pumping. ~~They~~ The authors used an idealized eddy and molecular diffusivity profile in the deep firn to simulate the effect of layers on firn air transport. Using these diffusivity profiles, they were able to obtain good agreement with observed $\delta^{15}N$, CH_4 and $^{14}CO_2$. Our 2D model includes an explicit representation of layering and places similar physical constraints on barometric pumping as the 1D model of Buizert and Severinghaus (2016). The model is tuned to optimize agreement with CO_2 and CH_4 and the patterns of both profiles are reproduced correctly (Fig. ~~10~~9). But the disagreement between modelled and observed $\delta^{15}N$ in the deep firn remains despite barometric pumping producing ~~significant~~ substantial non-fractionating dispersive mixing in the region (Fig. ~~11~~10). Simulated $\delta^{15}N$ values diverge from observations at ~38 m, where gravitational enrichment seems to stop in observations but continues in the model. ~~The~~ In contrast, the LIZ, as ~~indicated~~ defined by CO_2 and CH_4, ~~in contrast~~ only starts at roughly 43 m depth. Such an early onset of dispersive mixing is not supported by the dispersivity parameterization. However, only the longitudinal-to-flow mixing in the vertical direction at Siple Station was used to develop the firn dispersivity parameterization, and the use of this parameterization may be inappropriate at Law Dome DSSW20K (Buizert and Severinghaus, 2016). Moreover, dispersivity typically differs in the horizontal and vertical as well as the longitudinal- and the traverse-to-flow directions, an effect that is not accounted for in this study because of a lack of observational evidence to constrain anisotropic dispersivity.

4 Discussion

4.1 Differential kinetic isotope fractionation

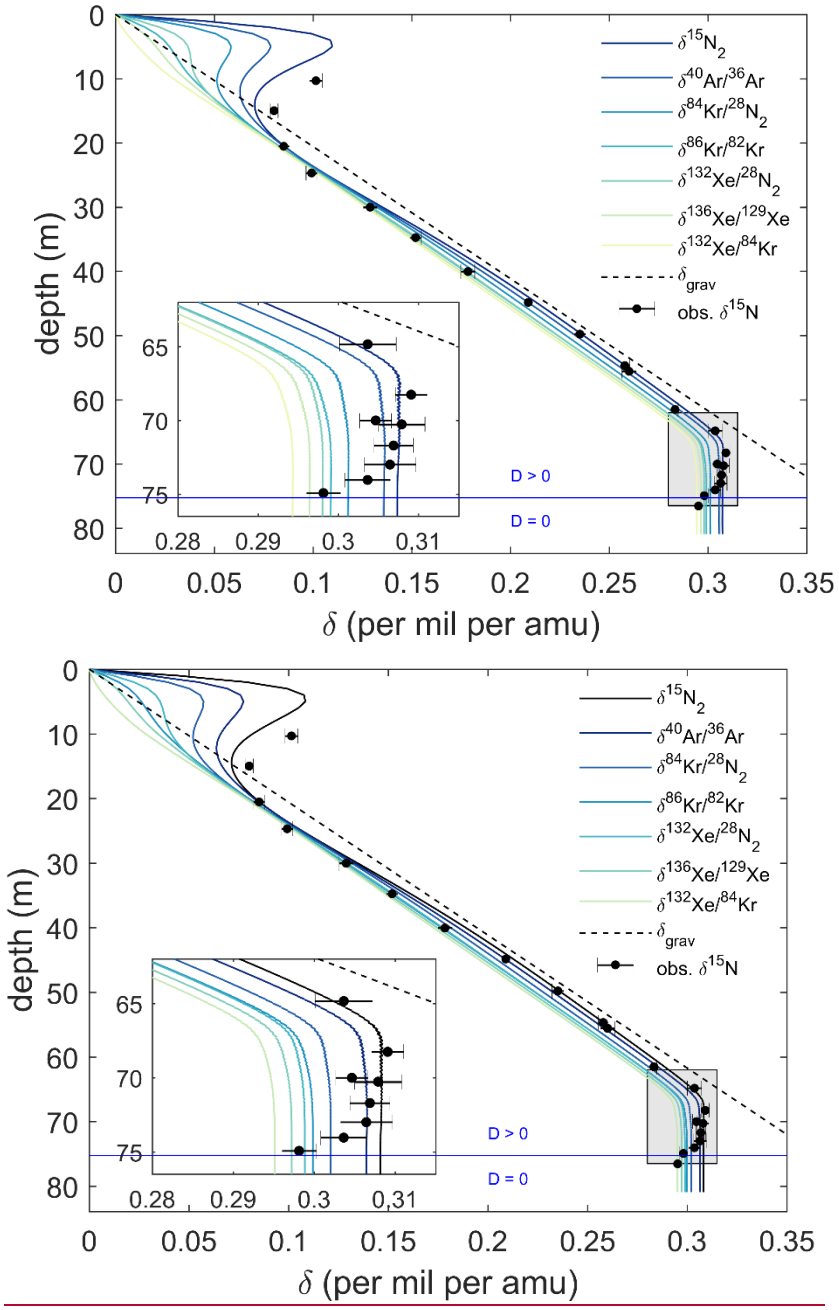

Figure 11~~12~~. Horizontally averaged isotope ratios at WAIS Divide in the 2D model including barometric pumping and horizontal layers. Isotope ratios are normalized to one atomic mass unit (amu~~, see SI~~) mass difference (SI ~~Sect. 6~~). The dashed black line represents the equilibrium solution for pure gravitational settling (δ_{grav}). The horizontal blue line marks the depth where vertical diffusivity reaches zero.

Observed $\delta^{15}N$ are shown as circles with horizontal error bars (Battle et al., 2011). The ~~inlay~~ inset shows a magnification of the lock-in zone (grey patch).

Isotope ratios in firn typically do not reach values as high as predicted from gravitational equilibrium due to the influence of advection and non-fractionating dispersive mixing (Trudinger et al., 1997; Kawamura et al., 2013; Buizert and Severinghaus, 2016). Advection and mass-independent mixing transport ~~less~~ less-fractionated air down in the firn column and act to counterbalance the enrichment of heavy isotopes by gravitational fractionation. As a result, ~~A~~all isotope ratios fall below the gravitational settling line δ_{grav} ~~in~~ (Fig. ~~12~~11) but ~~the magnitude of the deviation depends on the specific isotope pair. but the magnitude of the deviation depends on the specific isotope pair. This difference between the mass-normalized Kr and Ar isotope ratios has been termed ^{86}Kr excess (Buizert and Severinghaus, 2016). At the COD of WAIS Divide, simulated ^{86}Kr excess is ~5.6 per meg per amu in the 2D model with barometric pumping. This is significantly lower than the 7 – 22 per meg per amu values observed in the WAIS Divide ice core (Orsi A., personal communication).~~

The magnitude of disequilibrium of different isotope and elemental ratios is quantified ~~–~~here by defining the (mass-normalized) kinetic fractionation ϵ' relative to $\delta^{15}N$ ~~(ϵ')~~ (Kawamura et al., 2013) as

$$\epsilon'_{x/y} \equiv \frac{1}{1000 \times \Delta m_{x/y}} \ln\left(\frac{q_{x/28}}{q_{y/28}}\right) - \ln\left(q_{^{15}N}\right), \qquad \text{~~12~~(9)}$$

where $\Delta m_{x/y}$ is the mass difference of isotopes x and y. This definition is similar to the ^{86}Kr excess terminology introduced by Buizert and Severinghaus (2016) but ϵ' is given in the more precise $\ln(q)$-notation and uses $\delta^{15}N$ as ~~the~~ reference instead of $\delta^{40}Ar$/ $\delta^{36}Ar$. ~~Here,~~ To calculate $\epsilon'_{x/y}$, ~~i~~isotope ratios ~~are assumed to be~~must have been previously corrected for the influence of thermal fractionation either through combined Ar and N_2 measurements on firn air (Grachev and Severinghaus, 2003a, 2003b) or, as done here, by removing temperature effects with a suitable firn air transport model (Fig. ~~13~~12).

The degree of disequilibrium, represented by ϵ', ~~–~~ is caused by differential kinetic isotope fractionation. Heavy, slow-diffusing isotopes approach gravitational equilibrium more slowly than lighter, faster-diffusing isotopes. Therefore, slow-diffusing~~ratios of heavier~~ isotopes~~elements~~ ~~are more~~experience larger ~~susceptible to~~ kinetic ~~fractionatio~~fractionation (i.e., deviations from gravitational equilibrium) in regimes with non-zero advection or dispersion~~n~~. Consequently, ϵ' is more negative for heavier, slower diffusing isotopes. On its own, this ~~simple~~ rule of thumb cannot fully explain the pattern of ratios containing two different elements, such as $^{132}Xe/^{28}N_2$. The magnitude of disequilibrium in such mixed-element ratios is further discussed in Appendix B.

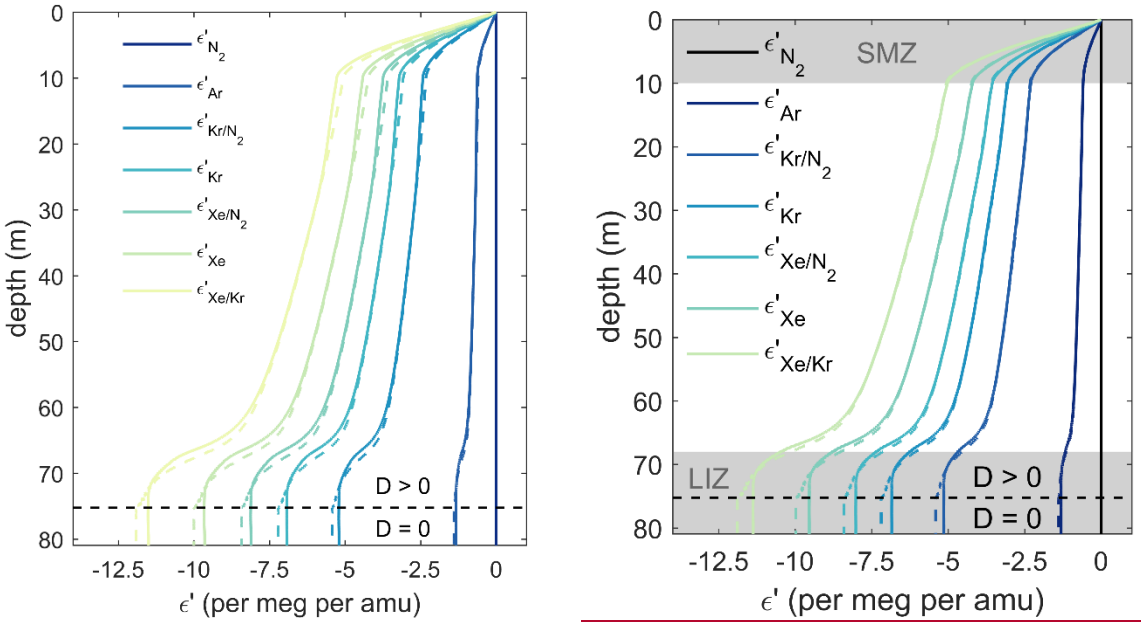

Figure 12~~13~~. Differential kinetic isotope fractionation (ϵ') profiles for different isotope pairs at WAIS Divide. Coloured solid and dashed lines show results from the 2D model with and without barometric pumping, respectively. $\epsilon'$is defined as the (typically negative) difference between any mass-normalized isotope ratio and $\delta^{15}N$ ~~as detailed in the~~(see text). Subscripts of one or two element names identify ratios as isotope or elemental ratios, respectively. The dashed black line highlights where molecular diffusivity in the model reaches zero.

In the DZ, ϵ' decreases almost linearly with depth, while within the ~~convective zone~~SMZ and ~~in the~~ LIZ ϵ' changes much more rapidly. Where molecular diffusivity is zero, ϵ' remains constant. This pattern is explained by the relative importance of advection and dispersive mixing compared to molecular diffusion in different regions of the firn column. The ~~vertical~~ Péclet number (Pe) traditionally quantifies the ratio of the advective to the diffusive transport and is here defined as the ratio of the diffusive to the advective time scale (τ_{D_m} and τ_{adv}). We~~Here we~~ add the time scale of dispersive mixing (τ_{D_e}) to the numerator because the effect of advection and dispersive mixing on the isotope profiles is very similar although the physics differ (Kawamura et al., 2013).

$$\mathrm{Pe} \equiv \frac{\tau_{adv} + \tau_{D_e}}{\tau_{D_m}} = \sim \frac{\frac{W}{L} + \frac{D_e}{L^2}}{\frac{\mathrm{D_m}}{L^2}} = \sim \frac{WL + D_e}{\mathrm{D_m}}, \qquad (10)$$

where $L = 1$ m is the characteristic length scale of firn air transport, and $\mathrm{D_m}$, W and D_e are characteristic values of the molecular diffusivity, the time mean vertical advection velocity, and the vertical dispersive or convective mixing at that depth, respectively.

This modifiede Péclet number ~~calculated in the model for the WAIS Divide~~ varies in the model by many orders of magnitude through the firn column at WAIS Divide with peak values in the ~~convective zone~~SMZ and the deep firn (Fig. ~~14~~13).

High modified Péclet numbers in the ~~convective zone~~SMZ are caused primarily by large D_e values, and high modified Péclet numbers in the LIZ are mostly the result of low molecular diffusivities. Kawamura et al. (2013) showed analytically that relative kinetic isotope fractionation depends on the ratio of eddy diffusivity to molecular diffusivity, but the role of advection was neglected due to near-zero accumulation rates at the Megadunes site. The absolute difference in kinetic isotope fractionation (i.e. ϵ') should be greatest when the product of the modified Péclet numbers of both isotopes is near one. In line with these theoretical predictions, we observe almost no further isotopic enrichment of $\delta^{15}N$ in the lock-in zone when barometric pumping is included in the model and Pe $\gg$ 1 (Figs. ~~8~~ 7 & ~~14~~13). The largest changes of ϵ' occur in the 2D model when the product of the modified Péclet numbers ~~the Péclet number~~ is within approximately 1-2 orders of magnitude of unity. ~~The~~ This region is illustrated by the vertical grey bar in Fig. ~~14~~13, which contains the ~~convective~~ SMZ~~zone~~ as well as the ~~region just above the~~beginning of the LIZ where non-fractionating mixing is of similar magnitude as molecular diffusion.

With active barometric pumping and centimetre-scale layering, the product of the modified Péclet numbers at the bottom of the LIZ becomes so large that ϵ' stops to decrease entirely in our model. If barometric pumping is neglected instead, the modified Péclet numbers in the layered 2D model are considerably lower in the LIZ and some gravitational and kinetic fractionation persists (i.e., $\delta^{15}N$ and ϵ' continue to change gradually). Therefore, barometric pumping leads to slightly weaker rather than stronger differential kinetic fractionation at the COD of WAIS Divide in contrast to expectations (Buizert and Severinghaus, 2016). Furthermore, ~~L~~layering and barometric pumping in the model seem to be insufficient to obtain the full ~5 – 23 per meg per amu range of~~extreme~~ ϵ'_{Kr} values ~~of ϵ'_{Kr} (or ^{86}Kr excess), observed~~ measured in the WAIS Divide ice core record~~.~~ (WAIS Divide Project Members, 2015; Bereiter et al., 2018). Instead, other, unresolved (i.e., subgrid-scale) processes may be the reason for the large observed disequilibrium. Establishing a straightforward relationship between disequilibrium and surface pressure variability using firn air models alone may not be possible without more observational data.~~ ^{86}Kr excess. For example, on the pore level, advective flows may be channelled into wider pores because the hydraulic conductance scales with the fourth power of the pore radius, whereas the diffusive conductance only depends on the square of the pore radius as indicated by the Hagen–Poiseuille equation (Buizert and Severinghaus, 2016). On small scales, Fick's law may also not be the correct relation to represent the physical process of diffusion. The mean square displacement in the disordered firn medium is not necessarily linearly depend on the product of diffusivity and time and we suggest other models of diffusion should be explored. Buizert and Severinghaus (2016) hypothesize that ^{86}Kr excess may be primarily produced by barometric pumping in the deep firn and could thus be used as a measure of paleo storminess in ice core records. Our findings suggest that establishing a straightforward relationship between ^{86}Kr excess and surface pressure variability using firn air models alone may not be possible without more observational data.

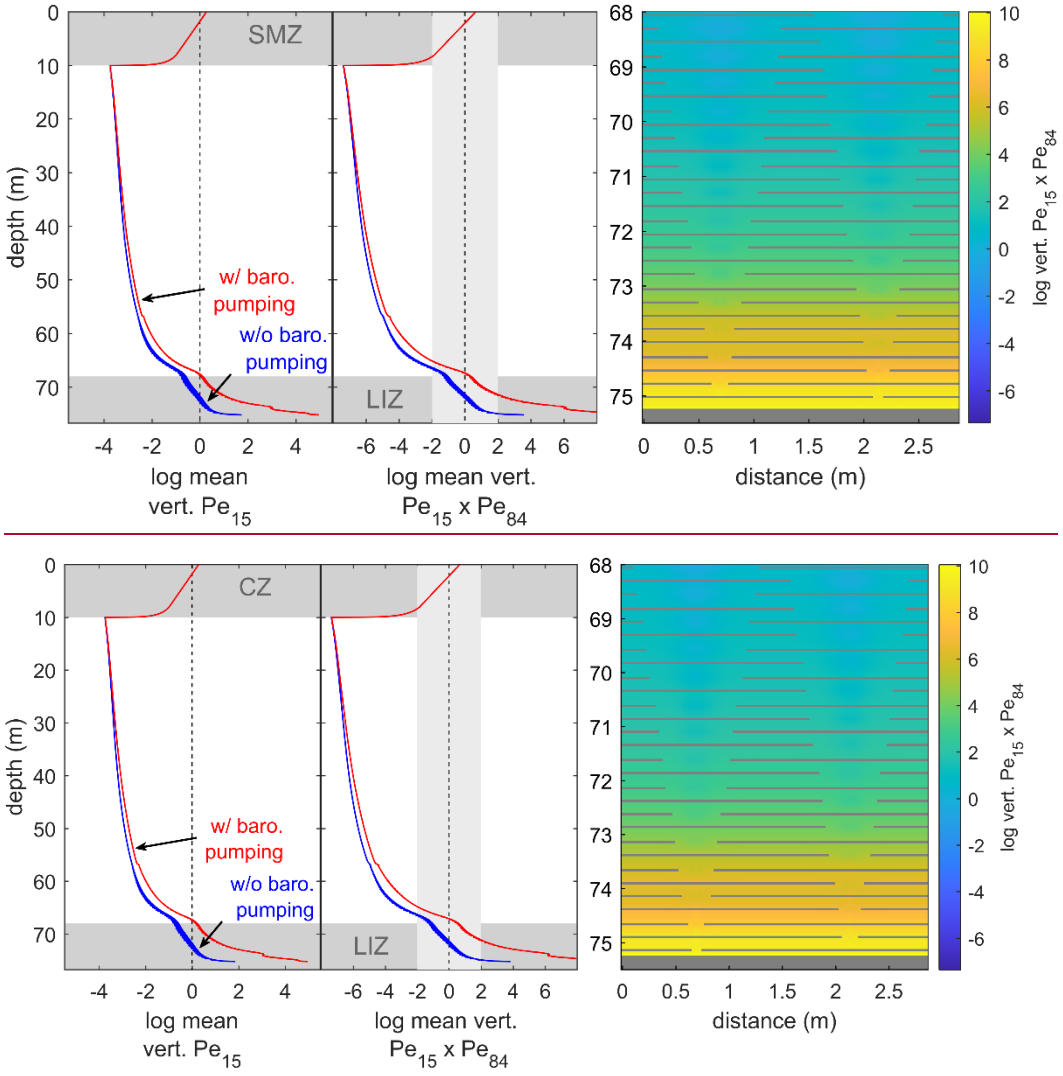

Figure 13~~14~~. The balance of fractionating and non-fractionating mixing at WAIS Divide. The left panel illustrates the horizontally averaged modified Péclet number of $\delta^{15}N$ (Pe_{15}, see text). Blue and red lines show results from the 2D models with and without barometric pumping. The strength of dispersive mixing in the calculations is given by the mean barometric pumping flow velocities at the site. The middle panel displays the product of the modified Péclet numbers for $\delta^{15}N$ and $^{84}Kr/^{28}N_2$ (Pe_{84}). The region where ϵ' changes with depth should be greatest (i.e., where the product of the modified Péclet numbers is near one) is highlighted by a grey bar. The right panel provides a magnified 2D map of this -Péclet number product in the LIZ. ~~Note that the Péclet number becomes infinite in the region below the COD and at layers where molecular diffusivities are zero. These regions are not considered when taking horizontal averages and are coloured grey in the right panel for illustratory purposes.~~

4.2 Diffusive fractionation

Strong kinetic isotope fractionation ~~was~~ can also be observed for trace gases that experience~~d~~ large changes in the atmospheric mixing ratio while the atmospheric isotope ratios remain~~ed~~ constant (Trudinger et al., 1997; Buizert et al., 2013). As the concentration of a trace gas increases, ~~the~~ isotopologues of the gas migrate into the firn column at different speeds because of

small differences in their masses and diffusivities. This results in a relative depletion of the slower diffusing isotopologue with depth called diffusive fractionation (Trudinger et al., 1997). During periods of abrupt CH_4 ~~release or sequestration~~change, diffusive fractionation commonly amounts to a relevant correction in ice core studies (Trudinger et al., 1997; Buizert et al., 2013). Diffusive fractionation of δ^{13}C-CH_4 is strong, and poorly constrained by models, to the degree that it prohibits the reliable atmospheric reconstruction of this parameter from firn air measurements (Sapart et al., 2013). Since ~~D~~diffusive fractionation is ~~another~~ a type of kinetic fractionation, it ~~and~~ can be tested in our model. We assume a constant atmospheric $^{13}C/^{12}C$ isotope ratio of 1.1147302 % for CO_2 (i.e., δ^{13}C-CO_2 = -8 ‰) and 1.0709052 % for CH_4 (i.e., δ^{13}C-CH_4 = -47 ‰), respectively. Thermal fractionation and gravitational settling are neglected to ~~highlight only~~isolate the impact of the atmospheric mixing ratio change. The model including barometric pumping calculates δ^{13}C-CO_2 and δ^{13}C-CH_4 values depleted by up to ~0.2 ‰ and ~~1.97~~2 ‰ relative to the atmosphere in the WAIS Divide LIZ at the time of firn air sampling (Fig. ~~15~~14). Without barometric pumping, delta values are notably higher because molecular diffusion is stronger, and the dispersive mixing no longer smoothes out the profile in the deep firn.

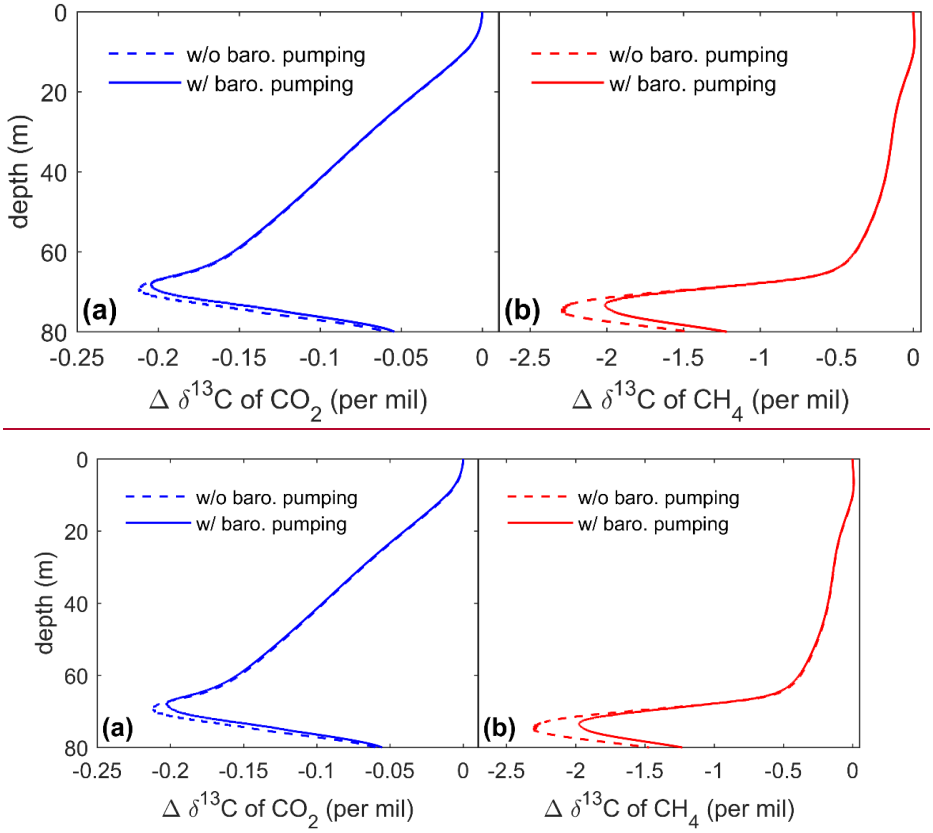

Figure ~~14~~15. Diffusive fractionation effect at the time of sampling at WAIS Divide on δ^{13}C of (a) CO_2 and (b) CH_4. Atmospheric mixing ratios of $^{12}CO_2$, $^{13}CO_2$, $^{12}CH_4$ and $^{13}CH_4$ were obtained from atmospheric trace gas histories used to drive the firn air model (see SI) and assuming constant atmospheric isotope ratios of -8 ‰ and -47 ‰ for δ^{13}C-CO_2 and δ^{13}C-CH_4, respectively. Firn air values are presented as the difference from the constant atmospheric isotope ratios.

4.3 Predicting disequilibrium

Past mean ocean temperature can be estimated from the noble gas concentrations in ice core bubbles (Headly and Severinghaus, 2007; Ritz et al., 2011; Bereiter et al., 2018). On glacial-interglacial timescales, ~~the~~ atmospheric concentrations of noble gases are ~~exclusively~~ primarily controlled by gas dissolution in the ocean. Because the temperature sensitivity of solubility is different for each gas, measurements of noble gas ratios in ice cores can be used to obtain a signal of integrated ocean temperature. However, as for any gas, the trace gas concentrations in bubbles must first be corrected for alterations of the atmospheric signal in the firn. In a recently published deglacial mean ocean temperature reconstruction, the WAIS Divide noble gas ice core record was corrected for gravitational fractionation and thermal fractionation using $\delta^{40}Ar/^{36}Ar$ measurements and a firn temperature gradient estimate (Bereiter et al., 2018). The authors further noted that different degrees of deviation from gravitational equilibrium (i.e., disequilibrium) can bias the gravitational fractionation correction applied to the raw noble gas record, which may lead to a cold bias of ~0.3°C in Holocene and LGM temperatures. Disequilibrium effects of -287.5 per meg for Kr/N_2, -833.3 per meg for Xe/N_2 and -545.7 per meg for Xe/Kr simulated by our model correspond to absolute temperature biases of 0.33 °C, 0.41 °C, and 0.45 °C, respectively, following the method of Bereiter et al. (2018). Because the magnitude of disequilibrium depends on firn properties and accumulation rate, glacial-interglacial changes in environmental boundary conditions may also affect the magnitude of disequilibrium in firn and thus the size of the relative deglacial temperature change estimated from noble gases.

In an attempt to compensate implicitly for disequilibrium effects and gravitational settling at the same time, it has been suggested that the elemental ratios Kr/N_2 and Xe/N_2 in bubbles should be corrected by subtracting krypton or xenon isotope ratios, respectively (Headly, 2008). ~~The hope is~~This would assume that krypton and xenon isotopes may be influenced similarly by the processes responsible for creating disequilibrium in Kr/N_2 and Xe/N_2. Therefore, this approach may compensate for disequilibrium effects and gravitational settling simultaneously, but it has been untested in models so far. The ϵ' values ~~modelled here~~ simulated here allow us to evaluate this method quantitatively. We use a linear fit to predict ~~the~~ ϵ'_{Kr/N_2} from ϵ'_{Kr}. The linear fit yields good agreement with the modelled ϵ'_{Kr} over the whole firn column (R^2>0.998), indicating that the scaling between ϵ' values is nearly independent of depth. We find that (mass-normalized) ϵ'_{Kr/N_2} should be approximately 75 % of ~~the~~ (mass-normalized) ϵ'_{Kr} at the WAIS Divide site. Scaling relationships for other isotope and element pairs are shown in Table 1 and are equally robust. Moreover, our results show that the source of disequilibrium is irrelevant ~~to~~ for the correction for the macroscopic processes represented in our model. Advection and convective or dispersive mixing show the same scaling relationships for ϵ'. At Law Dome DSSW20K, the calculated ratio of ϵ'_{Kr/N_2} and ϵ'_{Kr} is at 75.9 % almost identical to the result at WAIS Divide. Sensitivity tests with the 1D analytical model presented in Appendix A demonstrate that the disequilibrium scaling relationship between Kr isotopes and Kr/N_2 is robust to within $\pm$ 5~~%~~ % over a wide parameter range of molecular diffusivity, eddy diffusivity and advection velocity. Uncertainties become largest in the extreme case when ϵ'_{Ar}, the lowest simulated ϵ' value, is used to predict $\epsilon'_{Xe/Kr}$, the highest simulated ϵ' value, but they never exceed $\pm$ 25~~%~~ %.

This suggests that the same scaling relationship between ϵ'_{Kr/N_2} and ϵ'_{Kr} may be assumed to ~~be used~~hold ~~at~~ for any ~~firn sampling~~ice core site without introducing large biases. ϵ'_{Kr} and ϵ'_{Xe} from combined measurements of $\delta^{15}N$, $\delta^{86}Kr/^{82}Kr$ and $\delta^{136}Xe/^{129}Xe$ in ice cores could be used to predict the disequilibrium effects on noble elemental ratios (i.e., ϵ'_{Kr/N_2}, ϵ'_{Xe/N_2} and $\epsilon'_{Xe/Kr}$) and allows us to make a gas-specific gravitational correction. Although predicted ϵ'_{Kr} values at WAIS Divide are close to the current analytical uncertainty of the $^{86}Kr/^{82}Kr$ measurement, correcting for kinetic fractionation and disequilibrium will become advisable with future improvements in precision and may improve mean ocean temperature reconstructions.

Table 1. ϵ' scaling factor in the 2D model with barometric pumping between different element and isotope ratios from linear regression of ϵ' value pairs at all depths. $R^2 > 0.996$ for all relationships.

Predictor: isotope ratio	**Response: time-variable atmospheric gas ratios**		
	ϵ'_{Kr/N_2}	$\epsilon'_{Xe/Kr}$	ϵ'_{Xe/N_2}
ϵ'_{Ar}	3.94	8.74	6.16
ϵ'_{Kr}	0.75	1.66	1.17
ϵ'_{Xe}	0.54	1.19	0.84

5 Conclusions

We developed a two-dimensional firn air transport model that explicitly represents tortuosity in the firn column through migrating layers of reduced permeability. The idealized representation of firn layering is physically motivated and may illustrate the impact of firn density anomalies (i.e., summer vs winter firn or wind crusts) on gas transport. The model also accounts for thermal fractionation, a ~~convective~~ surface mixed zone, and surface pressure-forced barometric pumping. Dispersive mixing ~~resulting from~~as a result of barometric pumping is constrained in the model by previously published parameterizations and not subject to tuning. Simulations of the $\delta^{15}N$ profile at WAIS Divide show that extensive horizontal diffusion through the tortuous firn structure is required by the discontinuous layers. This limits the effective vertical diffusion of gases at depth. However, layering alone ~~cannot~~ does not fully prevent gravitational enrichment of isotopes in the deep firn ~~completely~~. Similarly, the effect of barometric pumping alone is insufficient to obtain agreement with observations. The combination of barometric pumping with layering, in contrast, leads to amplified dispersive mixing. This is due to high ~~by~~ velocity focusing in layer openings and leads to a more natural emergence of a lock-in zone in the model.

Previous studies have shown that d~~D~~ownward advection, convective mixing and dispersive mixing all hinder trace gases in reaching the isotope ratios expected from gravitational settling (e.g., Severinghaus et al., 2010; Kawamura et al., 2013; Buizert and Severinghaus, 2016;). K~~This k~~inetic fractionation is strongest for slow~~-~~ diffusing gases and increases with firn column ~~height~~depth. Our numerical experiments show ~~clearly~~ that barometric pumping leads to increased isotopic disequilibrium in the firn column. However, our simulations~~experiments~~ fail to account for the ~~large~~ full range of ^{86}Kr excess observed in the WAIS Divide core, as well as for the relatively weak $\delta^{15}N$ enrichment seen at DSSW20K, suggesting that these effects are not caused by the presence of layering (as previously suggested) and that their origin must be sought

elsewhere. We further find robust scaling relationships between the magnitude of disequilibrium in different noble gas isotope and elemental ratios. Our results suggest that, to first order, these scaling relationships are independent of depth in the firn column and independent of the reason for disequilibrium for the process represented in the model (i.e., dispersive mixing, advection or convective mixing). Thus, a correction that accounts for differential kinetic fractionation may be applied to measured observed noble gas ratios in the reconstruction of mean ocean temperature ~~to account for kinetic fractionation~~.

6 Appendices

6.1 Appendix A: An analytical solution for simplified firn air transport

Here, we seek an analytical solution to the following idealized scenario of firn air transport: firn air advection, diffusion, and dispersion in one dimension. In this case, vertical trace gas migration relative to the major gas nitrogen is governed by ~~the Eq. (A1):~~

$$\tilde{s}\frac{\partial q}{\partial t} = \frac{\partial}{\partial z}\left[\tilde{s}D_m\left(\frac{\partial q}{\partial z} - \frac{\Delta m\, g}{R\,T}q + \Omega\frac{\partial T}{\partial z}q\right) + \tilde{s}D_e\frac{\partial q}{\partial z}\right] - \tilde{s}w\frac{\partial q(z,t)}{\partial z}, \quad \text{(A1)}$$

with ~~$q \equiv \delta + 1$ the ratio of an isotope to 28N2 relative to a standard, $\tilde{s} \equiv s_{op}\exp\left(\frac{\Delta m g z}{RT}\right)$ the pressure – corrected open porosity (m3 m – 3), D_m~~ and D_e the molecular and eddy diffusivity (m² s^{-1})~~, Ω the thermal diffusion sensitivity (K^{-1}),~~ and w the effective vertical air advection velocity due to snow accumulation and pore compression (m s^{-1}) (e.g., Schwander et al., 1993; Rommelaere et al., 1997; Trudinger et al., 1997; Severinghaus et al., 2010; Buizert et al., 2012; Kawamura et al., 2013). The five terms on the right-hand side of Eq. (A1) represent Fickian diffusion, gravitational settling, thermal fractionation, mass-independent dispersion and gas advection (from left to right). A Dirichlet ~~(i.e., known value)~~ boundary condition is chosen at the top of the firn column and represents the well-mixed atmosphere (i.e., $q(0) \equiv 0$). The bottom boundary condition is given by a Neumann boundary condition allowing only an advective flux to leave the domain ($\tilde{s}(D_m + D_e)\frac{\partial q}{\partial z} - \tilde{s}D_m\left(\frac{\Delta m\, g}{R\,T} - \Omega\frac{\partial T}{\partial z}\right)q \equiv 0 \;@\; z = z(COD)$).

Assuming steady-state and neglecting changes of $\tilde{s}$, D_m, D_e and w with depth, Eq. (A1) reduces to (Severinghaus et al., 2010)

$$\frac{\partial q}{\partial t} \equiv 0 = (D_m + D_e)\frac{\partial^2 q}{\partial z^2} - D_m(G - \mathcal{T})\frac{\partial q}{\partial z} - w\frac{\partial q}{\partial z}, \quad \text{(A2)}$$

where $G \equiv \frac{\Delta m\, g}{R\,T}$ and $\mathcal{T} \equiv \Omega\frac{\partial T}{\partial z}$ represent the constants in the gravitational and thermal fractionation term.

The solution to Eq. (A2) ~~for~~ yields trace gas profiles above the COD in delta notation ~~takes the form~~

$$\delta = \frac{\exp\left(\frac{D_m(G-\mathcal{T})+w}{D_m+D_e}\,z\right)-1}{\frac{w}{D_m(G-\mathcal{T})}\exp\left(\frac{D_m(G-\mathcal{T})+w}{D_m+D_e}\,z_{COD}\right)+1} \begin{cases} \dfrac{\exp\left(\frac{D_m(G-\mathcal{T})+w}{D_m+D_e}\,z\right)-1}{\frac{w}{D_m(G-\mathcal{T})}\exp\left(\frac{D_m(G-\mathcal{T})+w}{D_m+D_e}\,z_{COD}\right)+1}, & z \le z_{COD} \\ \delta(z_{COD}), & z > z_{COD} \end{cases} \quad \text{(A3)}$$

where $z_{COD} = z(COD)$ (see SI Fig. S2). δ values below the COD are constant. Note that Eq. (A2) only applies to trace gas transport into N_2, not to transport of one trace gas into another trace gas, as discussed in the text. Nevertheless Because $\delta^{15}N$ only requires calculating the transport of the trace gas $^{15}N^{14}N$ into the major gas $^{28}N_2$, the equation can be used as such is to calculate $\delta^{15}N$.

By evaluating some extreme cases, Eq. (A4A3) illustrates a few key points about trace gas transport of $\delta^{15}N$ in firn. Under a large negative temperature gradient (i.e., atmospheric warming, $\mathcal{T} \to -\infty$), $\delta \to \infty$ and thermally sensitive gases are enriched in the firn because the numerator grows faster than the denominator. Similarly, heavier gases ($G \to \infty$) are more strongly fractionated ($\delta \to \infty$) than lighter gases assuming they have the same molecular diffusivity. Advection ($w \to \infty$) and eddy mixing ($D_e \to \infty$) prevent the system from reaching the trace gas concentrations expected from gravitational settling and ultimately force concentrations to be constant ($\delta \to 0$). A lack of molecular diffusion ($D_m \to 0$) leads to the same result ($\delta \to 0$). Naturally, Eq. (A4A3) reduces to the profile of a gravitationally settled gas (i.e., Eq. (1)) when $w \to 0$ and $D_e \to 0$.

6.2 Appendix B: Differential kinetic isotope fractionation in ratios of two different elements

Here we revisit the relative disequilibrium for ratios of two elements as seen in Figs. 12 11 and 1312. First, recall the definition of ϵ' for a ratio of isotopes x and y (indicated by their nominal atomic masses)

$$\epsilon'_{x/y} \equiv \frac{10^{-3}}{m_x - m_y}\ln(q_{x/y}) - \ln(q_{29/28}) = \ln\left(\frac{q_{x/y}^{\frac{10^{-3}}{m_x-m_y}}}{q_{29/28}}\right). \quad \text{(A4)}$$

Equation (3) shows that $q_{x/y}$ is the ratio of q values calculated for the transport of each isotope into $^{28}N_2$ ($q_{x/28}$ and $q_{y/28}$). $q_{x/28}$ (or $q_{y/28}$) may also be expressed in reference to nitrogen using the ϵ' value for the isotope

$$\frac{10^{-3}}{m_x - m_{28}}\ln(q_{x/28}) = \ln(q_{29/28}) + \epsilon'_{x/28} \quad \rightarrow \quad q_{x/28} = \left(q_{29/28}\cdot\exp(\epsilon'_{x/28})\right)^{10^3(m_x-m_{28})} \ln\left(q_{x/28}^{\frac{1}{m_x-m_{28}}}\right) \quad \text{(A5)}$$

$$= \ln(q_{29/28}) + \epsilon'_{x/28} = \ln\left(q_{29/28}\cdot\exp(\epsilon'_{x/28})\right).$$

Note that ϵ' by definition is already mass-normalized. It follows from Eqs. (3), (A4) and (A5) that

$$\epsilon'_{x/y} = \ln\left(\frac{\left(\frac{q_{x/28}}{q_{y/28}}\right)^{\frac{10\text{^}-3}{m_x-m_y}}}{q_{29/28}}\right) = \ln\left(\frac{\left(\frac{\left(q_{29/28}\cdot\exp(\epsilon'_{x/28})\right)^{m_x-m_{28}}}{\left(q_{29/28}\cdot\exp(\epsilon'_{y/28})\right)^{m_y-m_{28}}}\right)^{\frac{1}{m_x-m_y}}}{q_{29/28}}\right). \quad \text{(A6)}$$

Equation (A6) may be rewritten to yield

$$\epsilon'_{x/y} = \frac{m_x-m_{28}}{m_x-m_y}\left[\ln(q_{29/28}) + \epsilon'_{x/28}\right] - \frac{m_y-m_{28}}{m_x-m_y}\left[\ln(q_{29/28}) + \epsilon'_{x/28}\right] - \ln(q_{29/28}). \quad \text{(A7)}$$

Because the terms containing $q_{29/28}$ cancel, we obtain a straightforward expression to find ϵ' for any isotope ratio from the ϵ' of two nuclides relative to $^{28}N_2$

$$\epsilon'_{x/y} = \frac{m_x - m_{28}}{m_x - m_y}\epsilon'_{x/28} - \frac{m_y - m_{28}}{m_x - m_y}\epsilon'_{y/28}. \quad \text{(A8)}$$

Analysis of this relationship reveals that disequilibrium should most strongly affect ratios of two heavy isotopes, such as $^{132}Xe/^{84}Kr$, because heavy elements diffuse slower than N_2 (i.e., $\epsilon'_{x/28} \ll 0$) and the mass weighting factor is larger in the first than in the second term (i.e., $\frac{m_x-m_{28}}{m_x-m_y} \gg \frac{m_y-m_{28}}{m_x-m_y}$). ~~As long as no explicit correction for disequilibrium effects is implemented in the determination of mean ocean temperature, this implies that particular caution should be used in interpreting the $^{132}Xe/^{84}Kr$ record at sites with substantial disequilibrium.~~

Although this equation can theoretically predict ϵ' of any isotope ratio from ϵ' of the two isotopes x and y relative to $^{28}N_2$ (i.e., $\epsilon'_{x/28}$ and $\epsilon'_{y/28}$), in practice, this approach will not allow correcting for differential kinetic isotope fractionation. $\epsilon'_{x/28}$ cannot be measured directly and the atmospheric ratio of the noble gas x to nitrogen is not constant over long timescales. Thus, $\epsilon'_{x/28}$ will not only be affected by disequilibrium but will also be influenced by atmospheric variability resulting from gas specific solubility differences (i.e., precisely the mean ocean temperature signals we attempt to reconstruct). Instead we suggest that the scaling relationships provided in Sect. 5.3 can be used to predict the ϵ' of noble gas elemental ratios.

7 Competing interests

The authors declare that they have no conflict of interest.

8 Acknowledgements

We would like to thank Jakob Keck, Alan Seltzer and Ian Eisenman for providing computational resources and insightful discussions on the numerical implementation of firn air transport. Sarah Shackleton has provided helpful comments on the

importance of disequilibrium in mean ocean temperature reconstruction. This work was supported by NSF grants PLR-1543229 and PLR-1543267.

9 References

Alley, R. B. and Koci, B. R.: Recent warming in central Greenland?, Annals of Glaciology, 14, 6–8, 1990.

Battle, M. O., Severinghaus, J. P., Sofen, E. D., Plotkin, D., Orsi, A. J., Aydin, M., Montzka, S. A., Sowers, T. and Tans, P. P.: Controls on the movement and composition of firn air at the West Antarctic Ice Sheet Divide, Atmospheric Chemistry and Physics, 11, 11007–11021, doi:10.5194/acp-11-11007-2011, 2011.

Bereiter, B., Shackleton, S., Baggenstos, D., Kawamura, K. and Severinghaus, J.: Mean global ocean temperatures during the last glacial transition, Nature Publishing Group, 553, 39–44, doi:10.1038/nature25152, 2018.

Buizert, C. and Severinghaus, J. P.: Dispersion in deep polar firn driven by synoptic-scale surface pressure variability, The Cryosphere, 10, 2099–2111, doi:10.5194/tc-2016-148, 2016.

Buizert, C., Martinerie, P., Petrenko, V. V, Severinghaus, J. P., Trudinger, C. M., Witrant, E., Rosen, J. L., Orsi, A. J., Rubino, M., Etheridge, D. M., Steele, L. P., Hogan, C., Laube, J. C., Sturges, W. T., Levchenko, V. A., Smith, A. M., Levin, I., Conway, T. J., Dlugokencky, E. J., Lang, P. M., Kawamura, K., Jenk, T. M., White, J. W. C., Sowers, T., Schwander, J. and Blunier, T.: Gas transport in firn: Multiple-tracer characterisation and model intercomparison for NEEM, Northern Greenland, Atmospheric Chemistry and Physics, 12, 4259–4277, doi:10.5194/acp-12-4259-2012, 2012.

Buizert, C., Sowers, T. and Blunier, T.: Assessment of diffusive isotopic fractionation in polar firn, and application to ice core trace gas records, Earth and Planetary Science Letters, 361, 110–119, doi:10.1016/j.epsl.2012.11.039, 2013.

Colbeck, S. C.: Air Movement in Snow due to Windpumping, Journal of Glaciology, 35(120), 209–213, 1989.

Craig, H., Horibe, Y. and T., S.: Gravitational separation of gases and isotopes in polar ice caps, Science, 242, 1675–1678, 1988.

Dahl-Jensen, D., Morgan, V. I. and Elcheikh, A.: Monte Carlo inverse modelling of the Law Dome (Antarctica) temperature profile, Annals of Glaciology, 29, 145–150, doi:10.3189/172756499781821102, 1999.

Darcy, H.: Les Fontaines Publiques de la Ville de Dijon, Victor Dalmont, Paris., 1856.

Dlugokencky, E. J., Lang, P. M., Mund, J. W., Crotwell, A. M., Crotwell, M. J. and Thoning, K. W.: Atmospheric Carbon Dioxide Dry Air Mole Fractions from the NOAA ESRL Carbon Cycle Cooperative Global Air Sampling Network, 1968-2015, Version: 2016-08-30, 2016a.

Dlugokencky, E. J., Lang, P. M., Crotwell, A. M., Mund, J. W., Crotwell, M. J. and Thoning, K. W.: Atmospheric Methane Dry Air Mole Fractions from the NOAA ESRL Carbon Cycle Cooperative Global Air Sampling Network, 1983-2015, Version: 2016-07-07, 2016b.

Etheridge, D. M., Steele, L. P., Langenfelds, R. L., Francey, R. J., Barnola, J. M. and Morgan, V. I.: Natural and anthropogenic changes in atmospheric CO2 over the last 1000 years from air in Antarctic ice and firn, Journal of Geophysical

Research-Atmospheres, 101(D2), 4115–4128, doi:10.1029/95JD03410, 1996.

Etheridge, D. M., Steele, L. P., Francey, R. J. and Langenfelds, R. L.: Atmospheric methane between 1000 A.D. and present: Evidence of anthropogenic emissions and climatic variability, Journal of Geophysical Research, 103(D13), 15979, doi:10.1029/98JD00923, 1998.

Freeze, R. A. and Cherry, J. A.: Groundwater, Prentice-Hall, Inc., Englewood Cliffs, New Jersey., 1979.

Grachev, A. and Severinghaus, J. P.: Laboratory determination of thermal diffusion constants for 29N2 /28N2 in air at temperatures from -60 to 0° C for reconstruction of magnitudes of abrupt climate changes using the ice core fossil – air paleothermometer, Geochimica et cosmochimica Acta, 67(3), 345–360, 2003a.

Grachev, A. M. and Severinghaus, J. P.: Determining the Thermal Diffusion Factor for 40Ar/ 36Ar in Air To Aid Paleoreconstruction of Abrupt Climate Change, The Journal of Physical Chemistry A, 107, 4636–4642, doi:10.1021/jp027817u, 2003b.

Headly, M.: Krypton and xenon in air trapped in polar ice cores: paleo-atmospheric measurements for estimating past mean ocean temperature and summer snowmelt frequency, University of California, San Diego., 2008.

Headly, M. A. and Severinghaus, J. P.: A method to measure Kr/N2 ratios in air bubbles trapped in ice cores and its application in reconstructing past mean ocean temperature, Journal of Geophysical Research, 112(D19105), 1–12, doi:10.1029/2006JD008317, 2007.

Hörhold, M. W., Laepple, T., Freitag, J., Bigler, M., Fischer, H. and Kipfstuhl, S.: On the impact of impurities on the densification of polar firn, Earth and Planetary Science Letters, 325–326, 93–99, doi:10.1016/j.epsl.2011.12.022, 2012.

Johnsen, S. J.: Stable isotope profiles compared with temperature profiles in firn with historical temperature records, Isotopes and Impurities in Snow and Ice, 388–392, 1977.

Kawamura, K., Severinghaus, J. P., Albert, M. R., Courville, Z. R., Fahnestock, M. A., Scambos, T. A., Shields, E. and Shuman, C. A.: Kinetic fractionation of gases by deep air convection in polar firn, Atmospheric Chemistry and Physics, 13, 11141–11155, doi:10.5194/acp-13-11141-2013, 2013.

Keeling, C. D., Stephen, C., Piper, S. C., Bacastow, R. B., Wahlen, M., Whorf, T. P., Heimann, M. and Meijer, H. A.: Exchanges of atmospheric CO2 and 13CO2 with the terrestrial biosphere and oceans from 1978 to 2000., Global Aspects, SIO Reference Series. Scripps Institution of Oceangraphy, San Diego, 01–06, 83–113, doi:10.1007/b138533, 2001.

Lazzara, M. A., Weidner, G. A., Keller, L. M., Thom, J. E. and Cassano, J. J.: Antarctic Automatic Weather Station Program: 30 Years of Polar Observation, Bulletin of the American Meteorological Society, 93, 1519–1537, doi:10.1175/BAMS-D-11-00015.1, 2012.

Lüthi, D., Le Floch, M., Bereiter, B., Blunier, T., Barnola, J.-M., Siegenthaler, U., Raynaud, D., Jouzel, J., Fischer, H., Kawamura, K. and Stocker, T. F.: High-resolution carbon dioxide concentration record 650,000-800,000 years before present., Nature, 453, 379–382, doi:10.1038/nature06949, 2008.

Mitchell, L. E., Buizert, C., Brook, E. J., Breton, D. J., Fegyveresi, J., Baggenstos, D., Orsi, A., Severinghaus, J., Alley, R. B., Albert, M., Rhodes, R. H., McConnell, J. R., Sigl, M., Maselli, O., Gregory, S. and Ahn, J.: Observing and modeling the

influence of layering on bubble trapping in polar firn, Journal of Geophysical Research Atmospheres, 120, 2558–2574, doi:10.1002/2014JD022766, 2015.

Van Ommen, T. D., Morgan, V. I., Jacka, T. H., Woon, S. and Elcheikh, A.: Near-surface temperatures in the Dome Summit South (Law Dome, East Antarctica) borehole, Annals of Glaciology, 29, 141–144, doi:doi:10.3189/172756499781821382, 1999.

Orsi, A. J., Cornuelle, B. D. and Severinghaus, J. P.: Little Ice Age cold interval in West Antarctica: Evidence from borehole temperature at the West Antarctic Ice Sheet (WAIS) Divide, Geophysical Research Letters, 39(L09710), 1–7, doi:10.1029/2012GL051260, 2012.

Orsi, A. J., Kawamura, K., Fegyveresi, J. M., Headly, M. A., Alley, R. B. and Severinghaus, J. P.: Differentiating bubble-free layers from Melt layers in ice cores using noble gases, Journal of Glaciology, 61(227), 585–594, doi:10.3189/2015JoG14J237, 2015.

Petit, R. J., Jouzel, J., Raynaud, D., Barkov, N. I., Barnola, J.-M., Basile, I., Bender, M., Chappellaz, J., Davis, M., Delaygue, G., Delmotte, M., Kotyakov, V. M., Legrand, M., Livenkov, V. Y., Lorius, C., Pépin, L., Ritz, C., Saltzman, E. and Stievenard, M.: Climate and atmospheric history of the past 420,000 years from the Vostok ice core, Antarctica, Nature, 399, 429–413, doi:10.1038/20859, 1999.

Ritz, S. P., Stocker, T. F. and Severinghaus, J. P.: Noble gases as proxies of mean ocean temperature: Sensitivity studies using a climate model of reduced complexity, Quaternary Science Reviews, 30, 3728–3741, doi:10.1016/j.quascirev.2011.09.021, 2011.

Rommelaere, V., Arnaud, L. and Barnola, J.-M.: Reconstructing recent atmospheric trace gas concentrations from polar firn and bubbly ice data by inverse methods, Journal of Geophysical Research, 102(D25), 30069–30083, 1997.

Sapart, C. J., Martinerie, P., Witrant, E., Chappellaz, J., Van De Wal, R. S. W., Sperlich, P., Van Der Veen, C., Bernard, S., Sturges, W. T., Blunier, T., Schwander, J., Etheridge, D. and Röckmann, T.: Can the carbon isotopic composition of methane be reconstructed from multi-site firn air measurements?, Atmospheric Chemistry and Physics, 13, 6993–7005, doi:10.5194/acp-13-6993-2013, 2013.

Schwander, J.: The Transformation of Snow to Ice and the Occlusion of Gases, The Environmental Record in Glaciers and Ice Sheets, 53–67, 1989.

Schwander, J., Stauffer, B. and Sigg, A.: Air mixing in firn and the age of the air at pore close-off, Annals of Glaciology, 10, 141–145, 1988.

Schwander, J., Barnola, J.-M., Andrié, C., Leuenberger, M., Ludin, A., Raynaud, D. and Stauffer, B.: The age of the air in the firn and the ice at Summit, Greenland, Journal of Geophysical Research, 98, 2831–2838, doi:10.1029/92JD02383, 1993.

Severinghaus, J. P. and Battle, M. O.: Fractionation of gases in polar ice during bubble close-off: New constraints from firn air Ne, Kr and Xe observations, Earth and Planetary Science Letters, 244, 474–500, doi:10.1016/j.epsl.2006.01.032, 2006.

Severinghaus, J. P., Grachev, A. and Battle, M.: Thermal fractionation of air in polar firn by seasonal temperature gradients, Geochemistry, Geophysics, Geosystems, 2(2000GC000146), 1–24, doi:10.1029/2000GC000146, 2001.

Severinghaus, J. P., Albert, M. R., Courville, Z. R., Fahnestock, M. A., Kawamura, K., Montzka, S. A., Mühle, J., Scambos, T. A., Shields, E., Shuman, C. A., Suwa, M., Tans, P. and Weiss, R. F.: Deep air convection in the firn at a zero-accumulation site, central Antarctica, Earth and Planetary Science Letters, 293, 359–367, doi:10.1016/j.epsl.2010.03.003, 2010.

Sowers, T., Bender, M. and Raynaud, D.: Elemental and Isotopic Composition of Occluded O2 and N2 in Polar Ice, Journal of Geophysical Research, 94(D4), 5137–5150, doi:10.1029/JD094iD04p05137, 1989.

Trudinger, C. M., Enting, I. G., Etheridge, D. M., Francey, R. J., Levchenko, V. A., Steele, L. P., Raynaud, D. and Arnaud, L.: Modeling air movement and bubble trapping in firn, Journal of Geophysical Research: Atmospheres, 102(D6), 6747–6763, doi:10.1029/96JD03382, 1997.

Trudinger, C. M., Etheridge, D. M., Rayner, P. J., Enting, I. G., Sturrock, G. A. and Langenfelds, R. L.: Reconstructing atmospheric histories from measurements of air composition in firn, Journal of Geophysical Research Atmospheres, 107(24), 1–13, doi:10.1029/2002JD002545, 2002.

Trudinger, C. M., Enting, I. G., Rayner, P. J., Etheridge, D. M., Buizert, C., Rubino, M., Krummel, P. B. and Blunier, T.: How well do different tracers constrain the firn diffusivity profile?, Atmospheric Chemistry and Physics, 13, 1485–1510, doi:10.5194/acp-13-1485-2013, 2013.

WAIS Divide Project Members: Precise interpolar phasing of abrupt climate change during the last ice age, Nature, 520, 661–665, doi:10.1038/nature14401, 2015.

Weller, G. and Schwerdtfeger, P.: Thermal properties and heat transfer processes of low-temperature snow, in Meteorological Studies at Plateau Station, Antarctica, vol. 25, edited by P. C. Dalrymple, A. J. Riordan, A. Riordan, A. J. Riordan, and R. C. L. andUwe R. Weller, H. H. Lettau, H. Lettau, L. A. Stroschein, L. S. Kundla, Leander A. Stroschein, M. Kuhn, Peter Schwerdtfeger, American Geophysical Union., 1977.

Supplementary Information to "The influence of layering and barometric pumping on firn air transport in a 2D model"

Benjamin Birner[1], Christo Buizert[2], Till J.W. ~~Wagner[1]~~ Wagner[3] and Jeffrey P. Severinghaus[1]

[1]Scripps Institution of Oceanography, University of California San Diego, La Jolla, CA 92093, USA
[2]College of Earth, Ocean and Atmospheric Sciences, Oregon State University, Corvallis, OR 97331, USA
[3]Department of Physics and Physical Oceanography, University of North Carolina at Wilmington, NC 28401, USA

Correspondence to: Benjamin Birner (bbirner@ucsd.edu)

1 2D trace gas transport model

1.1 Numerical integration scheme

Trace gas migration in firn is governed by the following partial differential ~~Eq. (S1)~~equation (Eq. (2) in main text)~~:~~

$$\tilde{s}\frac{\partial q}{\partial t} = \vec{\nabla}\cdot\left[\tilde{s}\boldsymbol{D}_m\left(\vec{\nabla}q - \vec{G}\,q + \Omega\frac{\partial T}{\partial z}q\,\hat{k}\right)\right] + \vec{\nabla}\cdot\left[\tilde{s}\boldsymbol{D}_d\vec{\nabla}q\right] - \left(\tilde{s}\,\vec{\mathrm{u}}\right)\cdot\vec{\nabla}q\,, \tag{S1}$$

where $\vec{G} \equiv \frac{\Delta m\,\vec{g}}{R\,T}$, $q \equiv \frac{\delta}{1000} + 1$ is the trace gas or isotope mixing ratio, $\tilde{s} \equiv s_{op}\exp\left(\frac{\mathrm{M}\,g}{R\,T}z\right)$ pressure-corrected open porosity ($m^3\,m^{-3}$), T temperature (K), Δm isotope mass difference (kg mol^{-1}) to the mass of air M (kg mol^{-1}), $\vec{g}$ gravitational acceleration (m s^{-2}), R the fundamental gas constant (J mol^{-1} K^{-1}), $\vec{u}$ air advection velocity due to snow accumulation, pore compression and barometric pumping (m s^{-1}), and Ω thermal diffusion sensitivity (K^{-1}). $\boldsymbol{D}_m$ is the molecular diffusivity and $\boldsymbol{D}_d$ is the dispersion tensor (m^2 s^{-1}). $\boldsymbol{D}_m$ has different entries on the diagonal to represent different strengths of molecular diffusion in the vertical and horizontal direction. Similarly, $\boldsymbol{D}_d$ is simplified to an "eddy diffusivity", $\boldsymbol{D}_e$, acting in vertical and horizontal direction as described in the text. $\tilde{s} = \tilde{s}(z)$, $T = \mathrm{T}(\mathrm{z},\mathrm{t})$, and $q = q(x,z,t)$ are scalar fields. Furthermore, $\vec{\mathrm{u}} = u(x,z,t)\,\hat{\imath} + w(x,z,t)\,\hat{k}$ is a vector field and $\vec{\nabla} \equiv \frac{\partial}{\partial x}\hat{\imath} + \frac{\partial}{\partial z}\hat{k}$ is the gradient operator in 2D.

Equation (S1) is discretized using a Crank-Nicolson time stepping scheme and central difference approximations derived from flux balance on an Arakawa C (i.e., staggered; Fig. S1) grid as follows:

$$\tilde{s}(z)\frac{q(x,z,t+\Delta t) - q(x,z,t)}{\Delta t} = \frac{1}{2}\left[(\mathbf{A}+\mathbf{B})_{|t+\Delta t}\,q(x,z,t+\Delta t) + (\mathbf{A}+\mathbf{B})_{|t}\,q(x,z,t)\right], \tag{S2}$$

where

$$\mathbf{A}_{|t}\, q(x,z,t) \equiv \frac{-\tilde{s}u\left(x+\frac{\Delta x}{2},z,t\right)}{2\Delta x}\, q(x+\Delta x,z,t) + \frac{\tilde{s}u\left(x-\frac{\Delta x}{2},z,t\right)}{2\Delta x}\, q(x-\Delta x,z,t) - \frac{\tilde{s}w\left(x,z+\frac{\Delta z}{2},t\right)}{2\Delta z}\, q(x,z+\Delta z,t) + \frac{\tilde{s}w\left(x,z-\frac{\Delta z}{2},t\right)}{2\Delta z}\, q(x,z-\Delta z,t) + \left[\frac{\tilde{s}u\left(x+\frac{\Delta x}{2},z,t\right) - \tilde{s}u\left(x-\frac{\Delta x}{2},z,t\right)}{2\Delta x} + \frac{\tilde{s}w\left(x,z+\frac{\Delta z}{2},t\right) - \tilde{s}w\left(x,z-\frac{\Delta z}{2},t\right)}{2\Delta z}\right] q(x,z,t)\,, \tag{S3}$$

$$\mathbf{B}_{|t}\, q(x,z,t) \equiv \frac{\tilde{s}D_h^*\left(x+\frac{\Delta x}{2},z,t\right)}{\Delta x^2} q(x+\Delta x,z,t) + \frac{\tilde{s}D_h^*\left(x-\frac{\Delta x}{2},z,t\right)}{\Delta x^2} q(x-\Delta x,z,t) + \left[\frac{\tilde{s}D_v^*\left(x,z+\frac{\Delta z}{2},t\right)}{\Delta z^2} - G\,\frac{\tilde{s}D_{m,v}\left(x,z+\frac{\Delta z}{2},t\right)}{2\Delta z} + \frac{\tilde{s}D_{m,v}\Omega\left(x,z+\frac{\Delta z}{2}\right)\left(\frac{T(x,z+\Delta z,t)-T(x,z,t)}{\Delta z}\right)}{2\Delta z}\right] q(x,z+\Delta z,t) + \left[\frac{\tilde{s}D_v^*\left(x,z-\frac{\Delta z}{2},t\right)}{\Delta z^2} + G\,\frac{\tilde{s}D_{m,v}\left(x,z-\frac{\Delta z}{2},t\right)}{2\Delta z} - \frac{\tilde{s}D_{m,v}\Omega\left(x,z-\frac{\Delta z}{2}\right)\left(\frac{T(x,z,t)-T(x,z-\Delta z,t)}{\Delta z}\right)}{2\Delta z}\right] q(x,z-\Delta z,t) + \left[-\frac{\tilde{s}D_h^*\left(x+\frac{\Delta x}{2},z,t\right)+\tilde{s}D_h^*\left(x-\frac{\Delta x}{2},z,t\right)}{\Delta x^2} - \frac{\tilde{s}D_v^*\left(x,z+\frac{\Delta z}{2},t\right)+\tilde{s}D_v^*\left(x,z-\frac{\Delta z}{2},t\right)}{\Delta z^2} + G\,\frac{\tilde{s}D_{m,v}\left(x,z-\frac{\Delta z}{2},t\right)-\tilde{s}D_{m,v}\left(x,z+\frac{\Delta z}{2},t\right)}{2\Delta z} + \frac{\tilde{s}D_{m,v}\Omega\left(x,z+\frac{\Delta z}{2}\right)\left(\frac{T(x,z+\Delta z,t)-T(x,z,t)}{\Delta z}\right)-\tilde{s}D_{m,v}\Omega\left(x,z-\frac{\Delta z}{2}\right)\left(\frac{T(x,z,t)-T(x,z-\Delta z,t)}{\Delta z}\right)}{2\Delta z}\right] q(x,z,t)\,, \tag{S4}$$

with $\boldsymbol{D}^* \equiv \boldsymbol{D}_e + \boldsymbol{D}_m$ a combination of eddy and molecular diffusivity in vertical (D_v^*) and horizontal (D_h^*) direction, Δt time step of integration (s), Δz vertical grid spacing (m), and Δx horizontal grid spacing (m). Here q is an Nx1 vectors where N is the number of grid cells; **A** and **B** are banded square-matrices of dimensions NxN that represent the advection operator (i.e., the sum of the three velocity components) and the diffusion operator (Fickian diffusion, eddy diffusion, thermal diffusion, and gravitational fractionation), respectively. The two matrices have entries on the diagonal as well as four off-diagonals corresponding to the grid points above, below, to the left and to the right. Because **A** and **B** are also dependent on time, subscripts indicate the time step in Eqs. (S3) and (S4). Equations (S2) – (S4) form a system of linear equations describing the change in time of q at all spatial points. Rearranging Eq. (S2) yields

$$q(x,z,t+\Delta t) = \left[\tilde{s}(z)\,\mathbf{I} - (\mathbf{A}+\mathbf{B})_{|t+\Delta t}\right]^{-1}\left[\frac{\Delta t}{2}(\mathbf{A}+\mathbf{B})_{|t} + \tilde{s}(z)\,\mathbf{I}\right] q(x,z,t)\,, \tag{S5}$$

with **I** the identity matrix, which can be stepped forward in time. In the limit of no horizontal transport and constant coefficients ($\tilde{s}$, D_m, D_e and $\vec{u}$ constant), we find good agreement between ~~our~~ this numerical model and analytical solutions for a simple 1D model (Appendix A, Fig. S2). δ^{15}N profiles from the model run at 5x higher temporal resolution indicate that the error introduced by a coarser time step converges and is small (~0.5 per meg) relative to the signal in the deep firn (~5 per meg) (Fig. S3).

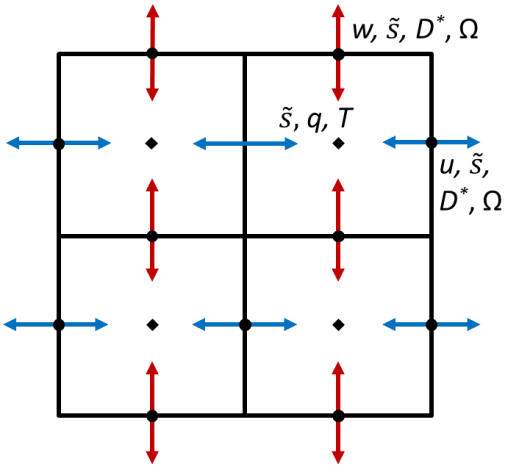

Figure S1. Schematic of how~~the distribution of~~ variables q, T, u, $\tilde{s}$, D^*, Ω and w are defined on the staggered grid.

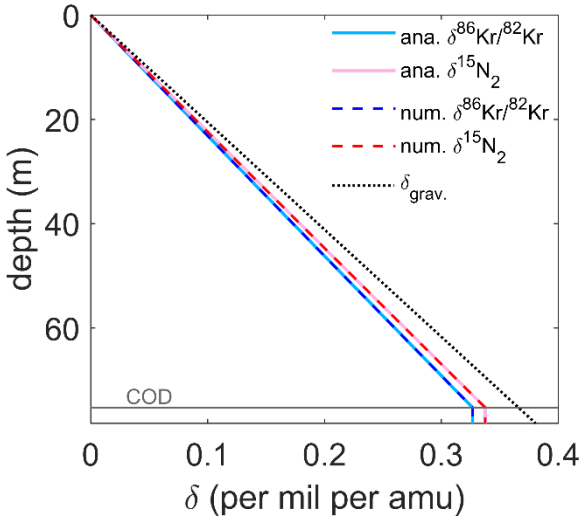

Figure S2. Comparison of 1D analytical solutions (Appendix A, solid lines) and numerical model output (dashed coloured lines). Here $w = 10^{-9}$ m s^{-1}, $D_e = 6 \times 10^{-7}$ m^2 s^{-1} and molecular diffusivity of CO_2 $D_m = 6 \times 10^{-6}$ m^2 s^{-1} up to the COD. The dashed black line shows the gravitational settling equilibrium, i.e., the steady-state solution for each isotope pair neglecting advection and non-fractionating mixing processes (δ_{grav}).

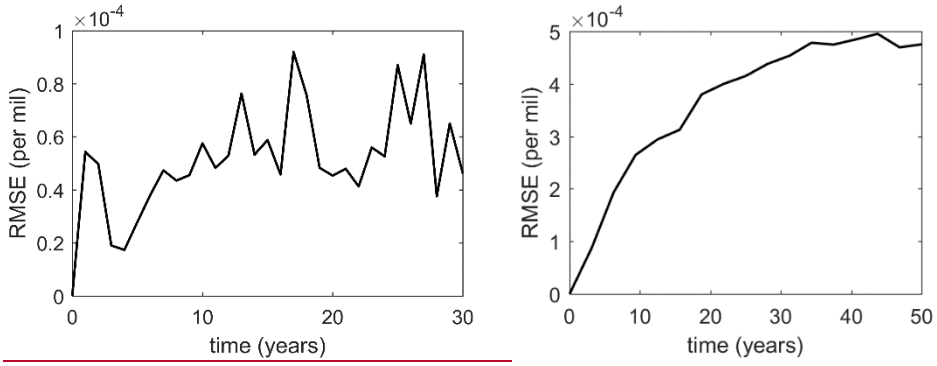

Figure S3. Evolution of the root-mean-square difference between the $\delta^{15}N$ profile produced by the model with barometric pumping and a time step of 3.5 days (default setting) relative to results obtained with 5x higher temporal resolution (assumed to yield the "true" solution). The error is quantified in the depth range of 68-75 m at WAIS Divide and converges at less than 0.~~5~~ 1 per meg after ~~30~~ 15 years. The pressure forcing was linearly interpolated for the high-resolution run and the model was initialized with the steady-state solution presented in the main text for both time steps. Interannual variability in the plot is caused by different surface pressures conditions right before each data point was recorded which forced transport of more or less gravitationally fractionated air into the region of interest.

1.2 Layering

We solve the trace gas transport equation under the consideration of discontinuous, impermeable, horizontal layers. Owing to computational limitations, layers ~~cannot be resolved directly in the model and~~ are ~~thus~~ somewhat idealized by assigning them an infinitesimal thickness. ~~The discretization of Eq. (S1) using a staggered grid as in Eqs. (S3) and (S4) greatly simplifies the implementation of these impermeable layers.~~

Layers are advected with the firn. The z-axis position of layer l, at time t, is found by numerically integrating the equation

$$z_l(t) = z_l(t_0) + \int_{t_0}^{t} w_{firn}(z_l(t'))\,\mathrm{d}t' , \tag{S6}$$

from the initial time t_0 where z_l is the depth of the layer and w_{firn} is the vertical firn advection velocity. Equation (S6) is discretized using Forward Euler time stepping such that

$$z_l(t) = z_l(t - \Delta t) + \mathrm{w_{firn}}\big(\mathrm{z_l}(\mathrm{z} - \Delta \mathrm{t})\big)\Delta \mathrm{t} . \tag{S7}$$

Layer positions on the discrete grid are updated once a layer has moved below the depth of the next grid box. New layers are introduced at 70% of the total depth of the firn column ~~(i.e. $z(\tilde{s} > 0)$)~~ once the top layer was displaced by at least the thickness of one annual layer from its initial position. The centre of each layer opening alternates between two locations (separated by half the horizontal domain length) and the layer size increases linearly with depth. Layers begin to cover the entire horizontal range of the model when the COD is reached and are not tracked further below this depth because any further gas transport is limited to advection with the pores.

1.3 Boundary conditions

A set of boundary and initial conditions accompany Eq. (S1):

1) The model is initialized with isotopic ratios as expected from gravitational equilibrium at all depths. For CO_2 and CH_4 transport simulations, initial concentrations are set to the lowest atmospheric concentrations observed for the time window of the simulation.

2) Surface values of q are given by the atmospheric trace gas concentration at each time step (i.e., a Dirichlet boundary). Atmospheric isotope ratios are assumed to be constant. Atmospheric CO_2 and CH_4 histories are taken and updated from Buizert et al. (2012) based on a combination of direct measurements and reconstructions from the Law Dome ice core site (~~Figure S4~~Figure S4) (Etheridge et al., 1996, 1998; Keeling et al., 2001; Dlugokencky et al., 2016a, 2016b).

3) A periodic boundary condition is implemented for all horizontal fluxes ~~by connecting both sides of the domain~~.

4) Because Eq. (S1) only describes the trace gas evolution in open pore space, the bottom of the domain is reached where $\tilde{s}$ equals zero. A Neumann boundary condition is chosen for this boundary and the flux leaving through the bottom of the domain is equal to the advection of pores with the firn. Diffusion already ceases to occur at the considerably shallower close-off depth (COD). Because the advective flux at the bottom boundary depends on q, it must be approximated locally using a backward difference scheme.

5) Layers are implemented on the staggered grid by setting the diffusivity and permeability between two adjacent boxes to zero. Layers have an infinitesimally small thickness and do not change the porosity anywhere. The permeability increases from layer edges towards the centre of the layer openings ~~as if porosity in the layer opening increased linearly~~ to obtain a more realistic flow field near layer edges. Other firn properties, such as the diffusivity, are ~~only~~ changed only on layer~~s~~ grid points because their porosity-dependence should be considerably weaker than for permeability. Vertical gas advection velocities on layers correspond to the local velocity of firn such that mixing ratio discontinuities are preserved and correctly advected downward at the same speed as layers. Layers do not directly impact the horizontal diffusion, permeability or porosity.

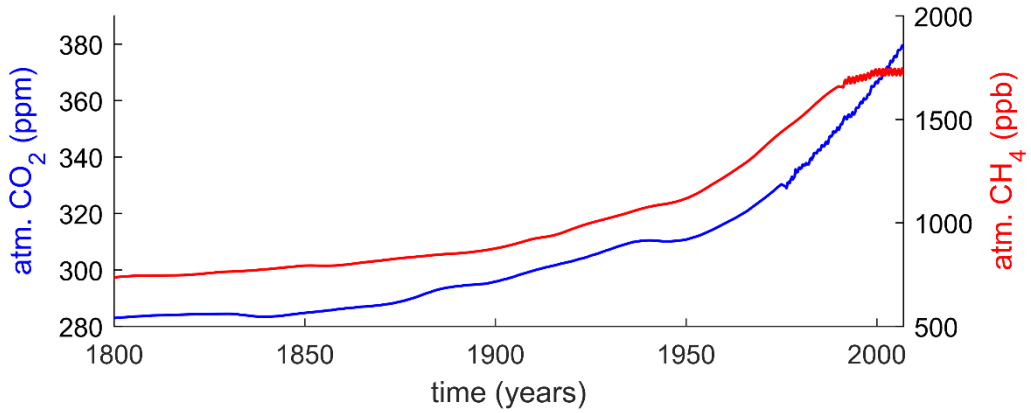

Figure S4. Atmospheric CO_2 and CH_4 histories composed from a combination of direct measurements and reconstructions from the Law Dome ice core site (Etheridge et al., 1996, 1998; Keeling et al., 2001; Buizert et al., 2012; Dlugokencky et al., 2016a, 2016b).

2 Flow field models for firn advection and barometric pumping

2.1 Firn pore advection and pore compression

Advection in the Eule~~a~~rian frame of the model ~~has three components~~consist of 3 distinct processes that combine to form the vector $\vec{u}$ in Eq. (S1). The first component of advection represents the downward migration of firn and air contained in the pore spaces due to the continuous accumulation of fresh snow at the surface. This flux can easily be calculated from the snow/ice mass balance and the density profile of the firn. Secondly, the compression of pores in the firn squeezes air out and drives a macroscopic airflow from the firn back to the atmosphere. Finally, barometric pumping drives direction-reversing airflows in response to surface pressure anomalies. These airflows act to return firn air pressures to hydrostatic balance. Barometric pumping flows are orders of magnitude faster than the other fluxes (Fig. ~~4c~~3c) but cause no net airflow when averaged over seasonal or longer time scales. Nevertheless, the fast flow speeds associated with barometric pumping may produce notable dispersive mixing in the deep firn as discussed in the main text (Buizert and Severinghaus, 2016).

The return and barometric pumping flows $\vec{u}_r$ and $\vec{u}_b$ move through the porous firn medium and obey Darcy's law. Darcy's law (Darcy, 1856) states that the equilibrium-state volume transport $\vec{Q}$ through the cross-sectional area A for laminar, incompressible flow is given by

$$\vec{Q} = -A\frac{\kappa}{\mu}\nabla P\,, \tag{S8}$$

where κ is permeability of the medium (m^2), μ is dynamic viscosity of the fluid (Pa·s), and ∇P is the pressure gradient (Pa m^{-1}) driving the flow. We note that the hydrostatic component of pressure ($\tilde{P}$) is no cause of flow and can thus be removed in the flow field model. We therefore consider only deviatoric pressure $P' \equiv P - \tilde{P}$. Discharge $\vec{Q}$ must be divided by area A and the pressure-corrected open porosity $\tilde{s}$ to obtain the true flow speed $\vec{u}$ per pore-cross sectional area used in the tracer advection equation because only a fraction of the total area is available for flow. This results in

$$\vec{u} = \frac{\vec{Q}}{A\,\tilde{s}} = -\frac{\kappa}{\mu\,\tilde{s}}\nabla \tilde{P}P'. \tag{S9}$$

The continuity equation for a compressible fluid in a porous medium can be derived from the conservation equation of air molecules, using the ideal gas law, which yields

$$\frac{\partial(s_{op}\,\rho)}{\partial t} + \nabla\cdot(s_{op}\,\rho\,\vec{u}) = s_{op}\,S\,, \tag{S10}$$

where ρ is air density and S denotes a source or sink of mass (Buizert and Severinghaus, 2016). Assuming porosity is independent of time, $\frac{\partial(s_{op})}{\partial t} = 0$, and the density in the firn is obtained from hydrostatic balance of an isothermal atmosphere, $\rho \simeq \rho_0 \exp\left(\frac{g\,M}{R\,T}\,z\right)$, the continuity equation implies that

$$\nabla \cdot (\tilde{s}\,\vec{u}) = \frac{\tilde{s}\,S}{\rho_0} - \frac{\partial(\rho_0)}{\partial t} \equiv \alpha\,, \tag{S11}$$

where ρ_0 is surface air density, α is a volume source or sink of air. The depth dependency of density has been absorbed into the open porosity as before. Equation (S11) shows that the divergence of the porosity-scaled velocity must equal the local source of air and change in density.

For the return flow of air to the atmosphere (i.e., $\vec{u}_r$) the source term α_r is the compression of pores during firn advection and density changes are neglected

$$\alpha_r = \nabla \cdot (\tilde{s}\,\vec{u}_r) = \nabla \cdot \left[-\frac{\kappa}{\mu}\nabla\tilde{P}P'\right], \tag{S12}$$

and for the barometric pumping component of flow (i.e., $\vec{u}_b$) the source or sink α_b is the local density change in response to surface pressure anomalies

$$\alpha_b = \nabla \cdot (\tilde{s}\,\vec{u}_b) = \nabla \cdot \left[-\frac{\kappa}{\mu}\nabla\tilde{P}P'\right]. \tag{S13}$$

α_r can be calculated as the vertical derivative of the mean vertical flow due to pore compression $\langle w_r \rangle = w_{air} - w_{firn}$, where w_{air} is the mean effective vertical air transport velocity (m s^{-1}), such that

$$\alpha_r = \frac{\partial}{\partial z}\left[\tilde{s}\,(w_{air} - w_{firn})\right]. \tag{S14}$$

This is analogous to calculating pore compression in a 1D firn column (Rommelaere et al., 1997). At steady-state, mass conservation of air requires that the net vertical flux of air molecules is equal at all depths when integrated horizontally. Using the ideal gas law, the total vertical transport of air molecules n per area A is given by

$$\frac{n}{A\,t} = \frac{P\frac{V}{t}}{A\,R\,T} = \frac{1}{R\,T}\left(\tilde{P}s_{op}w_{air} + P_b s_{cl} w_{firn}\right) \equiv \text{const.}, \tag{S15}$$

where $\tilde{P}$ is the ambient hydrostatic pressure in open pores, P_b is pressure of air in bubbles, and s_{cl} is closed porosity (m^3 m^{-3}) (Rommelaere et al., 1997). Temporal changes in $\tilde{P}$ are small and their impact on w_{air} and P_b is neglected in Eq. (S15). At $z =$

$z(\mathrm{COD})$, vertical airflow ceases and air is only carried further downward by the advection of pores with the firn. Therefore, w_{air} is equal to the advection velocity at and below this depth and

$$\frac{n}{A\,t} = \frac{1}{R\,T}\left(\tilde{P} s_{op} w_{firn} + P_b s_{cl} w_{firn}\right)_{|z=z_{COD}} . \tag{S16}$$

For given bubble pressure P_b, Eqs. (S15) and (S16) can be solved to find w_{air} and α_r at all depths. Rommelaere et al. (1997) derive an equation for the change in bubble air content based on the compression of previously existing bubbles and the trapping of air in new bubbles

$$P_b(z) = \frac{1}{w_{firn}\, s_{cl}} \int_0^z \tilde{P}\, w_{firn} s_t \frac{\partial}{\partial z}\left(\frac{s_{cl}}{s_t}\right) dz\,, \tag{S17}$$

where $s_t \equiv s_{cl} + s_{op}$ is total porosity. Typical pressure profiles are shown in Fig. S5. High P_b near the surface results from the very small, but non-zero closed porosity values that are an artefact of the porosity parameterization at that depth. Mean P_b in the top ~60 % of the firn column above the COD should thus be interpreted with caution.

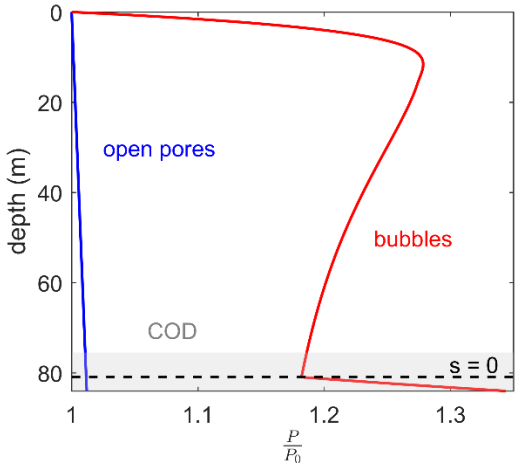

Figure S5. Normalized profiles of pressure in bubbles and of hydrostatic pressure in open pores at WAIS Divide.

Equations (S12), (S14), (S15), and (S17) are combined to calculate the ~~hypothetical~~ pressure fields for the return flow

$$\frac{\partial}{\partial z}\left[\tilde{s}\left(w_{air} - w_{firn}\right)\right] = \nabla \cdot \left[-\frac{\kappa}{\mu}\nabla \tilde{P} P'\right]. \tag{S18}$$

Subsequently, the corresponding velocity field $\vec{u}_r$ is obtained using Eq. (S9). Plots of a representative pressure anomaly field and corresponding flow field are shown in Figs. S6 and S7.

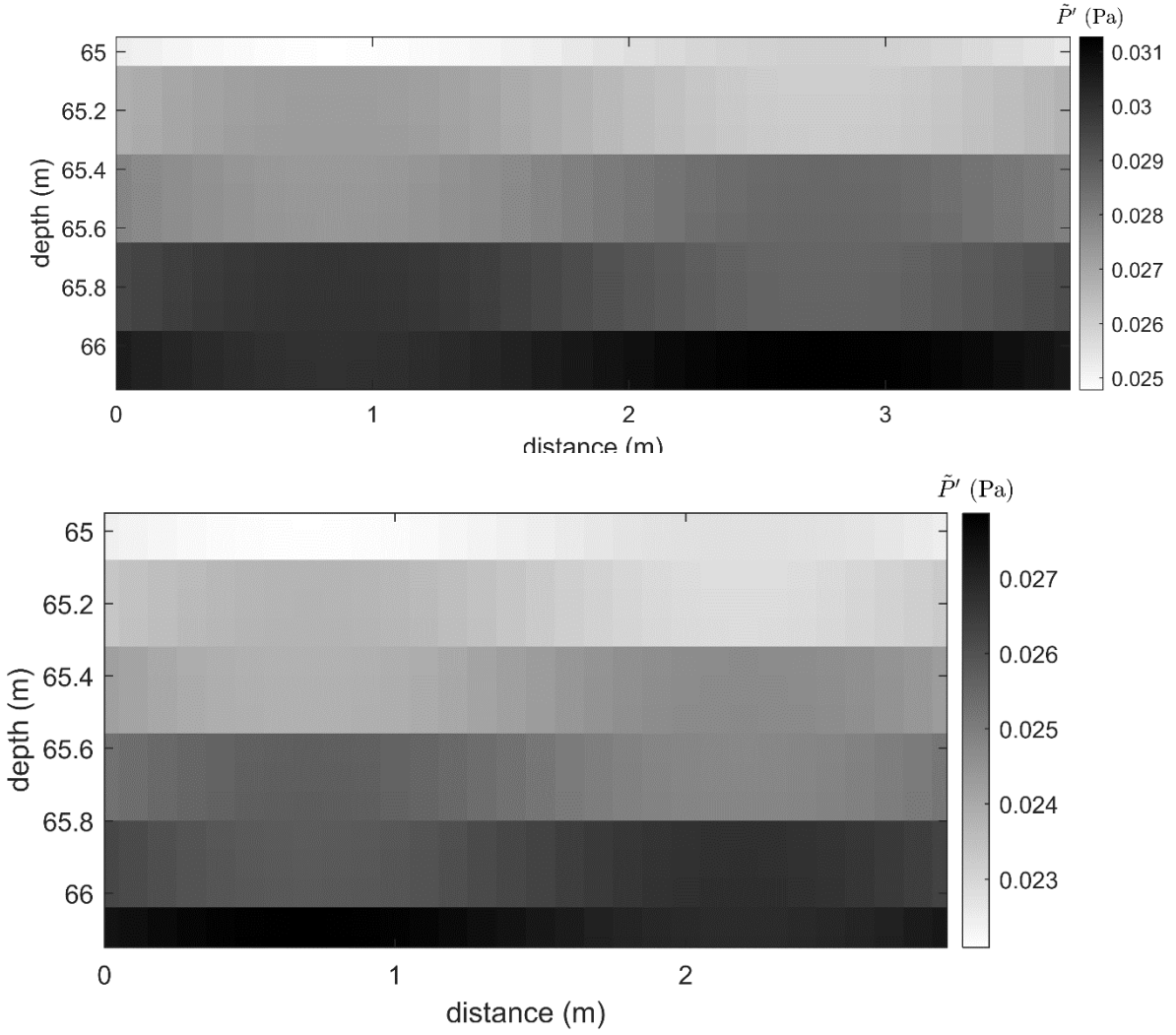

Figure S6. Pressure anomaly field calculated for the return flow to the atmosphere shown in Fig. S7. Layers appear as discontinuities in the pressure field on the model domain. The ~~P~~plot ~~is~~ shown~~s~~ a ~1 m section of the deep firn and is presented at reduced grid resolution for clarity.

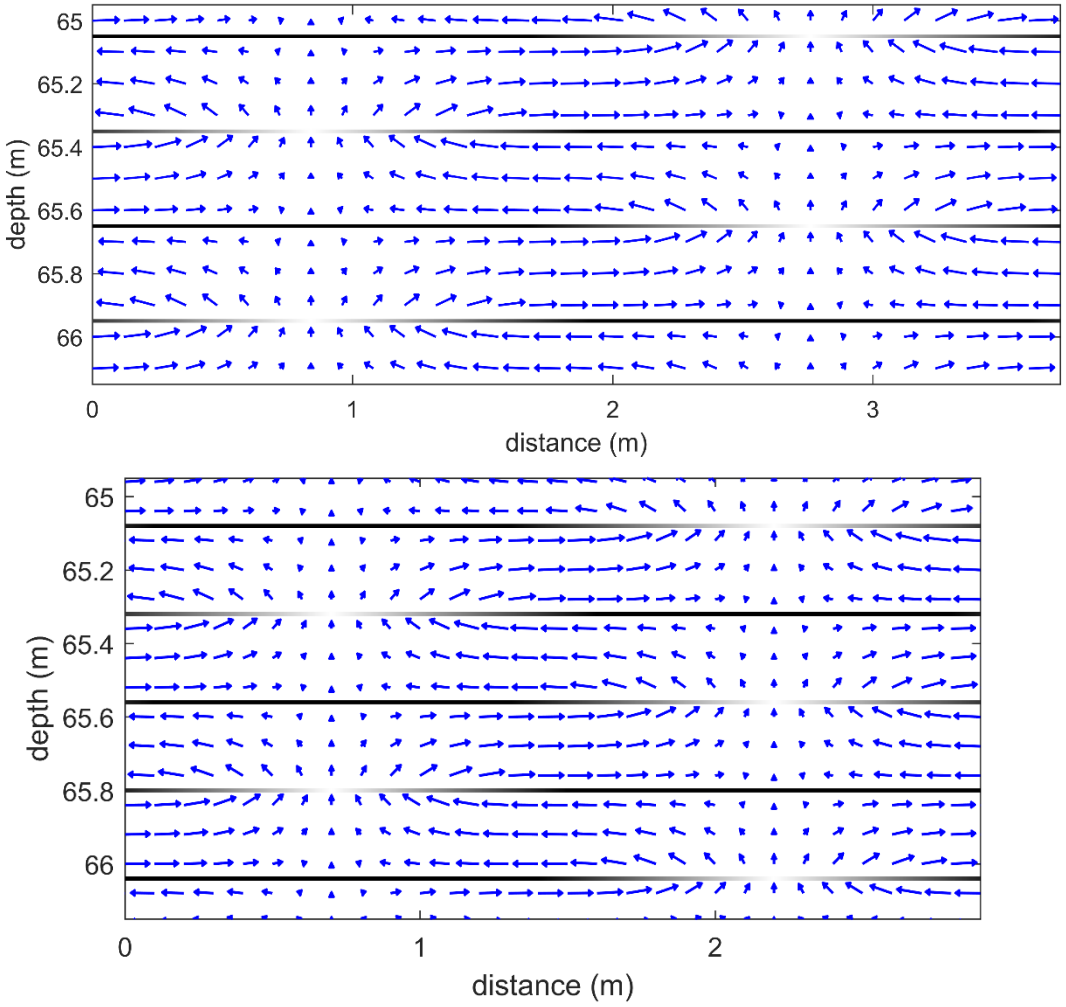

Figure S7. Return flow of air to the atmosphere corresponding to Fig. S6. The plot shows a selected region of the deep firn and is presented at reduced grid resolution for clarity. ~~Plot is shown at reduced grid resolution for clarity.~~ The blackness of layers indicates the local vertical permeability of the firn.

2.2 Barometric pumping

The source term for barometric pumping, α_b, is equal to the change in firn air density caused by surface pressure anomalies associated with passing storms (Fig. S8). Air compression or expansion demands a local convergence or divergence of flow that forces air to move in or out of the firn, assuming porosity remains constant.

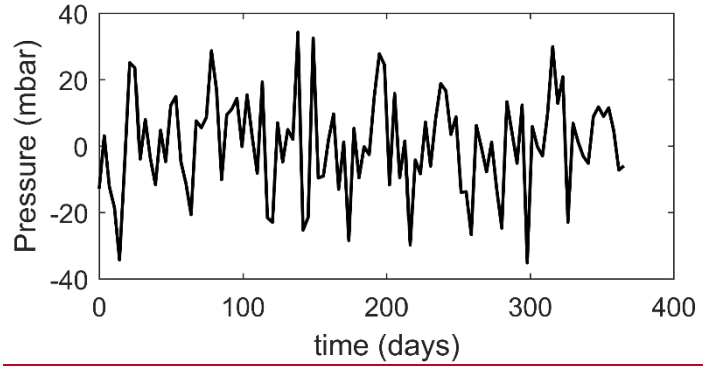

Figure S8. One-year subsection of the surface pressure forcing driving barometric pumping at WAIS Divide. Observed daily pressure variability of ~7 mbar was rescaled by a factor of $\sqrt{\Delta t}$ to account for the longer time step used in the model.

Starting from Darcy's law, the continuity equation and hydrostatic balance, Buizert and Severinghaus (2016) derived a partial differential equation for firn air pressure similar to Eq. (S19)

$$s_{op}\frac{\partial P}{\partial t} = \nabla \cdot \left[s_{op}\, \bar{P}_0 \exp\left(\frac{M\, g}{R\, T} z\right) \frac{\kappa}{\tilde{s}\mu} \nabla \tilde{P} P' \right]. \quad \text{(S19)}$$

Here, we ~~chose not to expand the divergence operator,~~ remove the hydrostatic component of pressure through the definition of $\tilde{P}P'$ and use the version of Darcy's law given by Eq. (S9) ~~instead~~. Note that ~~F~~following Buizert and Severinghaus (2016), we linearized Eq. (S19) in the pressure anomaly by replacing the pressure (or equivalently the density) in the continuity equation by the annual mean hydrostatic pressure $\left(P = \bar{P}_0 \exp\left(\frac{M\, g}{R\, T} z\right)\right)$. However, the high computational costs of running a 2D model (~2 days runtime on 10 CPUs per simulation with Δt = 3.5 days) prevent us from reducing the time step below ~3 days and from explicitly resolving the propagation of surface pressure waves into firn. Instead, we assume that the pressure changes on the LHS ~~should be~~are approximately in hydrostatic balance throughout the firn, in line with results by Buizert and Severinghaus (2016):

$$\frac{\partial P}{\partial t} \simeq \frac{\partial \tilde{P}}{\partial t} = \frac{\partial P_0}{\partial t} \exp\left(\frac{M\, g}{R\, T} z\right), \quad \text{(S20)}$$

where $P_0 = P_0(t)$ is the time-varying surface pressure. Combining Eqs. (S19) and (S20) yields α_b

$$\alpha_b \equiv \frac{\tilde{s}}{\bar{P}_0} \frac{\partial P_0}{\partial t}, \quad \text{(S21)}$$

and an equation to calculate a hypothetical pressure field which gives rise to the barometric pumping flow

$$\frac{\tilde{s}}{\bar{P}_0} \frac{\partial P_0}{\partial t} = \nabla \cdot \left[\frac{\kappa}{\mu} \nabla \tilde{P} P' \right], \quad \text{(S22)}$$

where $\bar{P}_0$ is the annual mean surface pressure. The flow field, ~~found using~~given by Eq. (S9), may be interpreted as the flow required over timestep Δt to return the column to hydrostatic balance with a new surface pressure of P_0. To represent storm activity, we prescribe $P_0(t)$ as pseudo-red noise. The surface pressure variability in the model is slightly damped compared to observations in order to account for non-hydrostatic changes. This yields comparable mean vertical velocities as published by Buizert and Severinghaus (2016).

Similar to Eq. (S1), the flow field models for the return flow and barometric pumping are discretized using central differences on a staggered grid. Values for κ are calculated using the parametrization of Adolph and Albert (2014) and μ is assumed to be constant. Surface values of ~~$\tilde{P}P'$~~ are set to zero for the return flow and to $P_0(t) - \bar{P}_0$ for barometric pumping. The grid is periodic in the x-direction and no fluxes through the bottom boundary are permitted. Layers set the permeability κ, and thus also velocities, between grid boxes to zero. Because layers are advected with the firn, the total flow field must be recalculated at every time step.

3 Thermal model

We use the thermal model of Alley and Koci (1990) to obtain temperature fields for all time steps. The temperature evolution of firn and ice can be simulated in 1D because horizontal temperature gradients are negligibly small. Heat transport in firn is governed by a ~~slightly~~ modified version of the traditional heat equation (Cuffey and Paterson, 2010)

$$\rho c_p \frac{\partial T}{\partial t} = \gamma \frac{\partial^2 T}{\partial z^2} + \frac{\partial \gamma}{\partial z}\frac{\partial T}{\partial z} - \rho c_p w_s \frac{\partial T}{\partial z} + Q \,, \tag{S23}$$

where $T = T(t,z)$ is temperature (°C), $\rho = \rho(z)$ firn density (kg m^{-3}), $c_p = c_p(T)$ specific heat capacity of firn (J kg^{-1} °C^{-1}), $\gamma = \gamma(T,\rho)$ heat conductivity (W m^{-1} °C^{-1}), w_s vertical advection velocity of firn

/ice (m s^{-1}), and Q is local heat production due to firn compaction and ice deformation (J s^{-1} m^{-2}). ~~Using the chain rule,~~ ~~t~~This expression can be rewritten in terms of the thermal diffusivity $k = \frac{\gamma}{c_p \rho}$ ~~(m^2 s^{-1})~~ as (Johnsen, 1977) ~~as~~

$$\frac{\partial T}{\partial t} = k\frac{\partial^2 T}{\partial z^2} + \left[\left(\frac{k}{\rho} + \frac{\partial k}{\partial \rho}\right)\frac{\partial \rho}{\partial y} - w_s\right]\frac{\partial T}{\partial z} + \left[\frac{\partial k}{\partial T} + \frac{k}{c_p}\frac{dc_p}{dT}\right]\left(\frac{\partial T}{\partial z}\right)^2 + Q\,. \quad \text{(S24)}$$

Following Alley and Koci (1990) ~~and references therein~~, we use the following parametrizations for w_s, c_p and k:

$$w_s = w_{firn}\left(1 - \frac{\sigma}{\rho_{ice} H}\right), \quad \text{(S25)}$$

$$c_p = 2096 + 7.7752T\,, \quad \text{(S26)}$$

$$k = \left(1 - 0.00882(T + 30)\right)\left(-1.229 \times 10^{-14}\rho^3 + 2.1312 \times 10^{-11}\rho^2 - 9.4 \times 10^{-9}\rho + 1.779 \times 10^{-6}\right), \quad \text{(S27)}$$

where σ is the cumulative load of firn~~f~~ above (kg m^{-2}) and H the total thickness of the ice sheet. Q is parameterized as

$$Q = \sigma\frac{\dot{b}\,\rho_{ice}}{\rho^3}\frac{\partial \rho}{\partial z}\frac{g}{c_p} + \frac{2\left(\frac{\dot{b}}{H}\right)^{\frac{4}{3}}}{\rho\, c_p \left(4.26 \times 10^{-13} \exp\left(-\frac{7217}{T + 273.15}\right)\right)^{\frac{1}{3}}}, \quad \text{(S28)}$$

where $\dot{b}$ is the ice equivalent accumulation rate (m s^{-1}) (Alley and Koci, 1990). Equation (S24) is solved by explicit (forward Euler) time stepping because of the non-linearity in T. Spatial derivatives are approximated by central differences. Since the firn air transport model just requires firn temperature for the last ~200 years, only the top 130 m of the ice sheet are simulated in the temperature model for computational efficiency. The temperature gradient at the bottom boundary is fixed to zero but temperature at that depth can evolve freely. Surface temperature histories for WAIS Divide and Law Dome DSS were previously published by Orsi et al. (2012), Van Ommen et al. (1999) and Dahl-Jensen et al. (1999) and allow us to develop a surface forcing for the model. For the Law Dome site DSSW20K, we combine the water oxygen isotope record translated to temperature following Van Ommen et al. (1999) and supplement~~ed~~ this published, six centuries long record with the rescaled mean annual temperature recorded at the nearby Casey Station for the last ~50 years (Jones and Reid, 2001). Further information on the isotope ~~–~~ to ~~–~~ temperature scaling and the relationship to the historic data at Casey station can be found in Van Ommen et al. (1999). An ~~appropriate~~ offset is applied to the isotope and instrumental temperatures to match the slightly different mean annual temperature at DSSW20K compared to DSS. The Orsi et al. (2012) best fit WAIS Divide surface temperature record is modified slightly to bring our model results in line with the published borehole temperature profiles (Fig. S9). A ~~generic Antarctic~~ site-specific mean seasonal cycle is superimposed on both long-term temperature forcings. The

seasonal cycle is generated by matching a sine and cosine wave including several harmonics to a climatology of Automated Weather Station data at WAIS Divide and Law Dome (Lazzara et al., 2012). The exact details of the seasonal cycle are of limited importance for trace gas transport to the lock-in zone because the seasonal temperature wave becomes quickly attenuated in the firn. We do not mean to imply that our forcings are necessarily accurate reconstructions of local surface temperature but the forcings should yield approximately correct thermal gradients in the firn using our model's temperature module. Moreover, thermal fractionation of isotopes only amounts to a comparatively small influence on most isotopes ratios. Thus, an approximately correct temperature profile is sufficient for our purposes. Temperature fields are only used to account for isotope thermal fractionation and any temperature influence on firn densification is neglected.

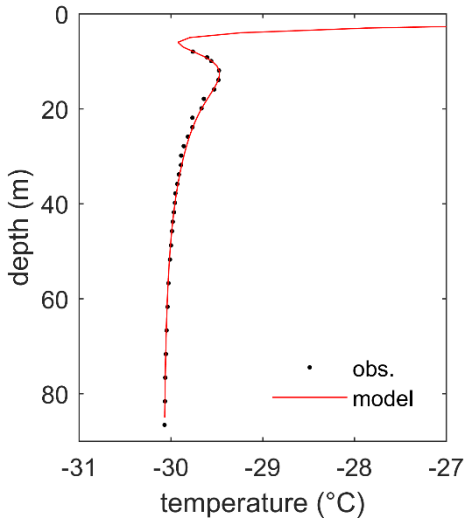

Figure S9. Observed borehole temperature and simulated temperature profile at WAIS Divide in January 2009 (Data from: Orsi et al., 2012).

4 ~~Model parameter summary~~Summary tables

Table S1. Overview of important model parameters

Parameters	WAIS Divide	Law Dome DSSW20K
Firn ~~Depth~~ depth (i.e., open	85 m	~~56~~5 m
Model height ~~Width~~	80.92 m ~~12 x thickness of an annual~~	52.74 m
Model width	2.85 m (= 12x annual layer thickness)	2.43 m
Horizontal grid spacing	0.03 m	0.03 m
Vertical grid spacing	0.04 m	0.04 m
Depth of occurrence of first layer	56.65 m (= 70 % of ~~total firn column~~firn	36.94 m
~~Time~~Simulation time range & time	1800–2006 in 3.5-day timesteps	1800–1998.05 in 3.5-day timesteps
Obs. annual mean ~~T~~temperature	243.15 K	253.45 K
Ice sheet ~~height~~ thickness H	3500 m	1200 m
Mean ~~S~~surface Pressure [1,2]	789 hPa	850 hPa
Surface ~~P~~pressure variability ($1\ \sigma$)	~~5~~7 hPa day^{-1}	11.2~~8~~ hPa day^{-1}
Ice equiv. advection velocity[1,2]	6.9714×10^{-9} m s^{-1}	5.1706×10^{-9} m s^{-1}
Surface mixed zone eddy diffusion[3] $D_e = D_{e0}\exp\left(-\frac{z}{\tau}\right)$	$D_{e0} = 2.38 \times D_{m0}$ $\tau = 2.5$ m range: 0 – 8 m + 2 m linear taper	$D_{e0} = 2.4 \times D_{m0}$ $\tau = 3.5$ m range: 0 – 14 m + 2 m linear taper

[1] WAIS Divide: WAIS Divide Project Members (2016)
[2] Law Dome: Etheridge et al. (1992)

[3] Eq. Kawamura et al. (2013)~~[3] and MacFarling Meure et al. (2006)~~
~~[4] Dlugokencky et al. (2016a) and Dlugokencky et al. (2016b)~~
~~[5] Keeling et al. (2001) and Dlugokencky et al. (2016b)~~
~~[6] Eq: Schwander et al. (1997)~~
~~[7] original Eq: Buizert and Severinghaus (2016)~~
~~[8] Eq: Goujon et al. (2003) in Severinghaus et al. (2010) and Kawamura et al. (2013)~~
~~[9] data: Trudinger et al. (1997); WAIS Divide coefficients: Battle et al. (2011)~~

Table S2. Overview of selected parameterizations in the model

Density of ice[1]		$\rho_{ice} = 916.5 - 0.14438\,(T - 273.15) - 1.517\cdot10^{-4}(T - 273.15)^2$ kg
Free air diffusivities relative to CO_2		Table 4 & 5 in SI to Buizert et al. (2012) and references therein
Dispersivity[2] (assumed isotropic)		$\alpha(s_{op}) = 1.26\cdot\exp(-25.7 s_{op})$
Total porosity		$s_t = 1 - \frac{\rho_{firn}}{\rho_{ice}}$
Closed porosity[3]		$s_{cl} = 0.37\cdot s_t\left(\frac{s_t}{1-\frac{831.2}{\rho_{ice}}}\right)^{-7.6}$
Firn density fit	$\leq z_{crit1}$	$\rho_{firn} = a_0 + a_1 z + a_2\cdot\exp[a_3\cdot(z_{crit1} - z)]$ kg m^{-3}
	$z_{crit1} - z_{crit2}$	$\rho_{firn} = b_0 + b_1 z + b_2 z^2$ kg m^{-3}
	$\geq z_{crit2}$	$\rho_{firn} = \rho_{ice} - (\rho_{ice} - \rho(z_{crit2}))\cdot\exp\left[-\frac{z - z_{crit2}}{\rho_{ice} - \rho(z_{crit2})}(b_1 + 2\cdot b_2 z_{crit2})\right]$ kg m^{-3}
Density fit parameters[4]	WAIS Divide	Law Dome DSSW20K
	$z_{crit1} = 16$	$z_{crit1} = 19.7186$
	$z_{crit2} = 110$	$z_{crit2} = 37.4193$

	$a_0 = 420$ $a_1 = 20.0121$ $a_2 = -151.242$ $a_3 = -0.1$ $b_0 = 506.85$ $b_1 = 5.3748$ $b_2 = -0.0152$	$a_0 = 511.8111$ $a_1 = 7.8210$ $a_2 = -0.0476$ $a_3 = 0.4143$ $b_0 = 556.5176$ $b_1 = 5.3204$ $b_2 = 0.0117$

[1] Eq: Schwander et al. (1997)
[2] original Eq: Buizert and Severinghaus (2016)
[3] Eq: Goujon et al. (2003) in Severinghaus et al. (2010) and Kawamura et al. (2013)
[4] data: Trudinger et al. (1997); WAIS Divide coefficients: Battle et al. (2011)

5 Law Dome DSSW20K firn properties

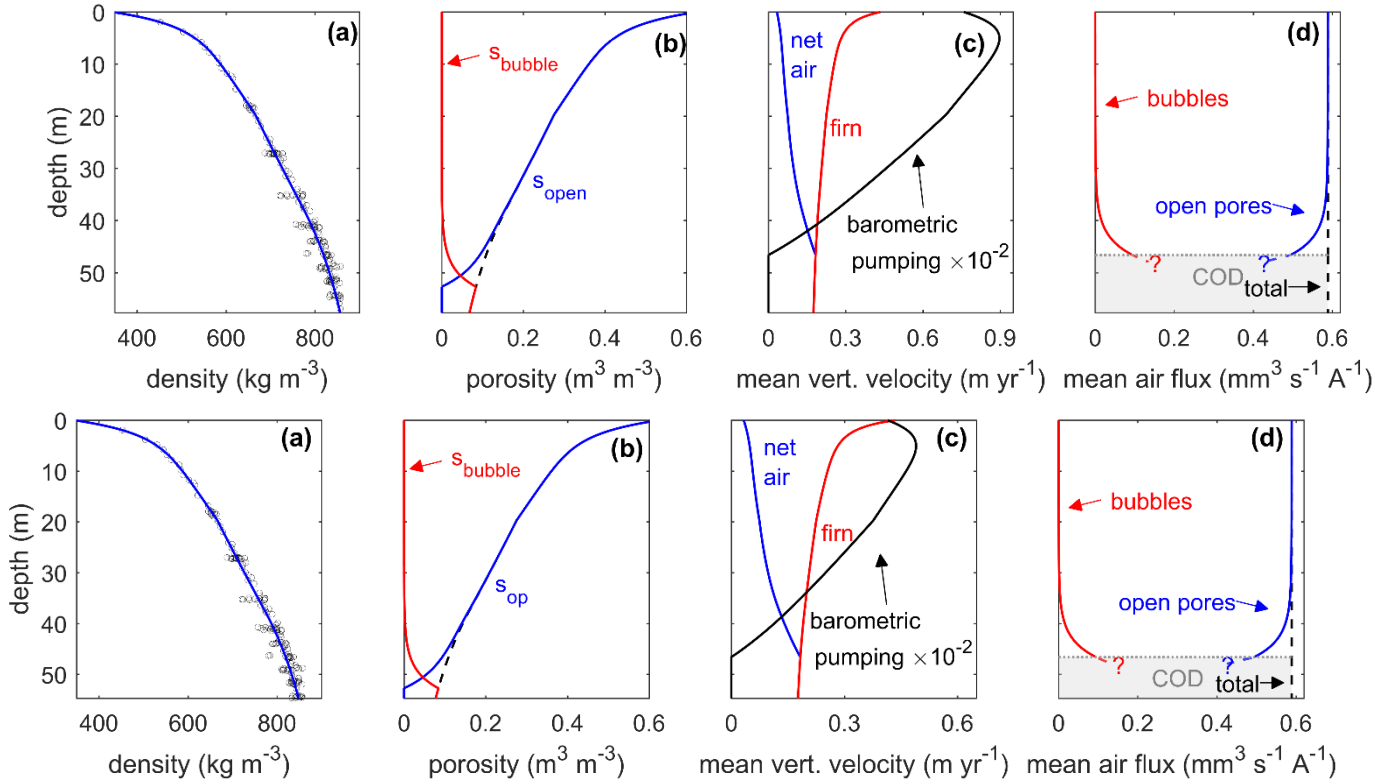

Figure S10. Same as Fig. ~~4~~ 3 for Law Dome DSSW20K. Density data: Trudinger et al. (2002, 2013)

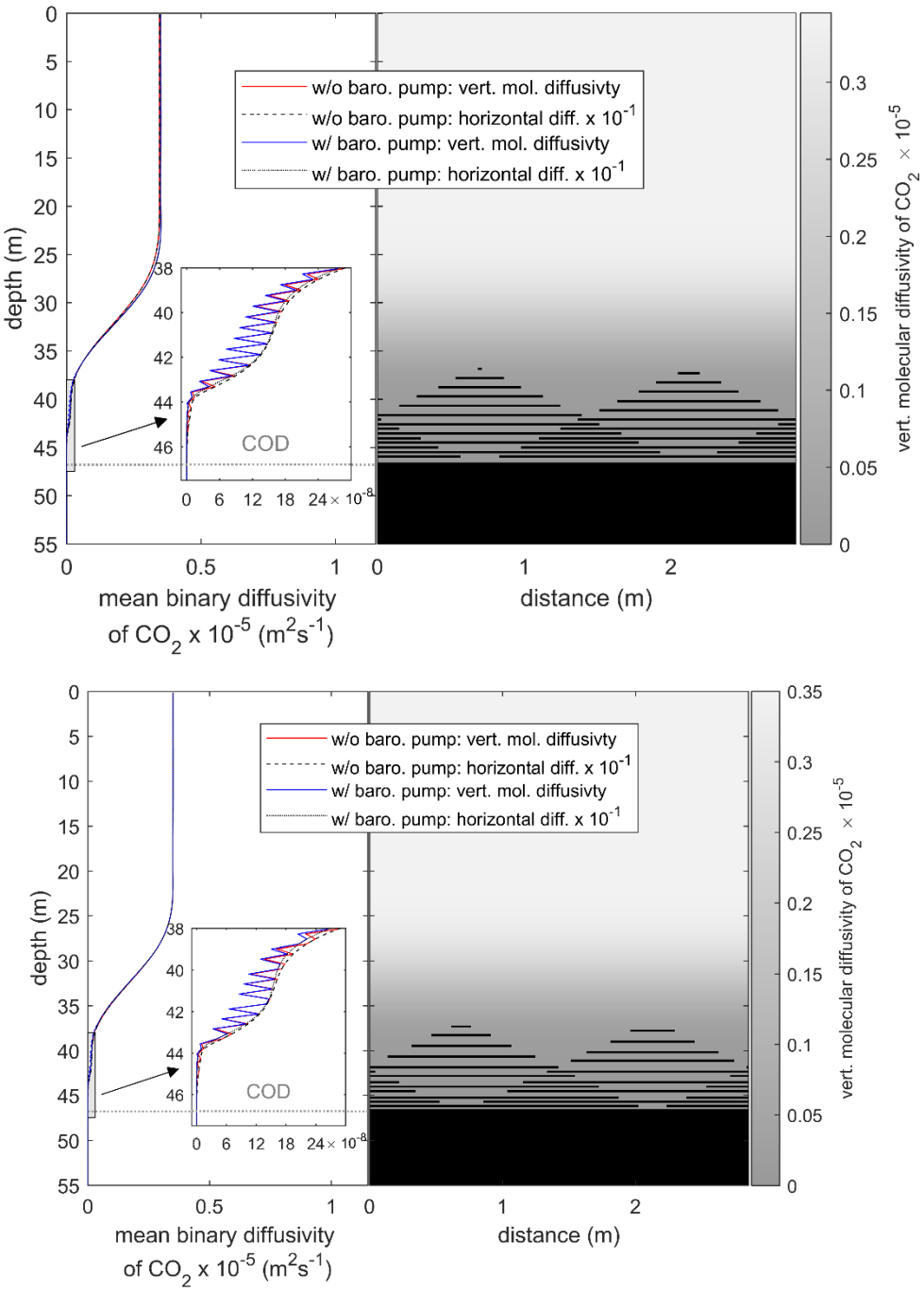

Figure S11. Same as Fig. ~~6~~ 5 for Law Dome DSSW20K. Every third annual layer is shown.

6 Mass normalization

Isotope ratios in delta notation are mass-normalized ~~when mentioned~~ to an isotope mass difference of one atomic mass unit (amu) using q-values

$$q_{norm} = q^{\frac{1}{1000 \times \Delta m}}. \quad \text{(S29)}$$

This is more accurate than dividing the ratio in delta notation by the isotope mass difference in amu (e.g. divide $\delta^{40}Ar/^{36}Ar$ by ~4 amu).

7 ~~WAIS Divide CO_2 profile comparison~~Additional supporting Figures

~~Four different versions of the 2D model are presented for WAIS Divide in the text. They represent combinations of active and inactive barometric pumping and the presence or absence of layers in the model. 2D models without layers contain no horizontal inhomogeneities and are thus reduced to 1D for computational efficiency but contain essentially the same physics and numerical implementation. Diffusivities in both 1D models are automatically tuned such that the CO_2 profiles are (nearly) identical to the corresponding 2D versions. The use of an automatic tuning procedure to match the CO_2 and CH_4 profiles of any 2D version of the model is prohibited by the high computational costs of running a 2D model. Differences in the CO_2 profiles between the different models are shown in Fig. S10.~~

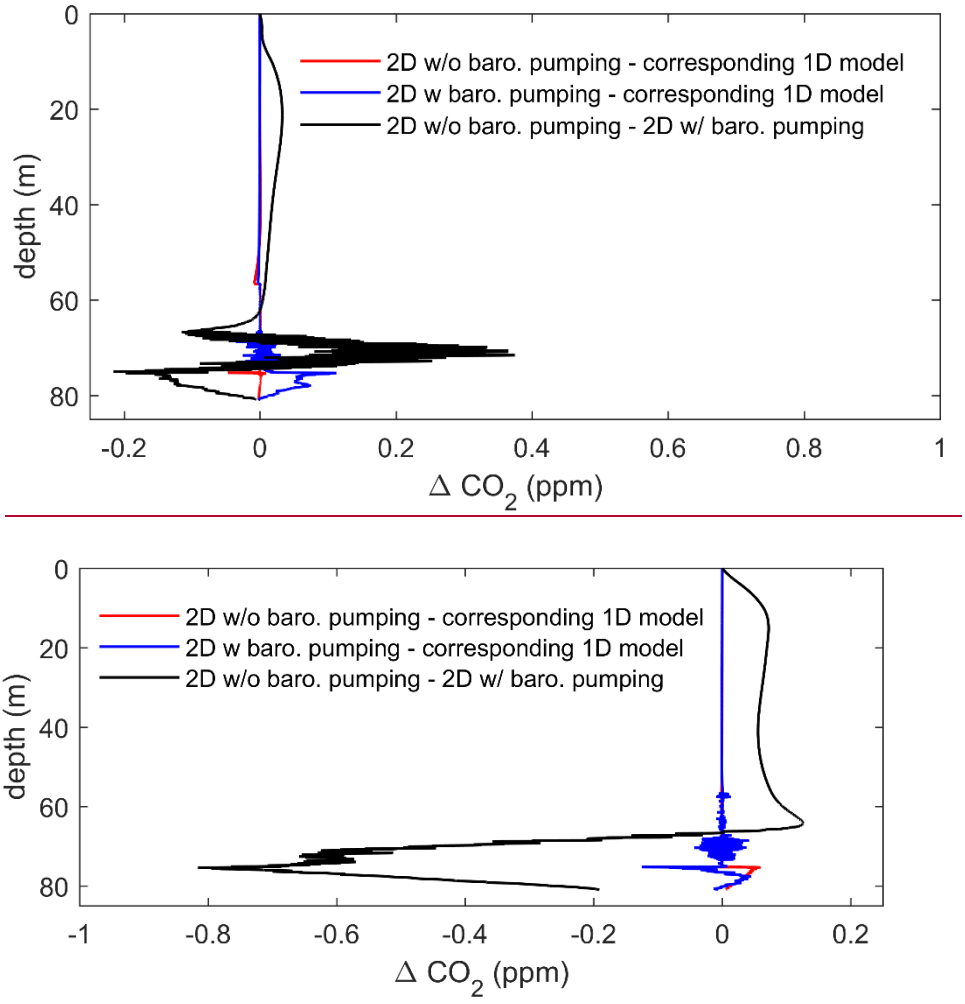

Figure S12. Comparison of simulated CO_2 values at WAIS Divide between both 2D models (black line) and between each 2D model and the corresponding 1D model (red and blue line).

~~8 Predicting kinetic isotope fractionation at WAIS Divide~~

~~Kinetic isotope fractionation (ϵ') of the krypton nitrogen ratio can be directly related to ϵ' of krypton isotopes. A linear fit yields the relationship shown in Fig. S11 and discussed in the text.~~

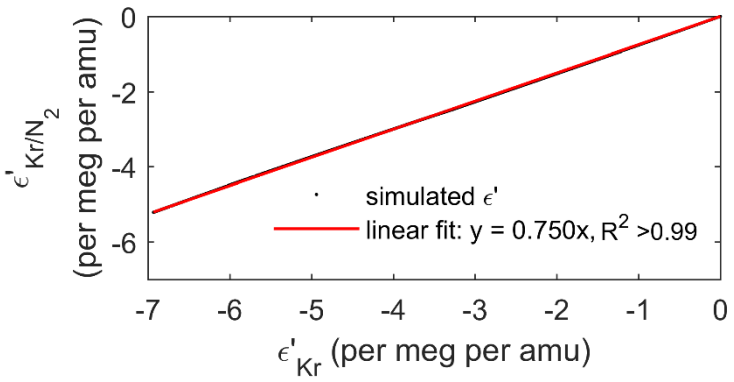

Figure S13. Linear fit to the relationship between mass-normalized ϵ' of $^{84}Kr/^{28}N_2$ and ϵ' of $^{86}Kr/^{82}Kr$ observed in the 2D model with barometric pumping at WAIS Divide.

References

Adolph, A. C. and Albert, M. R.: Gas diffusivity and permeability through the firn column at Summit, Greenland: Measurements and comparison to microstructural properties, Cryosphere, 8(1), 319–328, doi:10.5194/tc-8-319-2014, 2014.

Alley, R. B. and Koci, B. R.: Recent warming in central Greenland?, Annals of Glaciology, 14, 6–8, 1990.

Battle, M. O., Severinghaus, J. P., Sofen, E. D., Plotkin, D., Orsi, A. J., Aydin, M., Montzka, S. A., Sowers, T. and Tans, P. P.: Controls on the movement and composition of firn air at the West Antarctic Ice Sheet Divide, Atmospheric Chemistry and Physics, 11, 11007–11021, doi:10.5194/acp-11-11007-2011, 2011.

Buizert, C. and Severinghaus, J. P.: Dispersion in deep polar firn driven by synoptic-scale surface pressure variability, The Cryosphere, 10, 2099–2111, doi:10.5194/tc-2016-148, 2016.

Buizert, C., Martinerie, P., Petrenko, V. V, Severinghaus, J. P., Trudinger, C. M., Witrant, E., Rosen, J. L., Orsi, A. J., Rubino, M., Etheridge, D. M., Steele, L. P., Hogan, C., Laube, J. C., Sturges, W. T., Levchenko, V. A., Smith, A. M., Levin, I., Conway, T. J., Dlugokencky, E. J., Lang, P. M., Kawamura, K., Jenk, T. M., White, J. W. C., Sowers, T., Schwander, J. and Blunier, T.: Gas transport in firn: Multiple-tracer characterisation and model intercomparison for NEEM, Northern Greenland, Atmospheric Chemistry and Physics, 12, 4259–4277, doi:10.5194/acp-12-4259-2012, 2012.

Cuffey, K. M. and Paterson, W. S. B.: The Physics of Glaciers, 4th ed., Butterworth-Heinemann/Elsevier, Burlington, MA., 2010.

Dahl-Jensen, D., Morgan, V. I. and Elcheikh, A.: Monte Carlo inverse modelling of the Law Dome (Antarctica) temperature profile, Annals of Glaciology, 29, 145–150, doi:10.3189/172756499781821102, 1999.

Darcy, H.: Les Fontaines Publiques de la Ville de Dijon, Victor Dalmont, Paris., 1856.

Dlugokencky, E. J., Lang, P. M., Mund, J. W., Crotwell, A. M., Crotwell, M. J. and Thoning, K. W.: Atmospheric Carbon Dioxide Dry Air Mole Fractions from the NOAA ESRL Carbon Cycle Cooperative Global Air Sampling Network, 1968-2015, Version: 2016-08-30, 2016a.

Dlugokencky, E. J., Lang, P. M., Crotwell, A. M., Mund, J. W., Crotwell, M. J. and Thoning, K. W.: Atmospheric Methane Dry Air Mole Fractions from the NOAA ESRL Carbon Cycle Cooperative Global Air Sampling Network, 1983-2015, Version: 2016-07-07, 2016b.

Etheridge, D. M., Pearman, G. I. and Fraser, P. J.: Changes in tropospheric methane between 1841 and 1978 from a high accumulation-rate Antarctic ice core, Tellus, 44B, 282–294, doi:10.1034/j.1600-0889.1992.t01-3-00006.x, 1992.

Etheridge, D. M., Steele, L. P., Langenfelds, R. L., Francey, R. J., Barnola, J. M. and Morgan, V. I.: Natural and anthropogenic changes in atmospheric CO2 over the last 1000 years from air in Antarctic ice and firn, Journal of Geophysical Research-Atmospheres, 101(D2), 4115–4128, doi:10.1029/95JD03410, 1996.

Etheridge, D. M., Steele, L. P., Francey, R. J. and Langenfelds, R. L.: Atmospheric methane between 1000 A.D. and present: Evidence of anthropogenic emissions and climatic variability, Journal of Geophysical Research, 103(D13), 15979, doi:10.1029/98JD00923, 1998.

Goujon, C., Barnola, J.-M. and Ritz, C.: Modeling the densification of polar firn including heat diffusion: Application to close-off characteristics and gas isotopic fractionation for Antarctica and Greenland sites, Journal of Geophysical Research, 108, 4792, doi:10.1029/2002JD003319, 2003.

Johnsen, S. J.: Stable isotope profiles compared with temperature profiles in firn with historical temperature records, Isotopes and Impurities in Snow and Ice, 388–392, 1977.

Jones, P. D. and Reid, P. A.: A databank of Antarctic surface temperature and pressure data, ORNL/CDIAC-27, NDP-032, Carbon Dioxide Information Analysis Center, Oak Ridge National Laboratory, U.S. Department of Energy, Oak Ridge, Tennessee., 2001.

Kawamura, K., Severinghaus, J. P., Albert, M. R., Courville, Z. R., Fahnestock, M. A., Scambos, T. A., Shields, E. and Shuman, C. A.: Kinetic fractionation of gases by deep air convection in polar firn, Atmospheric Chemistry and Physics, 13, 11141–11155, doi:10.5194/acp-13-11141-2013, 2013.

Keeling, C. D., Stephen, C., Piper, S. C., Bacastow, R. B., Wahlen, M., Whorf, T. P., Heimann, M. and Meijer, H. A.: Exchanges of atmospheric CO2 and 13CO2 with the terrestrial biosphere and oceans from 1978 to 2000., Global Aspects, SIO Reference Series. Scripps Institution of Oceangraphy, San Diego, 01–06, 83–113, doi:10.1007/b138533, 2001.

Lazzara, M. A., Weidner, G. A., Keller, L. M., Thom, J. E. and Cassano, J. J.: Antarctic automatic weather station program: 30 years of polar observations, Bulletin of the American Meteorological Society, 93, 1519–1537, doi:10.1175/BAMS-D-11-00015.1, 2012.

Van Ommen, T. D., Morgan, V. I., Jacka, T. H., Woon, S. and Elcheikh, A.: Near-surface temperatures in the Dome Summit South (Law Dome, East Antarctica) borehole, Annals of Glaciology, 29, 141–144, doi:doi:10.3189/172756499781821382, 1999.

Orsi, A. J., Cornuelle, B. D. and Severinghaus, J. P.: Little Ice Age cold interval in West Antarctica: Evidence from borehole temperature at the West Antarctic Ice Sheet (WAIS) Divide, Geophysical Research Letters, 39(L09710), 1–7, doi:10.1029/2012GL051260, 2012.

Rommelaere, V., Arnaud, L. and Barnola, J.-M.: Reconstructing recent atmospheric trace gas concentrations from polar firn and bubbly ice data by inverse methods, Journal of Geophysical Research, 102(D25), 30069–30083, 1997.

Schwander, J., Sowers, T., Barnola, J. M., Blunier, T., Fuchs, A. and Malaizé, B.: Age scale of the air in the summit ice: Implication for glacial-interglacial temperature change, Journal of Geophysical Research, 102(D16), 19483–19493, doi:10.1029/97JD01309, 1997.

Severinghaus, J. P., Albert, M. R., Courville, Z. R., Fahnestock, M. A., Kawamura, K., Montzka, S. A., Mühle, J., Scambos, T. A., Shields, E., Shuman, C. A., Suwa, M., Tans, P. and Weiss, R. F.: Deep air convection in the firn at a zero-accumulation site, central Antarctica, Earth and Planetary Science Letters, 293, 359–367, doi:10.1016/j.epsl.2010.03.003, 2010.

Trudinger, C. M., Enting, I. G., Etheridge, D. M., Francey, R. J., Levchenko, V. A., Steele, L. P., Raynaud, D. and Arnaud, L.: Modeling air movement and bubble trapping in firn, Journal of Geophysical Research: Atmospheres, 102(D6), 6747–6763, doi:10.1029/96JD03382, 1997.

Trudinger, C. M., Etheridge, D. M., Rayner, P. J., Enting, I. G., Sturrock, G. A. and Langenfelds, R. L.: Reconstructing atmospheric histories from measurements of air composition in firn, Journal of Geophysical Research Atmospheres, 107(24), 1–13, doi:10.1029/2002JD002545, 2002.

Trudinger, C. M., Enting, I. G., Rayner, P. J., Etheridge, D. M., Buizert, C., Rubino, M., Krummel, P. B. and Blunier, T.: How well do different tracers constrain the firn diffusivity profile?, Atmospheric Chemistry and Physics, 13, 1485–1510, doi:10.5194/acp-13-1485-2013, 2013.

WAIS Divide Project Members: WAIS Divide Site Characteristics, [online] Available from: http://www.waisdivide.unh.edu (Accessed 15 November 2016), 2016.

The influence of layering and barometric pumping on firn air transport in a 2D model

Benjamin Birner[1], Christo Buizert[2], Till J.W. ~~Wagner[1]~~ Wagner[3] and Jeffrey P. Severinghaus[1]

[1]Scripps Institution of Oceanography, University of California San Diego, La Jolla, CA 92093, USA
[2]College of Earth, Ocean and Atmospheric Sciences, Oregon State University, Corvallis, OR 97331, USA
[3]Department of Physics and Physical Oceanography, University of North Carolina at Wilmington, NC 28401, USA

Correspondence to: Benjamin Birner (bbirner@ucsd.edu)

Abstract. Ancient air trapped in ice core bubbles has been paramount to developing our understanding of past climate and atmospheric composition. Before air bubbles become isolated in ice, the atmospheric signal is altered in the firn column by transport processes such as advection and diffusion. However, the influence of low~~im~~ permeabi~~l~~le~~i~~ity layers and barometric pumping (driven by surface pressure variability) on firn air transport is not well understood and cannot be captured in conventional 1-dimensional firn air models. Here we present a 2-dimensional (2D) trace gas advection-diffusion-dispersion model that accounts for discontinuous horizontal layers of reduced permeability. We find that layering ~~and~~ or barometric pumping individually yield too small a reduction in gravitational settling to match observations. In contrast, ~~a combination of both effects more strongly supresses gravitational fractionation~~when both effects are active, the model's gravitational fractionation is suppressed as observed. Layering ~~locally~~ focuses airflows in certain regions in the 2D model ~~and thus~~which acts to ~~amplifies~~ amplify the dispersive mixing resulting from barometric pumping. Hence, the representation of both factors is needed to obtain a ~~more natural~~realistic emergence of the lock-in zone. ~~Moreover~~In contrast to expectations, we find that the addition of barometric pumping in the layered 2D model does not substantially change the differential kinetic fractionation of fast and slow diffusing trace gases~~, which is observed in nature~~. ~~This suggests~~However, like 1D models, the 2D model substantially underestimates the amount of differential kinetic fractionation seen in actual observations, suggesting that further subgrid-scale ~~physics~~ processes may be missing in the current generation of firn air transport models. ~~However~~In spite of this deficiency, we find robust scaling relationships between kinetic isotope fractionation of different noble gas isotope and elemental ratios. These relationships may be used to correct for kinetic fractionation in future high precision ice core studies and can amount to a bias of up to 0.45 °C in noble gas based mean ocean temperature reconstructions at WAIS Divide, Antarctica.

1 Introduction

In the upper 50-130 m of ~~un~~consolidated snow above an ice sheet, known as the firn layer, atmospheric gases gradually become ~~gradually~~ entrapped in ~~secluded~~ occluded pores and are eventually preserved as bubbles in the ice below. Antarctic ice core records containing these trapped gases have been critical in informing our understanding of the interplay of past climate and atmospheric trace gas variability over the past 800,000 years (Petit et al., 1999; Lüthi et al., 2008). As atmospheric gases migrate through the firn, they are modified in elemental composition and isotopic signatures~~composition~~ by several competing physical processes~~ which may alter elemental concentrations and isotopic signatures~~ (Schwander et al., 1988, 1993; Trudinger et al., 1997; Buizert et al., 2012; Kawamura et al., 2013; Mitchell et al., 2015). Therefore, appropriate corrections must be applied to firn and ice core records to accurately reconstruct atmospheric trace gas histories.

Box 1| Porous media terminology

Porosity: the fraction of (firn) volume filled by gas

Permeability: the degree to which a porous medium permits viscous flow to pass through

Fickian diffusion: molecular diffusion that is proportional to the concentration gradient as described by Fick's first law

Tortuosity: measure of the twistedness of pathways through a porous medium

Firn is a layered medium, in which the denser layers can impede vertical diffusion and transport~~Abundant evidence shows from field observations, high-resolution firn density measurements, and comparisons of summer and winter ice, that (near-) impermeable horizontal layers exist in polar firn~~ (Hörhold et al., 2012; Mitchell et al., 2015; Orsi et al., 2015) (Fig. 1). The~~ir~~ significance of these layers for firn gas transport remains unclear and motivates this work. Readers who are familiar with the structure of firn and its air transport processes may wish to skip ahead to the last paragraph of this section. To build some intuition about firn transport processes, a simple analytical model of firn air transport is provided in Appendix A.

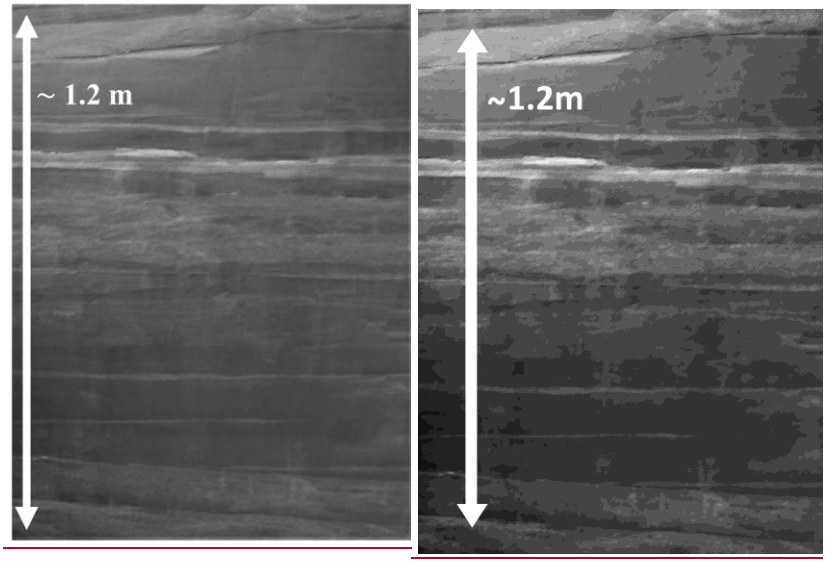

Figure 1. Layering of firn photographed in a surface pit at WAIS Divide. Image courtesy of Anaïs Orsi.

We distinguish four main processes affecting the composition of air in firn: diffusion, advection, dispersion and convective mixing. Molecular ~~Fickian d~~diffusion, driven by concentration gradients in the firn, is the primary mode of horizontal and vertical transport. Molecular diffusion also enables gravitational fractionation, or "settling", of trace gases in proportion to their masses (Schwander, 1989; Sowers et al., 1989; Schwander et al., 1993; Trudinger et al., 1997). Gravitational settling leads to an enrichment of heavy isotopes with depth that is described in equilibrium by the barometric equation (Schwander, 1989; Sowers et al., 1989; Craig et al., 1988):

$$\delta_{grav} = \left[\exp\left(\frac{g\Delta m}{R\,T} z\right) - 1\right] \times 1000\ ‰, \quad (1)$$

where $\delta \equiv \frac{r_{sample}}{r_{standard}} - 1 \equiv q - 1$, with r being~~is~~ the isotope ratio (unitless), z the depth (m), T the absolute temperature (K), Δm the isotope mass difference (kg mol^{-1}), g the gravitational acceleration (m s^{-2}), and R the fundamental gas constant (J mol^{-1} K^{-1}).

Gradual accumulation of snow and air bubble trapping leads to a slow, downward advection of the enclosed air. The net air advection velocity is slower than the snow accumulation rate (yet still downward in the horizontal average in an Eulerian framework) because compression of the porous firn medium produces a ~~return~~ flow of air ~~from the firn column to the atmosphere~~upward relative to the firn matrix (Rommelaere et al., 1997).

Buoyancy-driven convection and brief pressure anomalies associated with wind blowing over an irregular topography cause strong mixing between the near-surface firn and the unfractionated atmosphere, smoothing ~~out any~~ concentration gradients (Colbeck, 1989; Severinghaus et al., 2010; Kawamura et al., 2013). This mixing ~~Such convective mixing is usually observed only in the top few meters of the firn column. Convective mixing~~ causes ~~a~~ substantial deviations from the gravitational settling equilibrium (i.e., the solution to Eq. (1)) and leads to varying degrees of kinetic isotope fractionation because faster diffusing isotopes more ~~easily overcome the same amount of mass-independent mixing~~readily return to thermal-gravitational equilibrium by diffusion (Buizert et al., 2012; Kawamura et al., 2013).

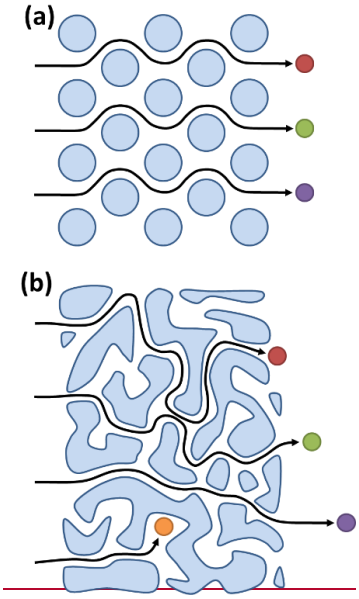

Figure 2. Schematic of (a) a non-dispersive medium and (b) a highly dispersive medium such as the deep firn. Figure reproduced from Buizert and Severinghaus, (2016).

Lastly, surface barometric pressure variability on longer timescales (> 1 hour) drives air movement down to the firn-ice transition. Building on work by Schwander et al. (1988), Buizert and Severinghaus (2016) suggest that migrating storm centressurface pressure variability may produce significant pressure gradients in the firn thatand induce fast airflows in firn. Porous firn has a high tortuosity, i.e., two points are typically connected by strongly curved paths, and the deep firn also contains many cul-de-sacs (Buizert and Severinghaus (2016), their Fig. 2)(Fig. 2). Airflow through such a medium produces mass-independent, dispersive mixing. Dispersion in this context is an emergent macroscopic phenomenon that describes microscopic velocity deviations of the flow from Darcy's law of bulk fluid flow through porous mediain different pores (Buizert and Severinghaus, 2016). This process may be accounted for by adding additional a dispersive mixing termon to the governing advection-diffusion equation traditionally used for of trace gas transport in firn (e.g., Buizert and Severinghaus, 2016).

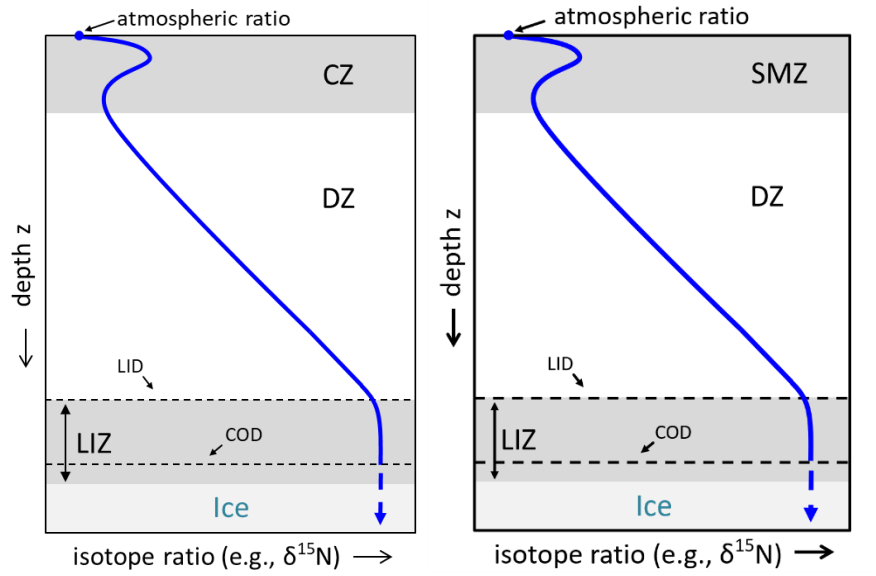

Figure 2~~3~~. Schematic depiction of a typical isotope profile. The ~~convective~~ surface mixed zone (~~CZ~~SMZ), the diffusive zone (DZ), the lock-in zone (LIZ) and the ice below are indicated by shading. Further indicated are the lock-in depth (LID) and the close-off depth (COD) (see text).

Together, these four processes yield a firn column that is ~~typically~~ split into a ~~convective~~ surface mixed zone (~~CZ~~SMZ, which has historically been labelled the convective zone), a diffusive zone (DZ) and a lock-in zone (LIZ) (Fig. 2~~3~~). The close-off depth (COD) occurs where the air content becomes fixed and pressure in open porosity increases above hydrostatic pressure. We prefer the term "surface mixed zone" over the more commonly used terminology "convective zone" to acknowledge the dual nature of mixing driven by convection and high-frequency pressure variability in this region. The SMZ~~CZ~~ is rather well-mixed with a trace gas composition similar to the atmosphere. Nevertheless, large seasonal thermal gradients can lead to isotopic fractionation which is only partially attenuated ~~by convective mixing~~ (Severinghaus et al., 2001, 2010; Kawamura et al., 2013). Molecular diffusion dominates in the DZ but ~~the~~ effective firn diffusivity decreases with depth ~~to represent~~due to the ~~hindering~~ increasing influence~~effect~~ of tortuosity ~~on~~ hindering diffusion. Throughout the DZ, gravitational settling leads to an enrichment of all isotopes heavier than air in proportion to their mass difference. The top of the LIZ, the somewhat ~~ill-~~poorly defined lock-in depth (LID) horizon, is commonly deduced from a rather sudden change in the slope of the $\delta^{15}N$, CO_2 or CH_4 profiles. Gravitational enrichment of isotopes ceases in the LIZ and isotope ratios remain constant with depth. We term any such deviation from gravitational equilibrium "disequilibrium" (without implying that such a situation is not in steady-state).

The physical mechanism responsible for the cessation of gravitational enrichment in the deep firn is still not fully understood. Since CFCs and other anthropogenic tracers have been detected in firn air measurements from the LIZ well below the depth expected from pure advection, it is clear that some amount of vertical transport by molecular diffusion or dispersion continues in the LIZ (Severinghaus et al., 2010; Buizert et al., 2012; Buizert and Severinghaus, 2016). However, no further

gravitational settling of isotopes occurs in the LIZ as indicated by constant $\delta^{15}N$ values. Furthermore, the vertical transport in the LIZ appears to be at least to some degree mass- and diffusivity-dependent ~~because~~ since the faster diffusing CH_4 advances further in the LIZ than the slower diffusing gases CFC-113 or CO_2 (Buizert et al., 2012). Therefore, transport in the LIZ cannot be explained by either mass-indiscriminate dispersive mixing or molecular diffusion alone. Most current 1D firn air models use a greatly reduced molecular diffusivity in the lock-in zone and simultaneously introduce a mass-independent mixing term tuned to match measured trace gas profiles (Buizert et al., 2012). A physical mechanism to justify these numerical methods remains elusive. An attempt at a physical explanation was given by Buizert and Severinghaus (2016), who ~~Buizert and Severinghaus (2016)~~ introduced barometric pumping in a 1D firn model. ~~The authors observed a significant effect of barometric pumping on the $\delta^{15}N$ profile but needed to invoke a highly idealized parametrization of firn layering to match observations due to the intrinsic difficulties of representing layers in 1D.~~

Here, we explore the possibility that non-fractionating trace gas mixing in deep firn may be explained by the combination of barometric pumping and discontinuous horizontal layers that have nominal diffusivity~~by discontinuous layers of zero diffusivity and barometric pumping~~. High density layers are empirically linked to low vertical permeability (and thus diffusivity),~~porosity, diffusivity and permeability,~~ increasing the firn's tortuosity and forcing extensive horizontal transport. The influence of layering ~~and horizontal inhomogeneity~~ on firn gas transport is mostly untested in numerical models so far since previous firn air models were generally limited to one dimension. In particular, we will test two mechanisms by which density layering could influence isotope ratios in firn air: (i) Layering may ~~(i)~~ reduce gravitational settling of isotopes because ~~the driving force for gravitational settling is effectively zero~~vertical settling of isotopes is absent during horizontal transport along layers; (ii) L~~and l~~ayering may ~~(ii)~~ modulate the mass-independent dispersive mixing effect of barometric pumping. Our analyses will focus on two Antarctic high-accumulation sites, WAIS Divide and Law Dome DSSW20K (Trudinger et al., 2002; Battle et al., 2011).

2 Methods

2.1 Governing equation and firn properties

We model 2D trace gas transport in firn ~~is simulated~~ by numerically solving the advection-diffusion-dispersion equation, known from hydrology (Freeze and Cherry, 1979), adapted to firn (following Schwander et al., 1993; Rommelaere et al., 1997; Trudinger et al., 1997; Severinghaus et al., 2010; Buizert et al., 2012; Kawamura et al., 2013;Buizert and Severinghaus, 2016),

$$\tilde{s}\frac{\partial q}{\partial t} = \vec{\nabla}\cdot\left[\tilde{s}\boldsymbol{D}_m\left(\vec{\nabla}q - \frac{\Delta m\,\vec{g}}{R\,T}\,q + \Omega\frac{\partial T}{\partial z}q\,\hat{k}\right) + \tilde{s}\boldsymbol{D}_d\vec{\nabla}q\right] - (\tilde{s}\,\vec{u})\cdot\vec{\nabla}q \qquad (2)$$

with $q \equiv \delta + 1$ the ratio of any isotope to $^{28}N_2$ compared to a standard material, $\tilde{s} \equiv s_{op}\exp\left(\frac{\Delta mgz}{RT}\right)$ the pressure-corrected open porosity ($m^3\ m^{-3}$), T temperature (K), Ω thermal diffusion sensitivity (K^{-1}), and $\vec{u}$ the advection velocity ($m\ s^{-1}$). $\boldsymbol{D}_m$ and

$\boldsymbol{D}_d$ are the 2D molecular diffusion and dispersion tensors ($m^2\ s^{-1}$). $\vec{\nabla} q$ is the concentration gradient and $\vec{\nabla} \cdot$ denotes the 2D divergence operator. From left to right, the terms of Eq. (2) represent the rate of change in concentration/isotope ratio, Fickian diffusion, gravitational fractionation, thermal fractionation, dispersive mixing and advection. Since Eq. (2) is only valid for the binary diffusion of a trace gas into a major gas, ratios of any two isotopes of masses x and y are obtained by separately simulating the ~~diffusion~~ transport of each isotope into the major gas $^{28}N_2$ and using the relationship

$$q_{x/y} = \frac{q_{x/28}}{q_{y/28}} \tag{3}$$

to calculate the isotope ratios of interest (Severinghaus et al., 2010).

Isotope ratios are assumed to be constant at the surface (Dirichlet boundary) and reconstructions of atmospheric CO_2 and CH_4 concentrations over the last 200 years are used to force runs of these anthropogenic tracers (see Supplementary Information (SI)). The model time step is 3.5 days; smaller time steps make the model impractical to run due to computational costs. The bottom boundary is implemented by allowing only the advective flux to leave the domain (Neumann boundary). Diffusion and dispersive mixing cease below the COD. A periodic boundary condition is used in the horizontal direction. The horizontal extent of the model is varied between sites with differing snow accumulation rates to maintain a constant ratio of annual layer thickness to the model's spatial extent, which affects barometric pumping velocity. Firn density (Fig. ~~4a~~3a) is prescribed from a fit to the measured density profile at each site. Following Severinghaus et al. (2010) and Kawamura et al. (2013), empirical relationships are used to derive open and closed porosities from the density profile (Fig. ~~4b~~3b). The pressure-corrected open porosity $\tilde{s}$ is assumed to be time independent.

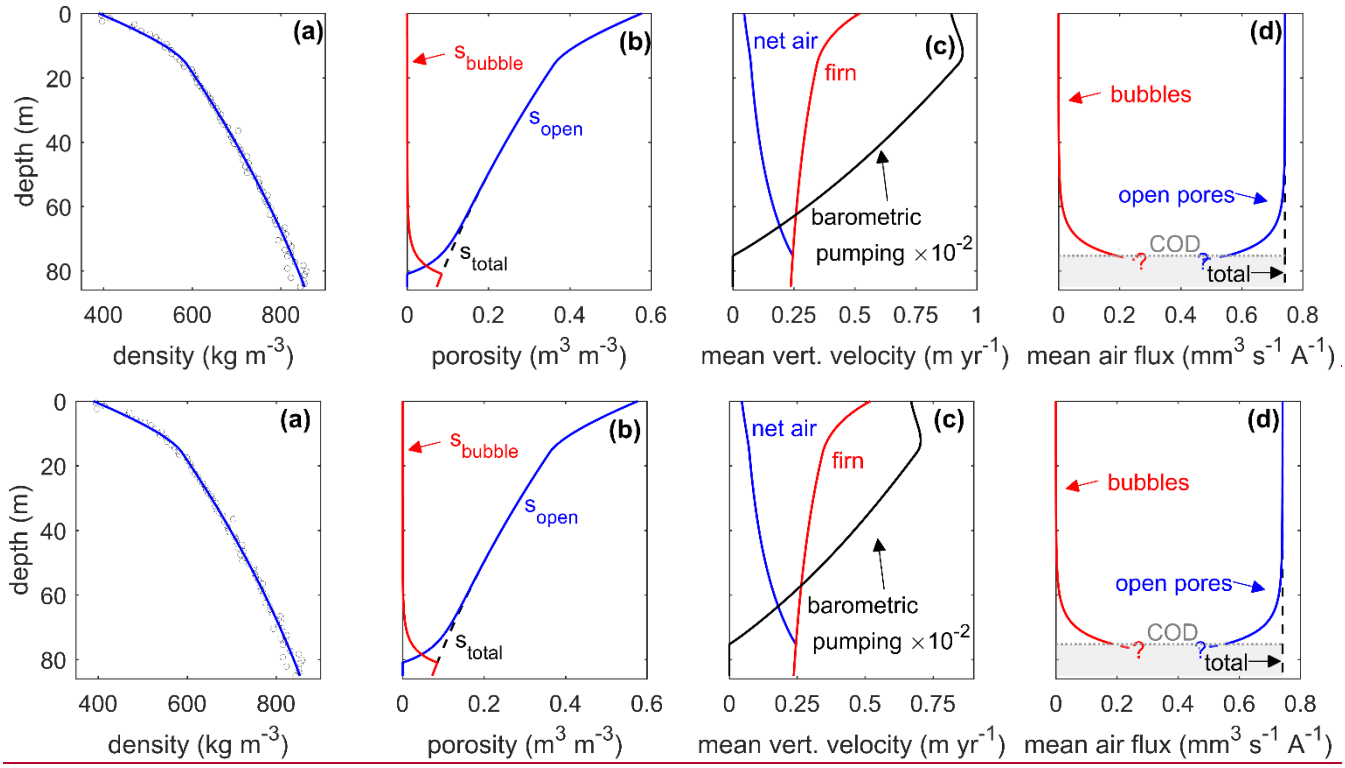

Figure 34. Firn conditions and modelled velocities profiles at WAIS Divide. (a) Density fit to observed data (data from Battle et al., 2011)~~,~~ (b) open, bubble (i.e., closed) and total porosity~~,~~ (c) horizontally averaged barometric pumping ~~strength~~ velocity (i.e., time-mean horizontal average of $|\vec{u}_b|$, black), and horizontally averaged net air velocity($\vec{w}_{firn} + \vec{u}_r$, blue) and firn velocity ($\vec{w}_{firn}$, red)~~, and~~; (d) mean air flux in open pores (blue) and bubbles (red).

2.2 Advection velocity and barometric pumping

The 2D velocity field $\vec{u}$ is a result of a combination of (i) air migration with the firn ($\vec{w}_{firn}$), (ii) return flow of air $\vec{u}_r$ ~~from~~ the firn to the atmosphere due to the gradual compression of pores ($\vec{u}_r$), and (iii) airflow resulting from barometric pumping $\vec{u}_b$ (Figs. ~~4c~~ 3c & ~~5~~4). Details on the~~ir~~ derivation of these velocities are provided in the SI. In short, $\vec{w}_{firn}$ ~~is the vertical advection of snow and air in the firn column and~~ is constrained by assuming a time-constant snow and ice mass flux at all depths. ~~The return flow~~ $\vec{u}_r$ is calculated based on the effective export flux of air in open and closed pores at the close-off depth (COD), imposing a constant mean vertical air flux throughout the firn column (Fig. ~~4d~~3d) (Rommelaere et al., 1997; Severinghaus and Battle, 2006). ~~Finally, the barometric pumping flow~~ $\vec{u}_b$ is the airflow needed to re-establish hydrostatic balance in the firn in response to any surface pressure anomaly. Surface pressure variability is represented by (pseudo-) red noise, mimicking observed pressure variability at both sites. The near-coast location Law Dome is more strongly affected by storm activity than WAIS Divide with pressure variability ~11.2 hPa day^{-1} compared to ~7 hP day^{-1} at WAIS Divide. $\vec{u}_r$ and $\vec{u}_b$ follow Darcy's law of flow through porous media (Darcy, 1856):

$$\vec{u} = -\frac{\kappa}{\tilde{s}\,\mu}\nabla P, \tag{4}$$

with ∇P the pressure gradient, κ the permeability of firn, and μ the viscosity of air (Fig. ~~5~~4).

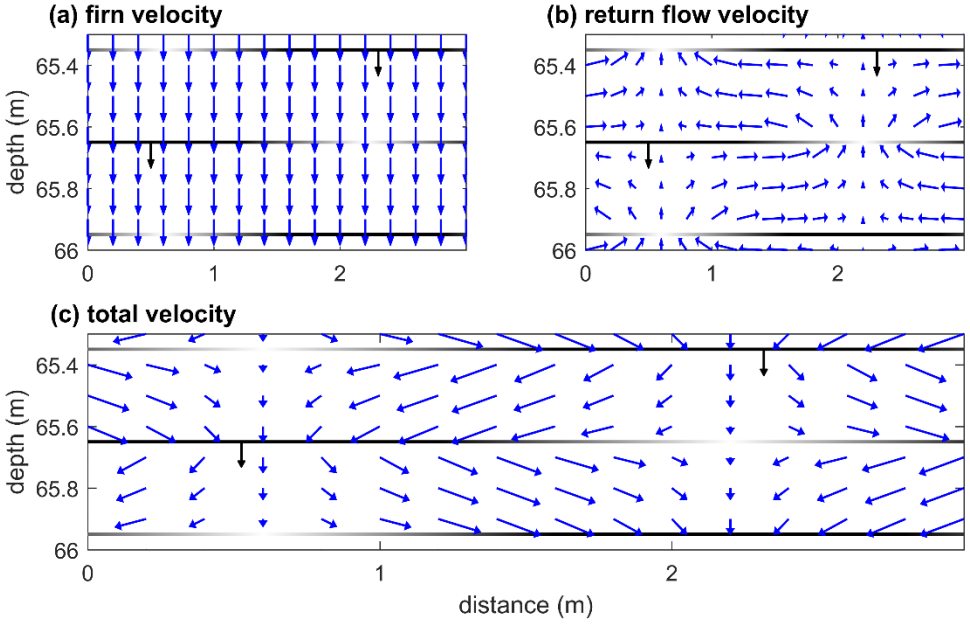

Figure ~~4~~5. The different components of the velocity field. ~~A linear combination of~~ (a) ~~the~~ firn velocity ~~and~~; (b) the velocity of air return flow to the atmosphere due to pore compression ~~yield~~; (c) ~~the~~ net firn air advection velocity ~~used in the model for a certain layer configuration~~(a linear combination of the fields in panels a ad b). Because of its alternating direction, barometric pumping yields no net flow but instantaneous flow field patterns look similar to panel (b). Black arrows indicate the ~~slow~~ downward advection of layers at the firn velocity.

2.3 Firn layering

Idealized firn layering is implemented by forcing the vertical velocity components u_r and u_b, as well as all vertical diffusive fluxes between the grid boxes on either side of a layer to be zero. Only the advection of air with the firn ($\vec{w}_{firn}$) remains active at~~for~~ these grid box boundaries. Layering limits vertical gas transport and yields almost exclusively horizontal transport between layers. ~~Here, we~~We ~~represent~~ assign layers ~~to have~~an infinitesimal thickness~~,~~ because of the computationally limited spatial resolution of the model. Layers are repeatedly introduced at a specific depth and migrate down with the velocity of the firn. The vertical distance between layers is set to correspond to the snow accumulation of one year and the horizontal extent of layers increases linearly with depth until they cover the entire domain at the close-off depth (COD). The mean layer opening size is held proportional to the annual layer thickness ~~at all sites~~ to make the vertical advection velocities independent of the arbitrary horizontal extent of the model. To obtain more realistic flow fields, the permeability of layers ~~tapers off at~~increases gradually towards both ends of a layer.

2.4 Dispersive mixing

The dispersion tensor $\boldsymbol{D}_d$ is made up of two components, (i) ~~convective~~ non-fractionating mixing of air in ~~a shallow region near the surface~~the SMZ and (ii) dispersive mixing caused by barometric pumping in the tortuous firn medium ~~in the more tortuous, deep firn~~. First, the ~~well-mixed convective zone~~SMZ is commonly represented by mass-independent ("eddy") diffusion acting in the vertical and horizontal directions. The corresponding diffusivity profile ~~of convective mixing $D_e = D_{eSMZ}(z)$~~ is pre~~de~~scribed as an exponential decay away from the snow-atmosphere interface (Kawamura et al., 2013). Its maximum surface value and the decay constant are chosen to match observed $\delta^{15}N$ values in the deep firn. After reaching a specified maximum depth of 8 m ~~or 14 m~~ at WAIS Divide and 14 m at Law Dome DSSW20K, D_{SMZ} ~~respectively, the diffusivity~~ tapers linearly to zero over 2 m.

Second, airflow through any dispersive medium leads to mixing in the directions longitudinal and transverse to the flow~~longitudinal-to-flow (i.e., along the flowline) and transverse-to-flow (i.e., across the flowline) mixing~~. Because barometric pumping velocities are orders of magnitude faster than the return flow, dispersive mixing is dominated by barometric pumping. ~~The 2D dispersion tensor becomes:~~

~~$$\boldsymbol{D}_d = \begin{bmatrix} D_L \frac{u_n^2}{v^2} + D_T \frac{w_n^2}{v^2} + D_e & \frac{u_n w_n}{v^2}(D_L - D_T) \\ \frac{u_n w_n}{v^2}(D_L - D_T) & D_T \frac{u_n^2}{v^2} + D_L \frac{w_n^2}{v^2} + D_e \end{bmatrix}, \quad (5)$$~~

~~where $u_n \equiv u_r + u_b$ and $w_n \equiv w_r + w_b$ are the sum of the return and barometric pumping velocity components in the x- and the y-directions with $v \equiv (u_n^2 + w_n^2)^{0.5}$. D_L and D_T are the longitudinal- and transverse-dispersion coefficient ($m^2\ s^{-1}$), respectively. D_L and D_T are commonly approximated as linear functions of velocity (Freeze and Cherry, 1979)~~

~~$$D_L = \alpha_L v \quad (6)$$~~

~~$$D_T = \alpha_T v \quad (7)$$~~

~~where the proportionality factors α_L and α_T are the longitudinal- and transverse-to-flow dispersivity (m).~~

The degree of dispersive mixing in firn presumably depends on the direction of flow and ~~probably also~~ differs between the longitudinal-to-flow and transverse-to-flow direction. However, the treatment of anisotropic media is complex and only one parametrization for vertical, longitudinal-to-flow dispersion in firn is currently available (Buizert and Severinghaus, 2016). Therefore, we assume that the dispersivity α of firn is isotropic ~~(i.e., $\alpha_L = \alpha_T \equiv \alpha$).~~and linearly dependent on the magnitude of the flow velocity vector ($v \equiv |\vec{u}_b + \vec{u}_r|$). ~~In this case, the 2D dispersion tensor becomes~~This simplifies ~~$\boldsymbol{D}_d$~~ to

$$\boldsymbol{D}_d = (\alpha\, v + D_{eSMZ})\, \boldsymbol{I}, \quad (8)(5)$$

with $\boldsymbol{I}$ the second order identity matrix (Freeze and Cherry, 1979; Buizert and Severinghaus, 2016). The dispersion flux term in Eq. (2) ~~becomes~~simplifies to

$$\tilde{s}\boldsymbol{D}_d\vec{\nabla}q = \tilde{s}\,[\alpha\, v + D_{eSMZ}]\,\vec{\nabla}q. \qquad (9)(6)$$

The dispersivity parametrization of Buizert and Severinghaus (2016) is based on direct measurements of cylindrical firn samples from Siple Station, Antarctica, performed by Schwander et al. (1988). The parameterization relates dispersivity to open porosity s_{op} as

$$\alpha(s_{op}) = \tilde{s}\,[1.26 \cdot \exp(-25.7\, s_{op})]. \qquad (10)(7)$$

~~Here, the~~A factor of $\tilde{s}$ was added to the original parameterization by Buizert and Severinghaus (2016) because α relates dispersive mixing to the velocity components u_n and w_n, that denote flow velocities per unit pore cross-section (w_{pores}). Schwander et al. (1988), however, originally measured the considerably slower bulk airflow per unit firn cross-section (i.e., $w_{bulk} = \frac{w_{pores}}{\tilde{s}}$). Since dispersivity is a scale dependent property, it is important to use parametrizations that are compatible with the resolution of the numerical model. The sample size of Schwander et al. (1988) (i.e., 30 mm diameter & 50 mm length) approximately matches the resolution of our numerical model (i.e., 30 x 40 mm) and thus should adequately approximate subgrid-scale (i.e., pore-scale) mixing processes that currently cannot be resolved. Spatial inhomogeneity of subgrid-scale firn dispersivity that was not captured by the sampling of Schwander et al. (1988) cannot be accounted for in the model. Dispersion on larger scales such as the interaction of flow and layers is explicitly represented in the model by the interplay of advection and diffusion. Thus, dispersive mixing is ~~completely~~ fully constrained in the model and based on empirical parameterizations that are not subject to ~~any~~ tuning.

2.5 Molecular diffusion

The (effective) molecular diffusivity profile is established by simultaneously fitting the simulated CO_2 and CH_4 profile to real firn measurements at both sites. Effective vertical diffusivity decreases with depth to represent the subgrid-scale effect of decreasing pore connectivity and increasing firn tortuosity, which is not fully represented by the explicit macroscopic layers in our model. A spline function ~~defines~~ is used to obtain the effective vertical diffusivity profile, which decreases monotonically from the surface to zero at the COD (Fig. ~~6~~5). Diffusivities for other trace gases are calculated by scaling the tuned CO_2 diffusivity by the free air diffusivity of each gas relative to CO_2 (Trudinger et al., 1997). The diffusivity tuning presents an underconstrained problem because horizontal and vertical molecular diffusivities are essentially free parameters. It is qualitatively evident from firn air sampling that horizontal connectivity/diffusivity is much higher than vertical diffusivity in ~~the~~ deep firn, but ~~this observation is incompletely quantified~~no satisfactory quantification of this anisotropy is available. As a best guess estimate, we set ~~Here,~~ horizontal molecular diffusivities ~~are fixed to 10x~~equal to 10x the vertical diffusivity at the

same depth. ~~and annual layers represented some fraction of the total tortuosity explicitly in the model.~~ There are many degrees of freedom in tuning molecular diffusivities and ~~the~~ our diffusivity parameterization is therefore not unique~~.~~ However, sensitivity tests with equal horizontal and vertical diffusivity in the model (compensated by shorter horizontal layers) yield comparable results.

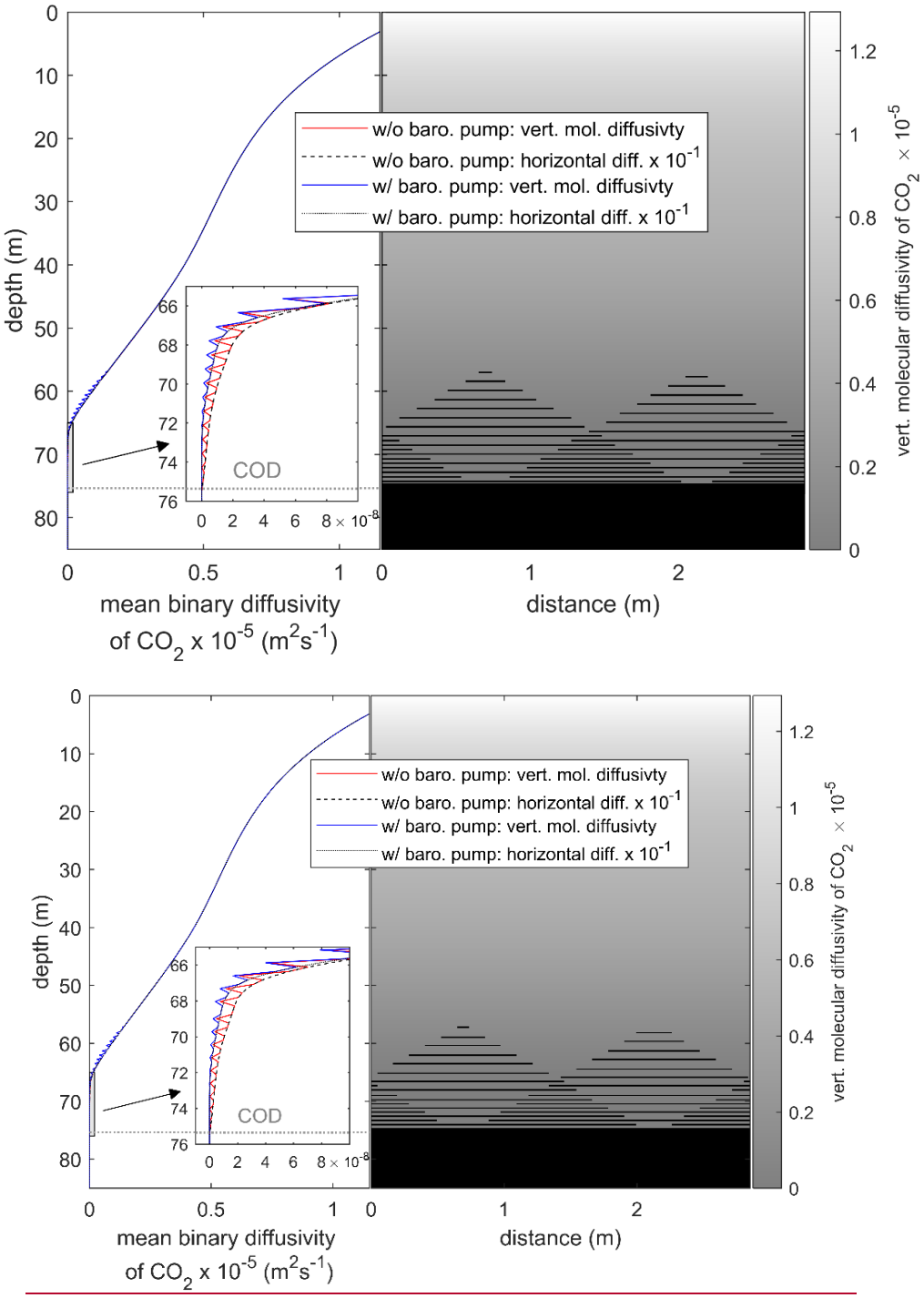

Figure 5~~6~~. The CO_2 diffusivity profile at WAIS Divide. Left panel: Horizontally averaged, vertical and horizontal diffusivity in the model with and without barometric pumping. Right panel: map of diffusivity in the 2D model without barometric pumping. Only every third layer present in the model is shown here for clarity.

2.6 Thermal fractionation and ~~the~~ temperature model

Finally, a 1D vertical thermal model by Alley and Koci (1990) is run separately to simulate the temperature evolution of the firn. The model is forced by a long-term surface temperature trend based on published records by Van Ommen et al. (1999), Dahl-Jensen et al. (1999) and Orsi et al. (2012). A ~~generic~~ mean Antarctic seasonal cycle derived from a ~8-10-year climatology of automatic weather station observations at WAIS Divide and Law Dome (Lazzara et al., 2012) is superimposed on this trend. Alley and Koci's temperature model is based on the heat transport equation for firn (Johnsen, 1977) with parametrizations for firn thermal properties from Weller and Schwerdtfeger (1977). Horizontal temperature gradients in firn are small at both sites and neglected in this study.

Considerable temperature gradients can exist in present-day firn because of recent global atmospheric warming and these gradients can lead to increased isotope thermal fractionation, in particular of $\delta^{15}N$. The sensitivity of isotopes to diffuse in response to temperature gradients is captured by the thermal diffusion sensitivity Ω. ~~Values of~~The temperature dependence of Ω ~~are~~ is approximated as a function of the effective average temperature T in Kelvin:

$$\Omega = \frac{a}{T} - \frac{b}{T^2} \qquad \text{~~11)~~(8)}$$

or Ω is assumed to be temperature independent if the ~~temperature sensitivity is~~coefficients a and b are unknown for a specific isotope ratio (Severinghaus et al., 2001). Coefficients a and b were determined experimentally for different isotope ratios by Grachev and Severinghaus (2003a, 2003b) and~~,~~ Kawamura et al. (2013) ~~and Kawamura (unpublished)~~.

A ~~detailed overview of further~~table of all model parameters and further details of the numerical realization of 2D gas transport ~~may be found~~is provided in the SI ~~(SI Sect. 1-4)~~.

3 Results

3.1 WAIS Divide

3.1.1 CO_2 and CH_4

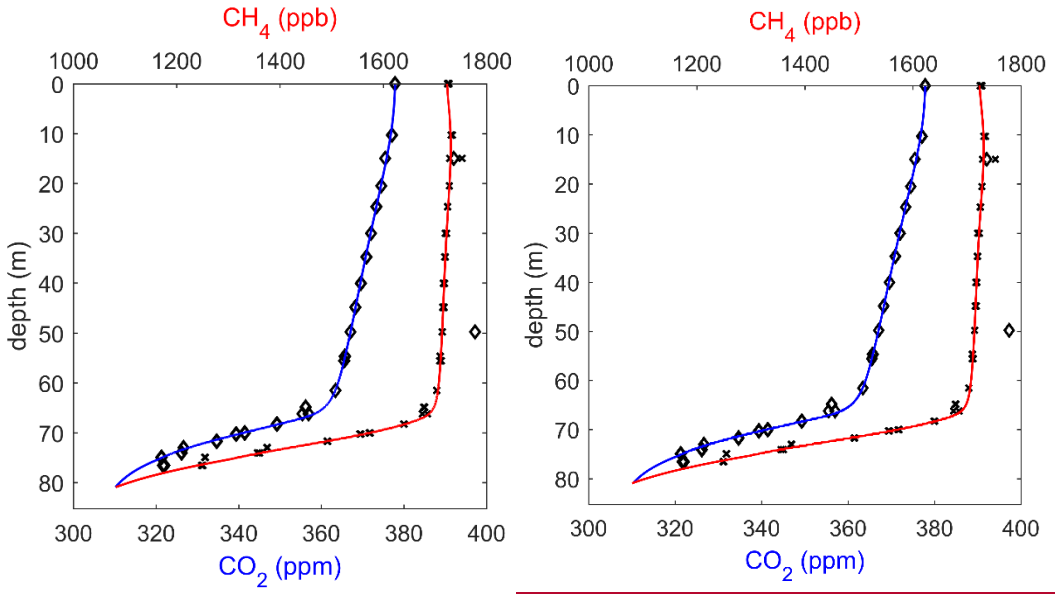

Figure 6~~7~~. Simulated and observed CO_2 and CH_4 concentrations in the firn at WAIS Divide. The model is initialized with the recorded atmospheric trace gas concentrations in 1800 CE at all depths and is forced at the surface with histories of atmospheric CO_2 and CH_4 concentrations (Etheridge et al., 1996, 1998; Keeling et al., 2001; Buizert et al., 2012; Dlugokencky et al., 2016a, 2016b). Markers indicate observed CO_2 (diamonds) and CH_4 (crosses) concentrations (Battle et al., 2011). Based on high CO_2 and CH_4, two samples at ~15 m and ~50 m depth were likely compromised by modern air during analysis and are thus ignored in the curve fit. Differences in the CO_2 and CH_4 profiles between the 1D model and the 2D model with or without barometric pumping are not visible at the resolution of this figure but are illustrated in the SI (Fig. S12~~9~~).

A comparison of simulated and observed CO_2 and CH_4 profiles shows good agreement at WAIS Divide, supporting the plausibility of our layered diffusivity parameterization (Fig. ~~7~~6). In line with observations, both CO_2 and CH_4 concentrations decrease slowly with depth until ~68 m below the surface due to the gradually increasing gas age and the anthropogenic rise in atmospheric CO_2 and CH_4 concentrations. ~~where they begin to~~The more rapid decrease ~~more rapidly~~of CO_2 and CH_4 below ~68 m is explained by a much slower vertical penetration of air and a faster increase of the gas age with depth in the LIZ.

In the following discussion we will examine and compare results from four different ~~permutations~~ versions of the 2D model: with or without impermeable layers and with activated or deactivated barometric pumping. In versions without layering, our 2D model loses all horizontal heterogeneity and will thus be referred to as a ~~'~~"1D ~~model'~~ model" in what follows~~throughout the text~~. Since the explicitly implemented tortuosity from layering in the 2D model affects molecular diffusion and dispersion equally it is represented by ~~equally~~ lowering the effective molecular diffusivity and dispersivity equally in the layered region of the 1D version instead. Diffusivities are tuned such that the CO_2 profiles are (nearly) identical. The small remaining

deviations in CO_2 and CH_4 concentrations between model ~~permutations~~ versions (< ±0.~~5~~ 8 ppm and < ±~~5~~ 9 ppb, respectively) are illustrated in ~~the SI (~~Fig. S~~9~~12~~)~~.

3.1.2 $\delta^{15}N$ and thermal fractionation

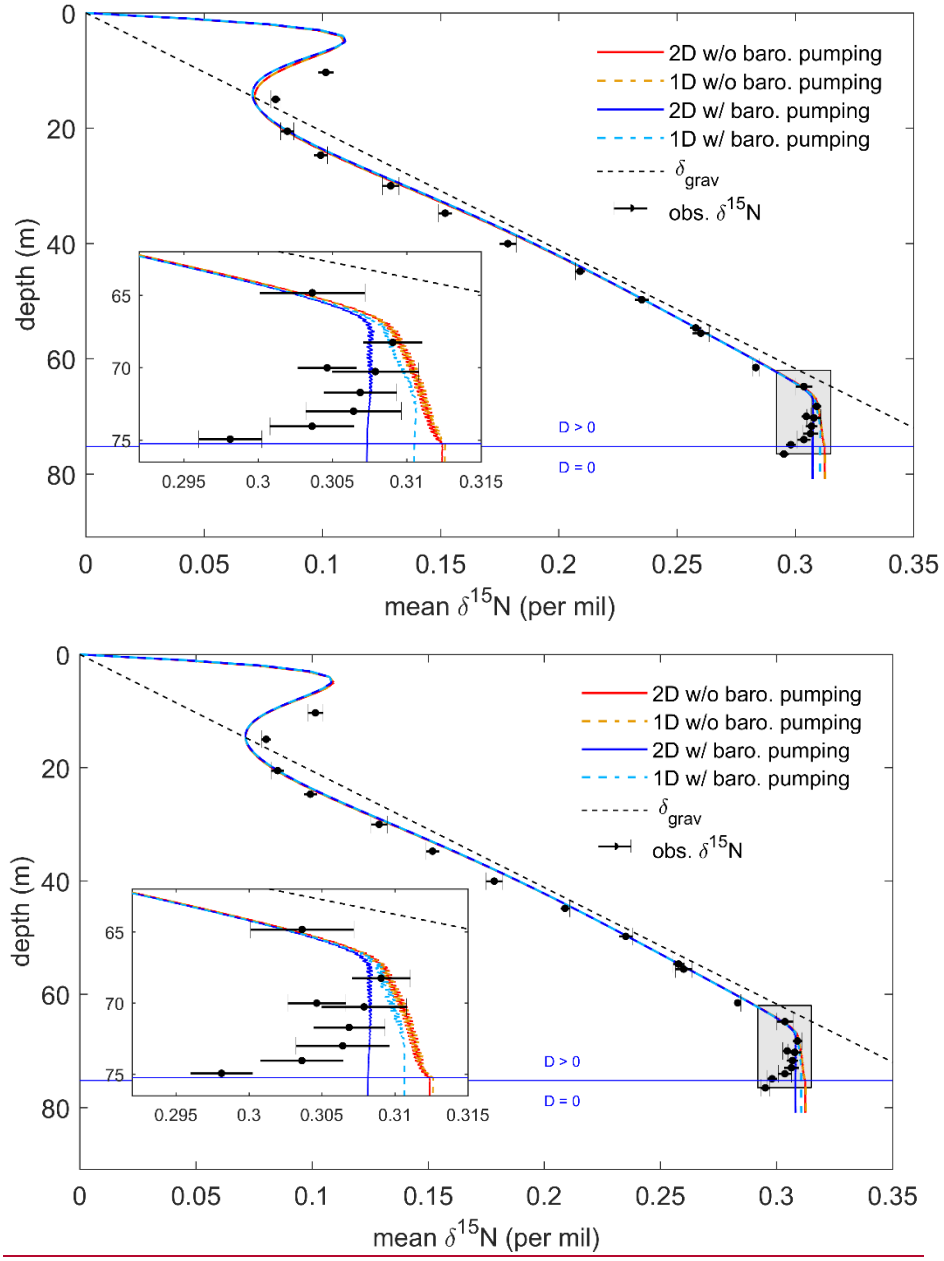

Figure ~~7~~8. Horizontally averaged $\delta^{15}N$ at WAIS Divide. Model output is shown from four different versions of the 2D model (see text). Black circles with error bars indicate the observed firn $\delta^{15}N$ (Battle et al., 2011). The dashed black line represents the equilibrium solution

for pure gravitational settling (δ_{grav}). The horizontal blue line marks the depth where vertical diffusivity reaches zero. The ~~inlay~~ inset shows a magnification of the lock-in zone.

In all four model setups, the seasonal cycle of temperature dominates the shape of the $\delta^{15}N$ profiles in the top ~30 m (Fig. ~~8~~7). Warm summer temperatures drive the migration of heavy isotopes into the colder firn below and produce a $\delta^{15}N$ summer peak just below the surface (Severinghaus et al., 2001). In contrast, a minimum of $\delta^{15}N$ occurred in this region during the previous winter season when the thermal gradients were reversed. The remnants of this winter minimum are still visible in the gas record as anomalously low $\delta^{15}N$ values below the summer peak. The differences between observations and simulated $\delta^{15}N$ values in the top of the firn column are likely caused by ~~the~~ our idealized representation of the seasonal cycle in the model. ~~Anomalous temperature gradients associated with extraordinary weather events just before firn air sampling will modify the observed $\delta^{15}N$ at the site but are unaccounted for in the model.~~

3.1.3 Impact of ~~(near-) impermeable~~reduced-permeability layers

In the layered 2D model without barometric pumping, the simulated $\delta^{15}N$ values are close to observations at the top of the LIZ but continue to increase with depth (Fig. ~~8~~7). This is contradicted by observational data even when the unusually low $\delta^{15}N$ values ~~right on~~at the COD and below are not taken into consideration (near the COD, firn air ~~pumping~~ sampling becomes more difficult in the field and the potential for fractionation during sampling is increased). A closer inspection of the lock-in zone in Figs. ~~8~~ 7 and ~~9~~ 8 reveals a zigzag pattern in the $\delta^{15}N$ profile where impermeable layers are present. Simulated ~~I~~isotope ratios are higher just above horizontal layers, where heavy isotopes can accumulate, and are anomalously low below layers where ~~they~~ heavy isotopes are more readily removed than supplied by gravitational settling. Gravitational settling through gaps in the layers sets up small horizontal concentration gradients that drive horizontal Fickian diffusion. Layering increases the effective travel path length for molecules and reduces the effective vertical diffusivity by increasing the tortuosity. However, layering alone appears to be insufficient to prevent gravitational settling completely, ~~because~~ with continued gravitational enrichment beingis observed in the LIZ in this model version.

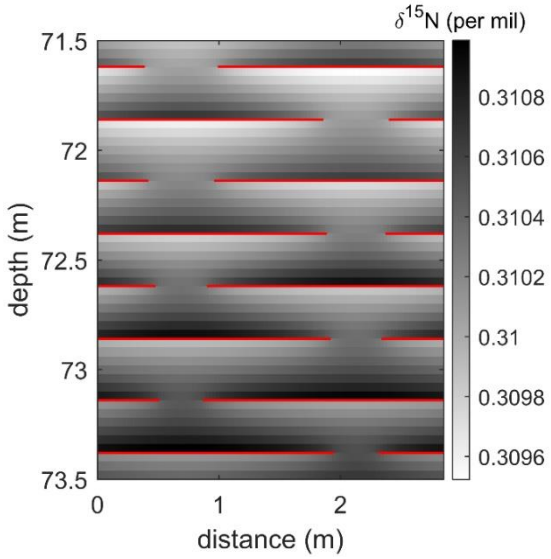

Figure ~~8~~9. Simulated $\delta^{15}N$ in a part of the lock-in zone at WAIS Divide from the 2D model not including barometric pumping. Impermeable horizontal layers are shown in red. The ~~openings sizes~~size of the openings in the layers shrink with increasing depth.

Is the impact of layers on the firn trace gas profile larger for isotopes such as $\delta^{15}N$ than for anthropogenic tracers such as CO_2, CFCs, or CH_4? All three gases have experienced large atmospheric variability in the industrial era. Therefore, the migration of these gases into the firn is dominated by vertical and horizontal Fickian diffusion~~. in contrast to~~ For $\delta^{15}N$, on the other hand, ~~where~~ the effect of gravity is critical for transport. To answer the above question, we compare output from the layered 2D model to the 1D model without layers. We find that $\delta^{15}N$ values in the 1D and 2D model without barometric pumping are almost identical (Fig. ~~8~~7). Layering in the 2D model increases the effective transport distance ~~of~~ for CO_2 just as much as for $\delta^{15}N$ and there is no disproportional impact of layering on gravitationally fractionated isotope ratios. Differences in explicitly represented tortuosity are automatically compensated in the 1D model during tuning to the same CO_2 profile by reducing molecular diffusivities. Therefore, we conclude that layering alone cannot simultaneously explain the observed CO_2 and $\delta^{15}N$ patterns.

3.1.4 Barometric pumping and the emergence of the LIZ

$\delta^{15}N$ values simulated by the 1D and 2D model with barometric pumping are lower in the LIZ than in both model versions without barometric pumping (Fig. ~~8~~7). Accounting for barometric pumping improves the agreement with observations throughout the lock-in zone. However, the reduction of gravitational fractionation is substantially stronger when layers are present. Only when both layering and barometric pumping are accounted for in the model simultaneously, does the $\delta^{15}N$ profile correctly indicate no further gravitational enrichment in the LIZ and ~~closely~~ match~~es~~ observations more closely. Dispersive mixing is nearly independent of molecular mass and does not lead to gravitational fractionation, but rather acts to eliminate the concentration gradients associated with gravitational settling. Although barometric pumping velocities are largest near the

surface (Fig. ~~4c~~3c), significant dispersive mixing is generally limited to the LIZ because ~~the~~ dispersivity of firn is inversely related to the open porosity in the parameterization of Buizert and Severinghaus (2016) and dispersion is overwhelmed by molecular diffusion in the DZ. Furthermore, molecular diffusivities drop rapidly in the LIZ ~~when barometric pumping is active~~ in the model (Fig. ~~6~~5). Because dispersion provides an additional transport mechanism for trace species, even less molecular diffusion is needed to match observed CO_2 and CH_4 concentrations in the LIZ when barometric pumping is active. Layering amplifies the importance of barometric pumping because gravitational fractionation between annual layers is restricted into the small gaps in the LIZ (Fig. ~~9~~8). Narrow pathways~~A lack of alternative pathways~~ ~~amplifies~~ amplify barometric pumping flow~~s~~ velocities and thus dispersive mixing in these regions (Fig. ~~5~~4), thus overwhelming the influence of gravitational fractionation more readily than in the 1D model. This effect is responsible for the larger differences between the $\delta^{15}N$ profiles obtained from the two model~~s~~ versions with barometric pumping in Fig. ~~8~~7. The strength of dispersive mixing in our layered 2D model is physically motivated; thus, barometric pumping and layering together lead to a more natural emergence of the $\delta^{15}N$-defined lock-in zone in the 2D model.

3.1.5 The ~~convective~~ surface mixed zone ~~height~~depth

We estimate the depth of the ~~convective~~ SMZ~~zone~~ at WAIS Divide to be ~2.8 m. Multiple different procedures have been used to estimate ~~convective zone~~SMZ ~~heights~~ thickness in the past, many of which rely on $\delta^{15}N$ data in the deep firn near the LIZ (Battle et al., 2011). However, if the deep firn is affected by dispersive mixing due to barometric pumping, these estimates may be falsely attributing some fraction of the dispersive mixing in the deep firn to the SMZ~~convective zone~~. To address this problem, we follow the method of Severinghaus et al. (2010) in calculating SMZ~~convective zone~~ thickness. This approach compares the depth where $\delta^{15}N$ reaches a certain value in two different model configurations with ~~and without convection~~zero and non-zero values of D_{SMZ}. Thermal effects are neglected. The first setup is the 2D model with barometric pumping as presented above but the dispersivity is set to zero everywhere without retuning the model. The ~~convective zone~~SMZ ~~height~~ thickness is calculated from the depth difference between this model run and a second model run where barometric pumping is deactivated, $D_{SMZ} = 0$~~and the convective zone are deactivated~~, and thus only advection and gravitational fractionation shape the profile of $\delta^{15}N$. Our ~~height~~ depth estimate of 2.8 m is within the range of values from 1.4 to 5.2 m published previously (Battle et al., 2011).

3.2 Law Dome DSSW20K

At Law Dome DSSW20K, the firn thickness is ~20 m less than at WAIS Divide. Accumulation rates are comparable, but annual-mean temperatures are ~10 K warmer. The ~~convective zone~~SMZ is slightly deeper and barometric pumping is stronger at Law Dome, yielding more ~~convective~~near-surface and dispersive mixing. Constraining the ~~convective zone height~~ SMZ depth at DSSW20K is ~~complicated~~ more difficult because ~~less~~ fewer $\delta^{15}N$ measurements are available for this site, and their associated uncertainty is, at $\pm$15 per meg, much larger than at the more recently sampled WAIS Divide site (Trudinger et al., 2002). Molecular diffusion generally takes a less important role at DSSW20K and molecular diffusivities obtained by tuning

are about half or less than those at WAIS Divide for most of the firn column. Thermal fractionation has a weaker impact on the isotope record near the surface at Law Dome due to the smaller amplitude of the seasonal cycle and stronger ~~convective~~ near-surface mixing compared to WAIS Divide. Figures of molecular diffusivity, advection velocities and other firn properties at site DSSW20K are ~~available~~ provided in the SI ~~Sect. 5~~.

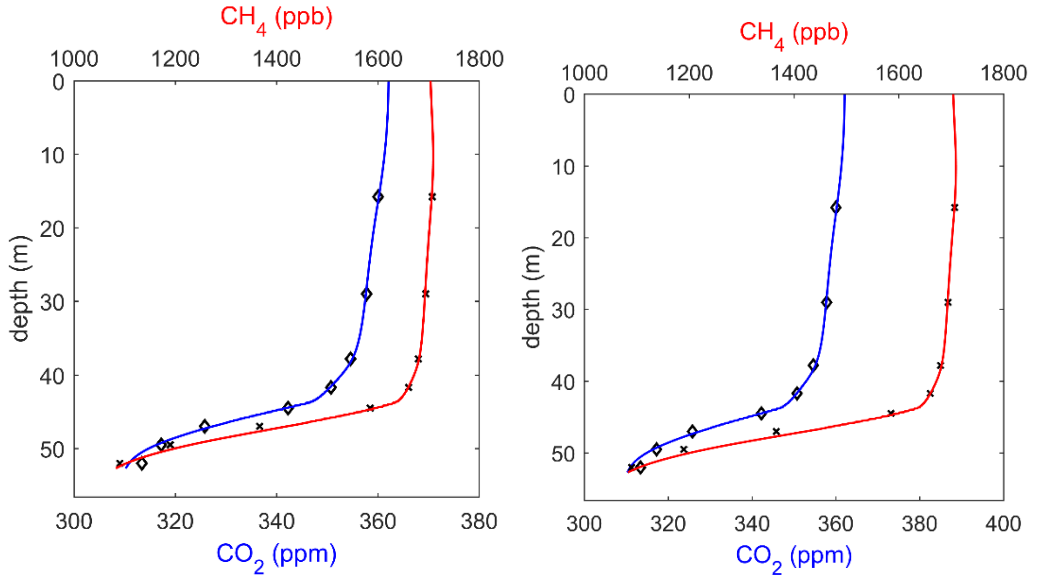

Figure ~~9~~10. Simulated CO2 and CH4 concentrations in the firn at Law Dome DSSW20K. The model is forced with histories of atmospheric CO_2 and CH_4 concentrations from 1800 to 1998 CE (the date of sampling). Markers indicate observed CO_2 (diamonds) and CH_4 (crosses) concentrations (Trudinger et al., 2002).

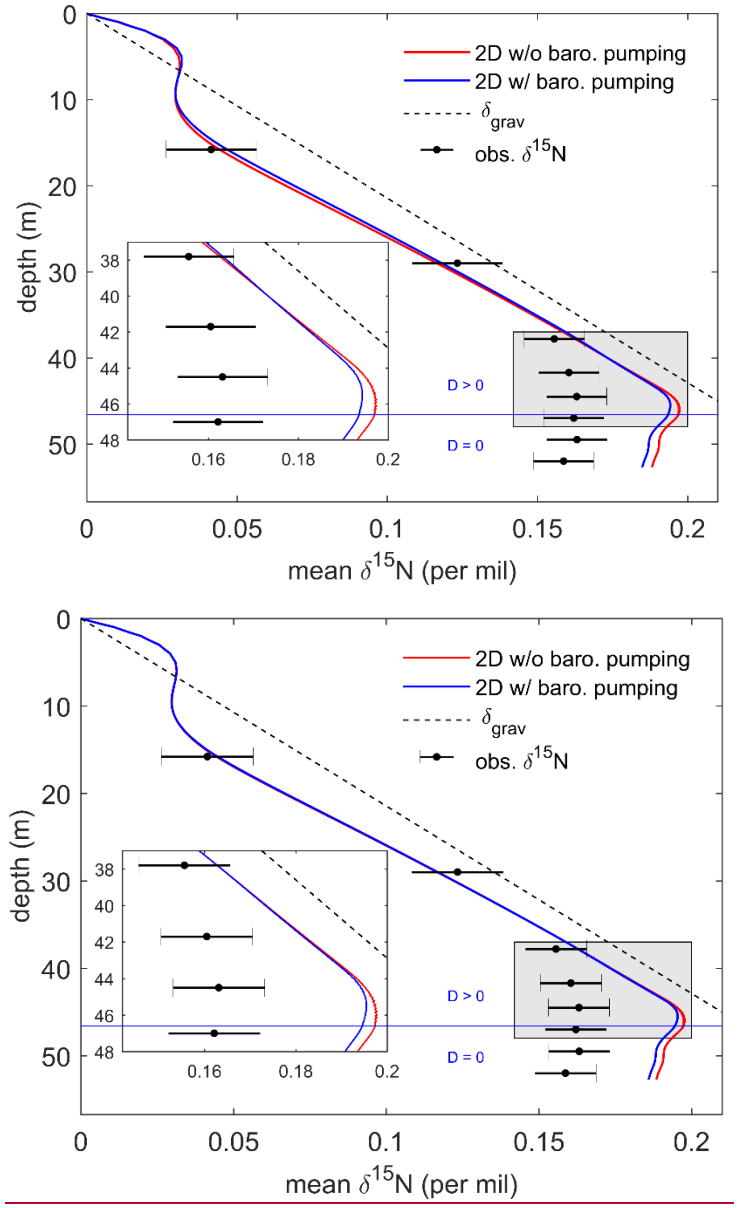

Figure 10~~11~~. Horizontally averaged δ^{15}N at Law Dome DSSW20K. The solid ~~blue and red~~ lines show the results of the 2D model (with layers), for the cases with (blue) and without (red) ~~including and excluding~~ barometric pumping~~, respectively~~. Black circles with error bars indicate the observed firn δ^{15}N (Trudinger et al., 2002, 2013). The dashed black line represents the equilibrium solution for pure gravitational settling (δ_{grav}). The horizontal blue line marks the depth where vertical diffusivity reaches zero. The ~~inlay~~ inset shows a magnification of the lock-in zone.

Simultaneously matching the δ^{15}N, CO_2 and CH_4 profile at Law Dome DSSW20K has proven difficult in the past (Trudinger et al., 2002; Buizert and Severinghaus, 2016). Simulated δ^{15}N in the LIZ is typically ~~significantly~~ substantially higher than in observations. Buizert and Severinghaus (2016) suggested that barometric pumping in the deep firn may be able to reconcile this contradiction. However, the mixing obtained from theoretical predictions was insufficient to ~~obtain the~~

~~anticipated results~~achieve a satisfactory fit. Buizert and Severinghaus (2016) hypothesized that firn layering may play a critical role in amplifying the impact of barometric pumping. ~~They~~ The authors used an idealized eddy and molecular diffusivity profile in the deep firn to simulate the effect of layers on firn air transport. Using these diffusivity profiles, they were able to obtain good agreement with observed $\delta^{15}N$, CH_4 and $^{14}CO_2$. Our 2D model includes an explicit representation of layering and places similar physical constraints on barometric pumping as the 1D model of Buizert and Severinghaus (2016). The model is tuned to optimize agreement with CO_2 and CH_4 and the patterns of both profiles are reproduced correctly (Fig. ~~10~~9). But the disagreement between modelled and observed $\delta^{15}N$ in the deep firn remains despite barometric pumping producing ~~significant~~ substantial non-fractionating dispersive mixing in the region (Fig. ~~11~~10). Simulated $\delta^{15}N$ values diverge from observations at ~38 m, where gravitational enrichment seems to stop in observations but continues in the model. ~~The~~ In contrast, the LIZ, as ~~indicated~~ defined by CO_2 and CH_4, ~~in contrast~~ only starts at roughly 43 m depth. Such an early onset of dispersive mixing is not supported by the dispersivity parameterization. However, only the longitudinal-to-flow mixing in the vertical direction at Siple Station was used to develop the firn dispersivity parameterization, and the use of this parameterization may be inappropriate at Law Dome DSSW20K (Buizert and Severinghaus, 2016). Moreover, dispersivity typically differs in the horizontal and vertical as well as the longitudinal- and the traverse-to-flow directions, an effect that is not accounted for in this study because of a lack of observational evidence to constrain anisotropic dispersivity.

4 Discussion

4.1 Differential kinetic isotope fractionation

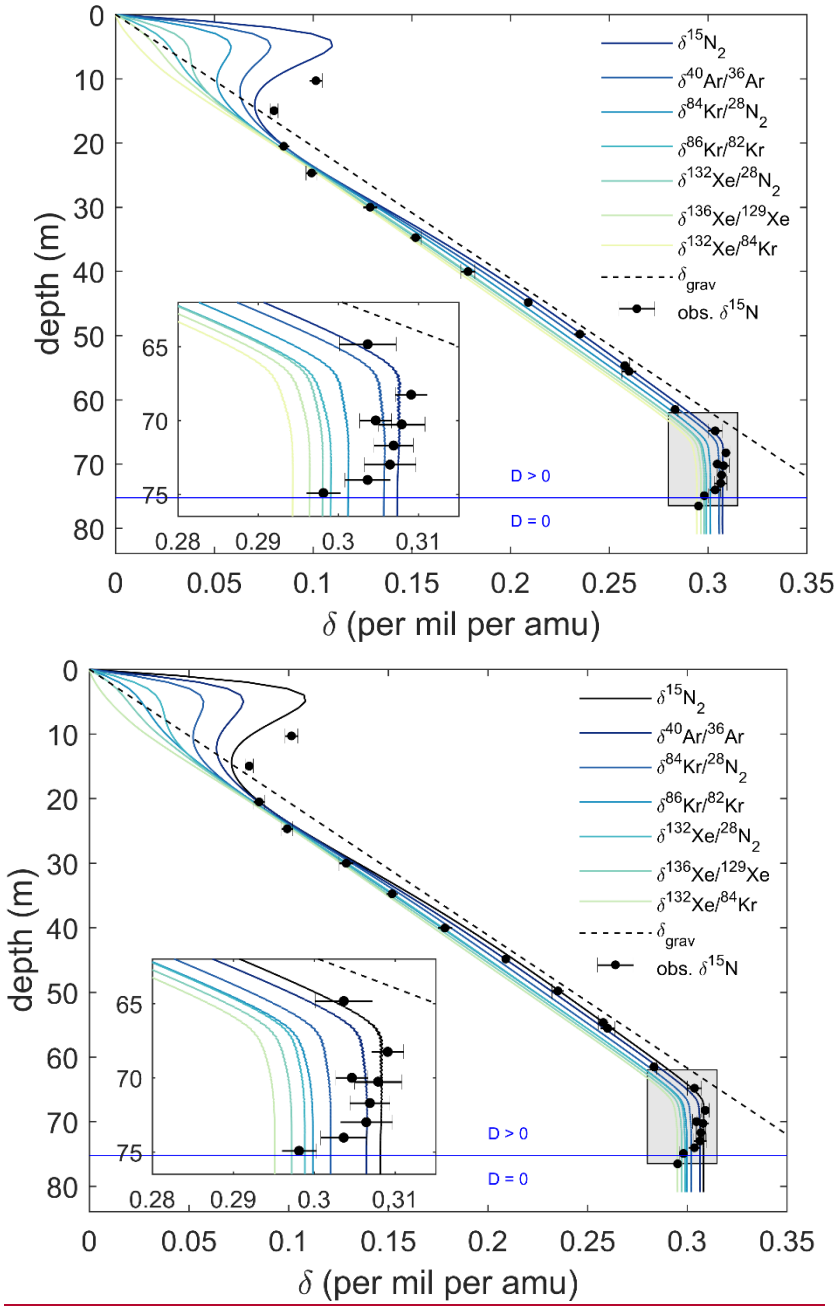

Figure 11~~12~~. Horizontally averaged isotope ratios at WAIS Divide in the 2D model including barometric pumping and horizontal layers. Isotope ratios are normalized to one atomic mass unit (amu~~, see SI~~) mass difference (SI ~~Sect. 6~~). The dashed black line represents the equilibrium solution for pure gravitational settling (δ_{grav}). The horizontal blue line marks the depth where vertical diffusivity reaches zero.

Observed $\delta^{15}N$ are shown as circles with horizontal error bars (Battle et al., 2011). The ~~inlay~~ inset shows a magnification of the lock-in zone (grey patch).

Isotope ratios in firn typically do not reach values as high as predicted from gravitational equilibrium due to the influence of advection and non-fractionating dispersive mixing (Trudinger et al., 1997; Kawamura et al., 2013; Buizert and Severinghaus, 2016). Advection and mass-independent mixing transport ~~less~~ less-fractionated air down in the firn column and act to counterbalance the enrichment of heavy isotopes by gravitational fractionation. As a result, ~~A~~all isotope ratios fall below the gravitational settling line δ_{grav} ~~in~~ (Fig. ~~12~~11) but ~~the magnitude of the deviation depends on the specific isotope pair. but the magnitude of the deviation depends on the specific isotope pair. This difference between the mass-normalized Kr and Ar isotope ratios has been termed ^{86}Kr excess (Buizert and Severinghaus, 2016). At the COD of WAIS Divide, simulated ^{86}Kr excess is ~5.6 per meg per amu in the 2D model with barometric pumping. This is significantly lower than the 7 – 22 per meg per amu values observed in the WAIS Divide ice core (Orsi A., personal communication).~~

The magnitude of disequilibrium of different isotope and elemental ratios is quantified ~~–~~here by defining the (mass-normalized) kinetic fractionation ϵ' relative to $\delta^{15}N$ ~~(ϵ')~~ (Kawamura et al., 2013) as

$$\epsilon'_{x/y} \equiv \frac{1}{1000 \times \Delta m_{x/y}} \ln\left(\frac{q_{x/28}}{q_{y/28}}\right) - \ln\left(q_{^{15}N}\right), \qquad \text{~~12~~(9)}$$

where $\Delta m_{x/y}$ is the mass difference of isotopes x and y. This definition is similar to the ^{86}Kr excess terminology introduced by Buizert and Severinghaus (2016) but ϵ' is given in the more precise $\ln(q)$-notation and uses $\delta^{15}N$ as ~~the~~ reference instead of $\delta^{40}Ar$/ $\delta^{36}Ar$. ~~Here,~~ To calculate $\epsilon'_{x/y}$, ~~i~~isotope ratios ~~are assumed to be~~must have been previously corrected for the influence of thermal fractionation either through combined Ar and N_2 measurements on firn air (Grachev and Severinghaus, 2003a, 2003b) or, as done here, by removing temperature effects with a suitable firn air transport model (Fig. ~~13~~12).

The degree of disequilibrium, represented by ϵ', ~~–~~ is caused by differential kinetic isotope fractionation. Heavy, slow-diffusing isotopes approach gravitational equilibrium more slowly than lighter, faster-diffusing isotopes. Therefore, slow-diffusing~~ratios of heavier~~ isotopes~~elements~~ ~~are more~~experience larger ~~susceptible to~~ kinetic ~~fractionatio~~fractionation (i.e., deviations from gravitational equilibrium) in regimes with non-zero advection or dispersion~~n~~. Consequently, ϵ' is more negative for heavier, slower diffusing isotopes. On its own, this ~~simple~~ rule of thumb cannot fully explain the pattern of ratios containing two different elements, such as $^{132}Xe/^{28}N_2$. The magnitude of disequilibrium in such mixed-element ratios is further discussed in Appendix B.

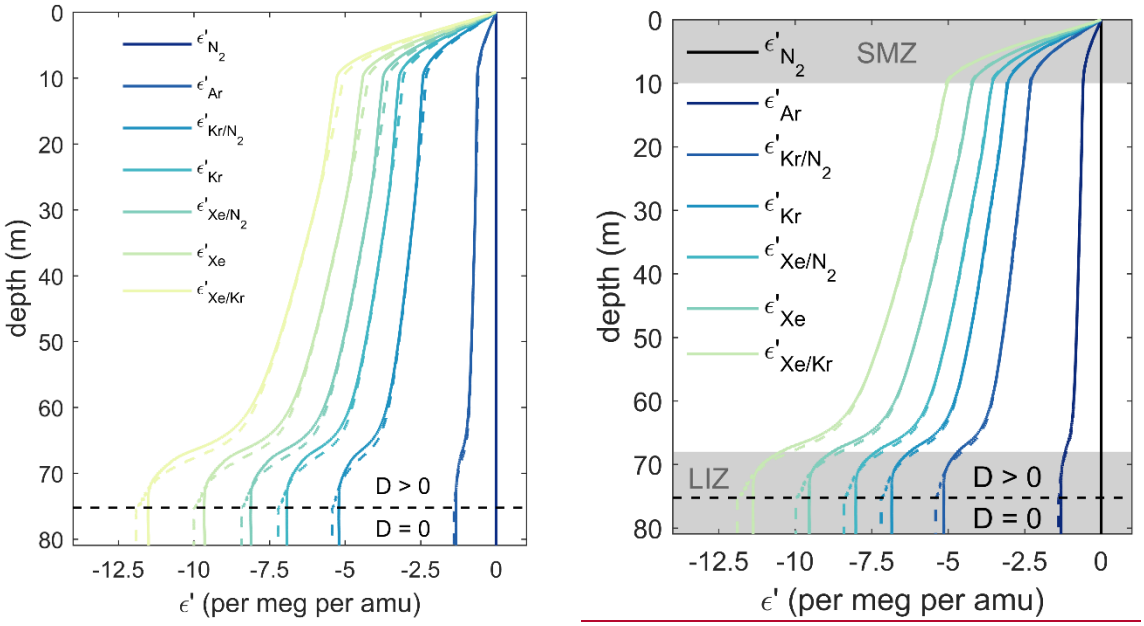

Figure 12~~13~~. Differential kinetic isotope fractionation (ϵ') profiles for different isotope pairs at WAIS Divide. Coloured solid and dashed lines show results from the 2D model with and without barometric pumping, respectively. $\epsilon'$is defined as the (typically negative) difference between any mass-normalized isotope ratio and $\delta^{15}N$ ~~as detailed in the~~(see text). Subscripts of one or two element names identify ratios as isotope or elemental ratios, respectively. The dashed black line highlights where molecular diffusivity in the model reaches zero.

In the DZ, ϵ' decreases almost linearly with depth, while within the ~~convective zone~~SMZ and ~~in the~~ LIZ ϵ' changes much more rapidly. Where molecular diffusivity is zero, ϵ' remains constant. This pattern is explained by the relative importance of advection and dispersive mixing compared to molecular diffusion in different regions of the firn column. The ~~vertical~~ Péclet number (Pe) traditionally quantifies the ratio of the advective to the diffusive transport and is here defined as the ratio of the diffusive to the advective time scale (τ_{D_m} and τ_{adv}). We~~Here we~~ add the time scale of dispersive mixing (τ_{D_e}) to the numerator because the effect of advection and dispersive mixing on the isotope profiles is very similar although the physics differ (Kawamura et al., 2013).

$$\mathrm{Pe} \equiv \frac{\tau_{adv} + \tau_{D_e}}{\tau_{D_m}} = \sim \frac{\frac{W}{L} + \frac{D_e}{L^2}}{\frac{\mathrm{D_m}}{L^2}} = \sim \frac{WL + D_e}{\mathrm{D_m}}, \qquad (10)$$

where $L = 1$ m is the characteristic length scale of firn air transport, and $\mathrm{D_m}$, W and D_e are characteristic values of the molecular diffusivity, the time mean vertical advection velocity, and the vertical dispersive or convective mixing at that depth, respectively.

This modifiede Péclet number ~~calculated in the model for the WAIS Divide~~ varies in the model by many orders of magnitude through the firn column at WAIS Divide with peak values in the ~~convective zone~~SMZ and the deep firn (Fig. ~~14~~13).

High modified Péclet numbers in the ~~convective zone~~SMZ are caused primarily by large D_e values, and high modified Péclet numbers in the LIZ are mostly the result of low molecular diffusivities. Kawamura et al. (2013) showed analytically that relative kinetic isotope fractionation depends on the ratio of eddy diffusivity to molecular diffusivity, but the role of advection was neglected due to near-zero accumulation rates at the Megadunes site. The absolute difference in kinetic isotope fractionation (i.e. ϵ') should be greatest when the product of the modified Péclet numbers of both isotopes is near one. In line with these theoretical predictions, we observe almost no further isotopic enrichment of $\delta^{15}N$ in the lock-in zone when barometric pumping is included in the model and Pe $\gg$ 1 (Figs. ~~8~~ 7 & ~~14~~13). The largest changes of ϵ' occur in the 2D model when the product of the modified Péclet numbers ~~the Péclet number~~ is within approximately 1-2 orders of magnitude of unity. ~~The~~ This region is illustrated by the vertical grey bar in Fig. ~~14~~13, which contains the ~~convective~~ SMZ~~zone~~ as well as the ~~region just above the~~beginning of the LIZ where non-fractionating mixing is of similar magnitude as molecular diffusion.

With active barometric pumping and centimetre-scale layering, the product of the modified Péclet numbers at the bottom of the LIZ becomes so large that ϵ' stops to decrease entirely in our model. If barometric pumping is neglected instead, the modified Péclet numbers in the layered 2D model are considerably lower in the LIZ and some gravitational and kinetic fractionation persists (i.e., $\delta^{15}N$ and ϵ' continue to change gradually). Therefore, barometric pumping leads to slightly weaker rather than stronger differential kinetic fractionation at the COD of WAIS Divide in contrast to expectations (Buizert and Severinghaus, 2016). Furthermore, ~~L~~layering and barometric pumping in the model seem to be insufficient to obtain the full ~5 – 23 per meg per amu range of~~extreme~~ ϵ'_{Kr} values ~~of ϵ'_{Kr} (or ^{86}Kr excess), observed~~ measured in the WAIS Divide ice core record~~.~~ (WAIS Divide Project Members, 2015; Bereiter et al., 2018). Instead, other, unresolved (i.e., subgrid-scale) processes may be the reason for the large observed disequilibrium. Establishing a straightforward relationship between disequilibrium and surface pressure variability using firn air models alone may not be possible without more observational data.~~ ^{86}Kr excess. For example, on the pore level, advective flows may be channelled into wider pores because the hydraulic conductance scales with the fourth power of the pore radius, whereas the diffusive conductance only depends on the square of the pore radius as indicated by the Hagen–Poiseuille equation (Buizert and Severinghaus, 2016). On small scales, Fick's law may also not be the correct relation to represent the physical process of diffusion. The mean square displacement in the disordered firn medium is not necessarily linearly depend on the product of diffusivity and time and we suggest other models of diffusion should be explored. Buizert and Severinghaus (2016) hypothesize that ^{86}Kr excess may be primarily produced by barometric pumping in the deep firn and could thus be used as a measure of paleo storminess in ice core records. Our findings suggest that establishing a straightforward relationship between ^{86}Kr excess and surface pressure variability using firn air models alone may not be possible without more observational data.

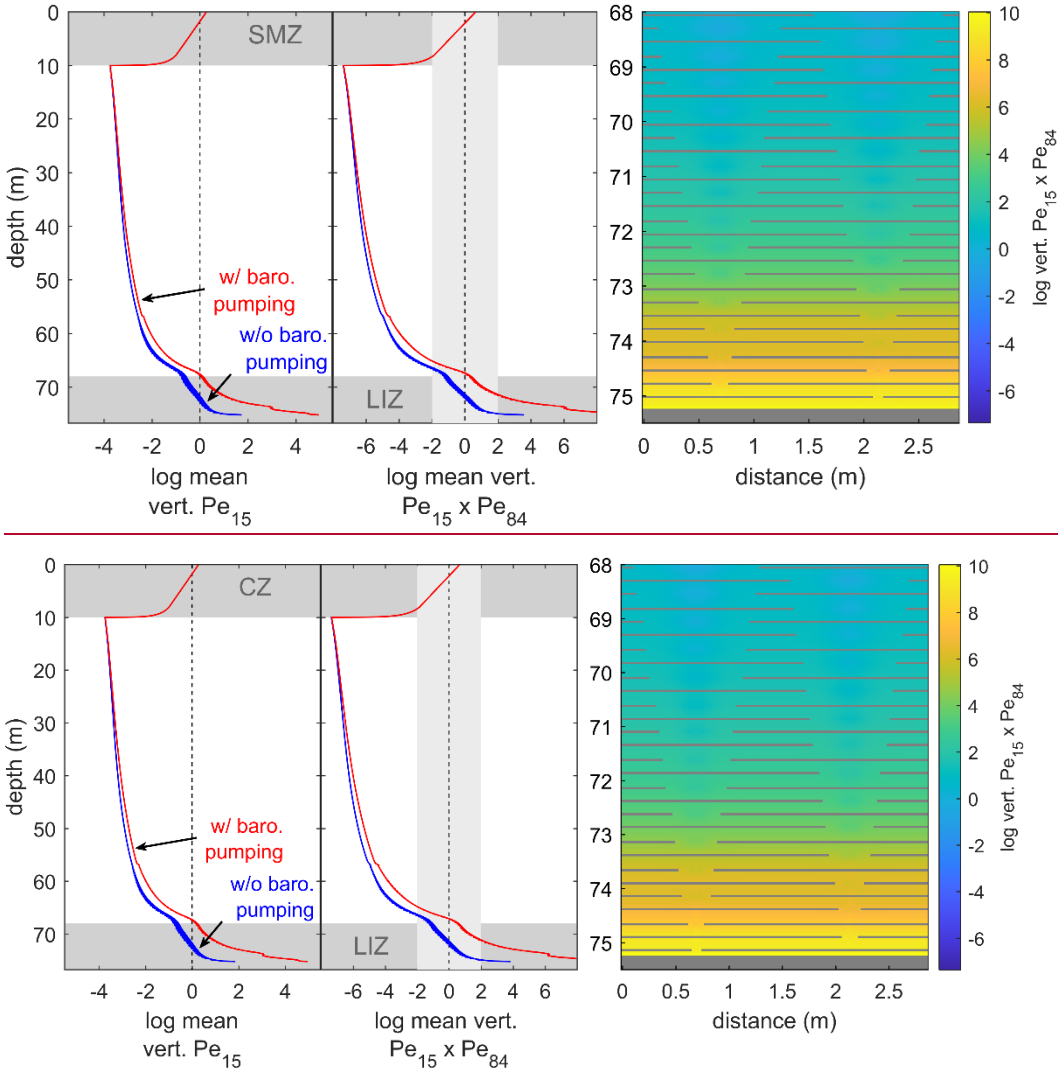

Figure 13~~14~~. The balance of fractionating and non-fractionating mixing at WAIS Divide. The left panel illustrates the horizontally averaged modified Péclet number of $\delta^{15}N$ (Pe_{15}, see text). Blue and red lines show results from the 2D models with and without barometric pumping. The strength of dispersive mixing in the calculations is given by the mean barometric pumping flow velocities at the site. The middle panel displays the product of the modified Péclet numbers for $\delta^{15}N$ and $^{84}Kr/^{28}N_2$ (Pe_{84}). The region where ϵ' changes with depth should be greatest (i.e., where the product of the modified Péclet numbers is near one) is highlighted by a grey bar. The right panel provides a magnified 2D map of this -Péclet number product in the LIZ. ~~Note that the Péclet number becomes infinite in the region below the COD and at layers where molecular diffusivities are zero. These regions are not considered when taking horizontal averages and are coloured grey in the right panel for illustratory purposes.~~

4.2 Diffusive fractionation

Strong kinetic isotope fractionation ~~was~~ can also be observed for trace gases that experience~~d~~ large changes in the atmospheric mixing ratio while the atmospheric isotope ratios remain~~ed~~ constant (Trudinger et al., 1997; Buizert et al., 2013). As the concentration of a trace gas increases, ~~the~~ isotopologues of the gas migrate into the firn column at different speeds because of

small differences in their masses and diffusivities. This results in a relative depletion of the slower diffusing isotopologue with depth called diffusive fractionation (Trudinger et al., 1997). During periods of abrupt CH_4 ~~release or sequestration~~change, diffusive fractionation commonly amounts to a relevant correction in ice core studies (Trudinger et al., 1997; Buizert et al., 2013). Diffusive fractionation of δ^{13}C-CH_4 is strong, and poorly constrained by models, to the degree that it prohibits the reliable atmospheric reconstruction of this parameter from firn air measurements (Sapart et al., 2013). Since ~~D~~diffusive fractionation is ~~another~~ a type of kinetic fractionation, it ~~and~~ can be tested in our model. We assume a constant atmospheric $^{13}C/^{12}C$ isotope ratio of 1.1147302 % for CO_2 (i.e., δ^{13}C-CO_2 = -8 ‰) and 1.0709052 % for CH_4 (i.e., δ^{13}C-CH_4 = -47 ‰), respectively. Thermal fractionation and gravitational settling are neglected to ~~highlight only~~isolate the impact of the atmospheric mixing ratio change. The model including barometric pumping calculates δ^{13}C-CO_2 and δ^{13}C-CH_4 values depleted by up to ~0.2 ‰ and ~~1.97~~2 ‰ relative to the atmosphere in the WAIS Divide LIZ at the time of firn air sampling (Fig. ~~15~~14). Without barometric pumping, delta values are notably higher because molecular diffusion is stronger, and the dispersive mixing no longer smoothes out the profile in the deep firn.

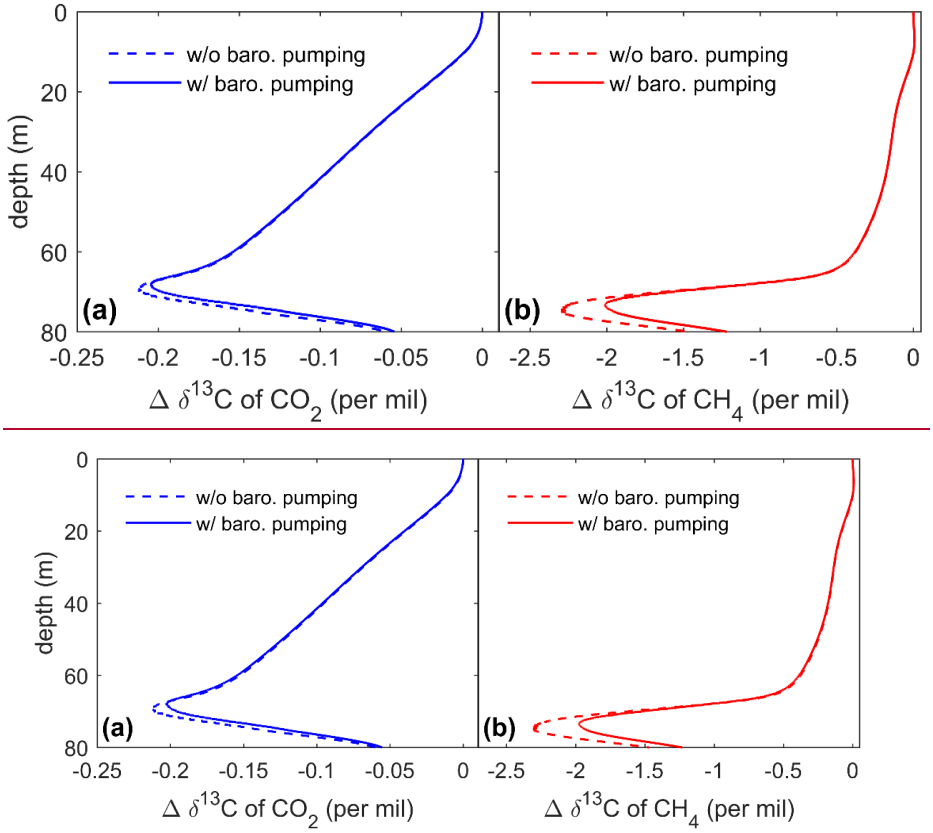

Figure ~~14~~15. Diffusive fractionation effect at the time of sampling at WAIS Divide on δ^{13}C of (a) CO_2 and (b) CH_4. Atmospheric mixing ratios of $^{12}CO_2$, $^{13}CO_2$, $^{12}CH_4$ and $^{13}CH_4$ were obtained from atmospheric trace gas histories used to drive the firn air model (see SI) and assuming constant atmospheric isotope ratios of -8 ‰ and -47 ‰ for δ^{13}C-CO_2 and δ^{13}C-CH_4, respectively. Firn air values are presented as the difference from the constant atmospheric isotope ratios.

4.3 Predicting disequilibrium

Past mean ocean temperature can be estimated from the noble gas concentrations in ice core bubbles (Headly and Severinghaus, 2007; Ritz et al., 2011; Bereiter et al., 2018). On glacial-interglacial timescales, ~~the~~ atmospheric concentrations of noble gases are ~~exclusively~~ primarily controlled by gas dissolution in the ocean. Because the temperature sensitivity of solubility is different for each gas, measurements of noble gas ratios in ice cores can be used to obtain a signal of integrated ocean temperature. However, as for any gas, the trace gas concentrations in bubbles must first be corrected for alterations of the atmospheric signal in the firn. In a recently published deglacial mean ocean temperature reconstruction, the WAIS Divide noble gas ice core record was corrected for gravitational fractionation and thermal fractionation using $\delta^{40}Ar/^{36}Ar$ measurements and a firn temperature gradient estimate (Bereiter et al., 2018). The authors further noted that different degrees of deviation from gravitational equilibrium (i.e., disequilibrium) can bias the gravitational fractionation correction applied to the raw noble gas record, which may lead to a cold bias of ~0.3°C in Holocene and LGM temperatures. Disequilibrium effects of -287.5 per meg for Kr/N_2, -833.3 per meg for Xe/N_2 and -545.7 per meg for Xe/Kr simulated by our model correspond to absolute temperature biases of 0.33 °C, 0.41 °C, and 0.45 °C, respectively, following the method of Bereiter et al. (2018). Because the magnitude of disequilibrium depends on firn properties and accumulation rate, glacial-interglacial changes in environmental boundary conditions may also affect the magnitude of disequilibrium in firn and thus the size of the relative deglacial temperature change estimated from noble gases.

In an attempt to compensate implicitly for disequilibrium effects and gravitational settling at the same time, it has been suggested that the elemental ratios Kr/N_2 and Xe/N_2 in bubbles should be corrected by subtracting krypton or xenon isotope ratios, respectively (Headly, 2008). ~~The hope is~~This would assume that krypton and xenon isotopes may be influenced similarly by the processes responsible for creating disequilibrium in Kr/N_2 and Xe/N_2. Therefore, this approach may compensate for disequilibrium effects and gravitational settling simultaneously, but it has been untested in models so far. The ϵ' values ~~modelled here~~ simulated here allow us to evaluate this method quantitatively. We use a linear fit to predict ~~the~~ ϵ'_{Kr/N_2} from ϵ'_{Kr}. The linear fit yields good agreement with the modelled ϵ'_{Kr} over the whole firn column (R^2>0.998), indicating that the scaling between ϵ' values is nearly independent of depth. We find that (mass-normalized) ϵ'_{Kr/N_2} should be approximately 75 % of ~~the~~ (mass-normalized) ϵ'_{Kr} at the WAIS Divide site. Scaling relationships for other isotope and element pairs are shown in Table 1 and are equally robust. Moreover, our results show that the source of disequilibrium is irrelevant ~~to~~ for the correction for the macroscopic processes represented in our model. Advection and convective or dispersive mixing show the same scaling relationships for ϵ'. At Law Dome DSSW20K, the calculated ratio of ϵ'_{Kr/N_2} and ϵ'_{Kr} is at 75.9 % almost identical to the result at WAIS Divide. Sensitivity tests with the 1D analytical model presented in Appendix A demonstrate that the disequilibrium scaling relationship between Kr isotopes and Kr/N_2 is robust to within $\pm$ 5~~%~~ % over a wide parameter range of molecular diffusivity, eddy diffusivity and advection velocity. Uncertainties become largest in the extreme case when ϵ'_{Ar}, the lowest simulated ϵ' value, is used to predict $\epsilon'_{Xe/Kr}$, the highest simulated ϵ' value, but they never exceed $\pm$ 25~~%~~ %.

This suggests that the same scaling relationship between ϵ'_{Kr/N_2} and ϵ'_{Kr} may be assumed to ~~be used~~hold ~~at~~ for any ~~firn sampling~~ice core site without introducing large biases. ϵ'_{Kr} and ϵ'_{Xe} from combined measurements of $\delta^{15}N$, $\delta^{86}Kr/^{82}Kr$ and $\delta^{136}Xe/^{129}Xe$ in ice cores could be used to predict the disequilibrium effects on noble elemental ratios (i.e., ϵ'_{Kr/N_2}, ϵ'_{Xe/N_2} and $\epsilon'_{Xe/Kr}$) and allows us to make a gas-specific gravitational correction. Although predicted ϵ'_{Kr} values at WAIS Divide are close to the current analytical uncertainty of the $^{86}Kr/^{82}Kr$ measurement, correcting for kinetic fractionation and disequilibrium will become advisable with future improvements in precision and may improve mean ocean temperature reconstructions.

Table 1. ϵ' scaling factor in the 2D model with barometric pumping between different element and isotope ratios from linear regression of ϵ' value pairs at all depths. $R^2 > 0.996$ for all relationships.

Predictor: isotope ratio	**Response: time-variable atmospheric gas ratios**		
	ϵ'_{Kr/N_2}	$\epsilon'_{Xe/Kr}$	ϵ'_{Xe/N_2}
ϵ'_{Ar}	3.94	8.74	6.16
ϵ'_{Kr}	0.75	1.66	1.17
ϵ'_{Xe}	0.54	1.19	0.84

5 Conclusions

We developed a two-dimensional firn air transport model that explicitly represents tortuosity in the firn column through migrating layers of reduced permeability. The idealized representation of firn layering is physically motivated and may illustrate the impact of firn density anomalies (i.e., summer vs winter firn or wind crusts) on gas transport. The model also accounts for thermal fractionation, a ~~convective~~ surface mixed zone, and surface pressure-forced barometric pumping. Dispersive mixing ~~resulting from~~as a result of barometric pumping is constrained in the model by previously published parameterizations and not subject to tuning. Simulations of the $\delta^{15}N$ profile at WAIS Divide show that extensive horizontal diffusion through the tortuous firn structure is required by the discontinuous layers. This limits the effective vertical diffusion of gases at depth. However, layering alone ~~cannot~~ does not fully prevent gravitational enrichment of isotopes in the deep firn ~~completely~~. Similarly, the effect of barometric pumping alone is insufficient to obtain agreement with observations. The combination of barometric pumping with layering, in contrast, leads to amplified dispersive mixing. This is due to high ~~by~~ velocity focusing in layer openings and leads to a more natural emergence of a lock-in zone in the model.

Previous studies have shown that d~~D~~ownward advection, convective mixing and dispersive mixing all hinder trace gases in reaching the isotope ratios expected from gravitational settling (e.g., Severinghaus et al., 2010; Kawamura et al., 2013; Buizert and Severinghaus, 2016;). K~~This k~~inetic fractionation is strongest for slow~~-~~ diffusing gases and increases with firn column ~~height~~depth. Our numerical experiments show ~~clearly~~ that barometric pumping leads to increased isotopic disequilibrium in the firn column. However, our simulations~~experiments~~ fail to account for the ~~large~~ full range of ^{86}Kr excess observed in the WAIS Divide core, as well as for the relatively weak $\delta^{15}N$ enrichment seen at DSSW20K, suggesting that these effects are not caused by the presence of layering (as previously suggested) and that their origin must be sought

elsewhere. We further find robust scaling relationships between the magnitude of disequilibrium in different noble gas isotope and elemental ratios. Our results suggest that, to first order, these scaling relationships are independent of depth in the firn column and independent of the reason for disequilibrium for the process represented in the model (i.e., dispersive mixing, advection or convective mixing). Thus, a correction that accounts for differential kinetic fractionation may be applied to measured observed noble gas ratios in the reconstruction of mean ocean temperature ~~to account for kinetic fractionation~~.

6 Appendices

6.1 Appendix A: An analytical solution for simplified firn air transport

Here, we seek an analytical solution to the following idealized scenario of firn air transport: firn air advection, diffusion, and dispersion in one dimension. In this case, vertical trace gas migration relative to the major gas nitrogen is governed by ~~the Eq. (A1):~~

$$\tilde{s}\frac{\partial q}{\partial t} = \frac{\partial}{\partial z}\left[\tilde{s}D_m\left(\frac{\partial q}{\partial z} - \frac{\Delta m\, g}{R\,T}q + \Omega\frac{\partial T}{\partial z}q\right) + \tilde{s}D_e\frac{\partial q}{\partial z}\right] - \tilde{s}w\frac{\partial q(z,t)}{\partial z}, \quad \text{(A1)}$$

with ~~$q \equiv \delta + 1$ the ratio of an isotope to 28N2 relative to a standard, $\tilde{s} \equiv s_{op}\exp\left(\frac{\Delta m g z}{RT}\right)$ the pressure – corrected open porosity (m3 m – 3), D_m~~ and D_e the molecular and eddy diffusivity (m² s^{-1})~~, Ω the thermal diffusion sensitivity (K^{-1}),~~ and w the effective vertical air advection velocity due to snow accumulation and pore compression (m s^{-1}) (e.g., Schwander et al., 1993; Rommelaere et al., 1997; Trudinger et al., 1997; Severinghaus et al., 2010; Buizert et al., 2012; Kawamura et al., 2013). The five terms on the right-hand side of Eq. (A1) represent Fickian diffusion, gravitational settling, thermal fractionation, mass-independent dispersion and gas advection (from left to right). A Dirichlet ~~(i.e., known value)~~ boundary condition is chosen at the top of the firn column and represents the well-mixed atmosphere (i.e., $q(0) \equiv 0$). The bottom boundary condition is given by a Neumann boundary condition allowing only an advective flux to leave the domain ($\tilde{s}(D_m + D_e)\frac{\partial q}{\partial z} - \tilde{s}D_m\left(\frac{\Delta m\, g}{R\,T} - \Omega\frac{\partial T}{\partial z}\right)q \equiv 0 \;@\; z = z(COD)$).

Assuming steady-state and neglecting changes of $\tilde{s}$, D_m, D_e and w with depth, Eq. (A1) reduces to (Severinghaus et al., 2010)

$$\frac{\partial q}{\partial t} \equiv 0 = (D_m + D_e)\frac{\partial^2 q}{\partial z^2} - D_m(G - \mathcal{T})\frac{\partial q}{\partial z} - w\frac{\partial q}{\partial z}, \quad \text{(A2)}$$

where $G \equiv \frac{\Delta m\, g}{R\,T}$ and $\mathcal{T} \equiv \Omega\frac{\partial T}{\partial z}$ represent the constants in the gravitational and thermal fractionation term.

The solution to Eq. (A2) ~~for~~ yields trace gas profiles above the COD in delta notation ~~takes the form~~

$$\delta = \frac{\exp\left(\frac{D_m(G-\mathcal{T})+w}{D_m+D_e}\,z\right)-1}{\frac{w}{D_m(G-\mathcal{T})}\exp\left(\frac{D_m(G-\mathcal{T})+w}{D_m+D_e}\,z_{COD}\right)+1} \begin{cases} \dfrac{\exp\left(\frac{D_m(G-\mathcal{T})+w}{D_m+D_e}\,z\right)-1}{\frac{w}{D_m(G-\mathcal{T})}\exp\left(\frac{D_m(G-\mathcal{T})+w}{D_m+D_e}\,z_{COD}\right)+1}, & z \le z_{COD} \\ \delta(z_{COD}), & z > z_{COD} \end{cases} \quad \text{(A3)}$$

where $z_{COD} = z(COD)$ (see SI Fig. S2). δ values below the COD are constant. Note that Eq. (A2) only applies to trace gas transport into N_2, not to transport of one trace gas into another trace gas, as discussed in the text. Nevertheless Because $\delta^{15}N$ only requires calculating the transport of the trace gas $^{15}N^{14}N$ into the major gas $^{28}N_2$, the equation can be used as such is to calculate $\delta^{15}N$.

By evaluating some extreme cases, Eq. (A4A3) illustrates a few key points about trace gas transport of $\delta^{15}N$ in firn. Under a large negative temperature gradient (i.e., atmospheric warming, $\mathcal{T} \to -\infty$), $\delta \to \infty$ and thermally sensitive gases are enriched in the firn because the numerator grows faster than the denominator. Similarly, heavier gases ($G \to \infty$) are more strongly fractionated ($\delta \to \infty$) than lighter gases assuming they have the same molecular diffusivity. Advection ($w \to \infty$) and eddy mixing ($D_e \to \infty$) prevent the system from reaching the trace gas concentrations expected from gravitational settling and ultimately force concentrations to be constant ($\delta \to 0$). A lack of molecular diffusion ($D_m \to 0$) leads to the same result ($\delta \to 0$). Naturally, Eq. (A4A3) reduces to the profile of a gravitationally settled gas (i.e., Eq. (1)) when $w \to 0$ and $D_e \to 0$.

6.2 Appendix B: Differential kinetic isotope fractionation in ratios of two different elements

Here we revisit the relative disequilibrium for ratios of two elements as seen in Figs. 12 11 and 1312. First, recall the definition of ϵ' for a ratio of isotopes x and y (indicated by their nominal atomic masses)

$$\epsilon'_{x/y} \equiv \frac{10^{-3}}{m_x - m_y}\ln(q_{x/y}) - \ln(q_{29/28}) = \ln\left(\frac{q_{x/y}^{\frac{10^{-3}}{m_x-m_y}}}{q_{29/28}}\right). \quad \text{(A4)}$$

Equation (3) shows that $q_{x/y}$ is the ratio of q values calculated for the transport of each isotope into $^{28}N_2$ ($q_{x/28}$ and $q_{y/28}$). $q_{x/28}$ (or $q_{y/28}$) may also be expressed in reference to nitrogen using the ϵ' value for the isotope

$$\frac{10^{-3}}{m_x - m_{28}}\ln(q_{x/28}) = \ln(q_{29/28}) + \epsilon'_{x/28} \quad \rightarrow \quad q_{x/28} = \left(q_{29/28}\cdot\exp(\epsilon'_{x/28})\right)^{10^3(m_x-m_{28})} \ln\left(q_{x/28}^{\frac{1}{m_x-m_{28}}}\right) \quad \text{(A5)}$$

$$= \ln(q_{29/28}) + \epsilon'_{x/28} = \ln\left(q_{29/28}\cdot\exp(\epsilon'_{x/28})\right).$$

Note that ϵ' by definition is already mass-normalized. It follows from Eqs. (3), (A4) and (A5) that

$$\epsilon'_{x/y} = \ln\left(\frac{\left(\frac{q_{x/28}}{q_{y/28}}\right)^{\frac{10\text{^}-3}{m_x-m_y}}}{q_{29/28}}\right) = \ln\left(\frac{\left(\frac{\left(q_{29/28}\cdot\exp(\epsilon'_{x/28})\right)^{m_x-m_{28}}}{\left(q_{29/28}\cdot\exp(\epsilon'_{y/28})\right)^{m_y-m_{28}}}\right)^{\frac{1}{m_x-m_y}}}{q_{29/28}}\right). \quad \text{(A6)}$$

Equation (A6) may be rewritten to yield

$$\epsilon'_{x/y} = \frac{m_x-m_{28}}{m_x-m_y}\left[\ln(q_{29/28}) + \epsilon'_{x/28}\right] - \frac{m_y-m_{28}}{m_x-m_y}\left[\ln(q_{29/28}) + \epsilon'_{x/28}\right] - \ln(q_{29/28}). \quad \text{(A7)}$$

Because the terms containing $q_{29/28}$ cancel, we obtain a straightforward expression to find ϵ' for any isotope ratio from the ϵ' of two nuclides relative to $^{28}N_2$

$$\epsilon'_{x/y} = \frac{m_x - m_{28}}{m_x - m_y}\epsilon'_{x/28} - \frac{m_y - m_{28}}{m_x - m_y}\epsilon'_{y/28}. \quad \text{(A8)}$$

Analysis of this relationship reveals that disequilibrium should most strongly affect ratios of two heavy isotopes, such as $^{132}Xe/^{84}Kr$, because heavy elements diffuse slower than N_2 (i.e., $\epsilon'_{x/28} \ll 0$) and the mass weighting factor is larger in the first than in the second term (i.e., $\frac{m_x-m_{28}}{m_x-m_y} \gg \frac{m_y-m_{28}}{m_x-m_y}$). ~~As long as no explicit correction for disequilibrium effects is implemented in the determination of mean ocean temperature, this implies that particular caution should be used in interpreting the $^{132}Xe/^{84}Kr$ record at sites with substantial disequilibrium.~~

Although this equation can theoretically predict ϵ' of any isotope ratio from ϵ' of the two isotopes x and y relative to $^{28}N_2$ (i.e., $\epsilon'_{x/28}$ and $\epsilon'_{y/28}$), in practice, this approach will not allow correcting for differential kinetic isotope fractionation. $\epsilon'_{x/28}$ cannot be measured directly and the atmospheric ratio of the noble gas x to nitrogen is not constant over long timescales. Thus, $\epsilon'_{x/28}$ will not only be affected by disequilibrium but will also be influenced by atmospheric variability resulting from gas specific solubility differences (i.e., precisely the mean ocean temperature signals we attempt to reconstruct). Instead we suggest that the scaling relationships provided in Sect. 5.3 can be used to predict the ϵ' of noble gas elemental ratios.

7 Competing interests

The authors declare that they have no conflict of interest.

8 Acknowledgements

We would like to thank Jakob Keck, Alan Seltzer and Ian Eisenman for providing computational resources and insightful discussions on the numerical implementation of firn air transport. Sarah Shackleton has provided helpful comments on the

importance of disequilibrium in mean ocean temperature reconstruction. This work was supported by NSF grants PLR-1543229 and PLR-1543267.

9 References

Alley, R. B. and Koci, B. R.: Recent warming in central Greenland?, Annals of Glaciology, 14, 6–8, 1990.

Battle, M. O., Severinghaus, J. P., Sofen, E. D., Plotkin, D., Orsi, A. J., Aydin, M., Montzka, S. A., Sowers, T. and Tans, P. P.: Controls on the movement and composition of firn air at the West Antarctic Ice Sheet Divide, Atmospheric Chemistry and Physics, 11, 11007–11021, doi:10.5194/acp-11-11007-2011, 2011.

Bereiter, B., Shackleton, S., Baggenstos, D., Kawamura, K. and Severinghaus, J.: Mean global ocean temperatures during the last glacial transition, Nature Publishing Group, 553, 39–44, doi:10.1038/nature25152, 2018.

Buizert, C. and Severinghaus, J. P.: Dispersion in deep polar firn driven by synoptic-scale surface pressure variability, The Cryosphere, 10, 2099–2111, doi:10.5194/tc-2016-148, 2016.

Buizert, C., Martinerie, P., Petrenko, V. V, Severinghaus, J. P., Trudinger, C. M., Witrant, E., Rosen, J. L., Orsi, A. J., Rubino, M., Etheridge, D. M., Steele, L. P., Hogan, C., Laube, J. C., Sturges, W. T., Levchenko, V. A., Smith, A. M., Levin, I., Conway, T. J., Dlugokencky, E. J., Lang, P. M., Kawamura, K., Jenk, T. M., White, J. W. C., Sowers, T., Schwander, J. and Blunier, T.: Gas transport in firn: Multiple-tracer characterisation and model intercomparison for NEEM, Northern Greenland, Atmospheric Chemistry and Physics, 12, 4259–4277, doi:10.5194/acp-12-4259-2012, 2012.

Buizert, C., Sowers, T. and Blunier, T.: Assessment of diffusive isotopic fractionation in polar firn, and application to ice core trace gas records, Earth and Planetary Science Letters, 361, 110–119, doi:10.1016/j.epsl.2012.11.039, 2013.

Colbeck, S. C.: Air Movement in Snow due to Windpumping, Journal of Glaciology, 35(120), 209–213, 1989.

Craig, H., Horibe, Y. and T., S.: Gravitational separation of gases and isotopes in polar ice caps, Science, 242, 1675–1678, 1988.

Dahl-Jensen, D., Morgan, V. I. and Elcheikh, A.: Monte Carlo inverse modelling of the Law Dome (Antarctica) temperature profile, Annals of Glaciology, 29, 145–150, doi:10.3189/172756499781821102, 1999.

Darcy, H.: Les Fontaines Publiques de la Ville de Dijon, Victor Dalmont, Paris., 1856.

Dlugokencky, E. J., Lang, P. M., Mund, J. W., Crotwell, A. M., Crotwell, M. J. and Thoning, K. W.: Atmospheric Carbon Dioxide Dry Air Mole Fractions from the NOAA ESRL Carbon Cycle Cooperative Global Air Sampling Network, 1968-2015, Version: 2016-08-30, 2016a.

Dlugokencky, E. J., Lang, P. M., Crotwell, A. M., Mund, J. W., Crotwell, M. J. and Thoning, K. W.: Atmospheric Methane Dry Air Mole Fractions from the NOAA ESRL Carbon Cycle Cooperative Global Air Sampling Network, 1983-2015, Version: 2016-07-07, 2016b.

Etheridge, D. M., Steele, L. P., Langenfelds, R. L., Francey, R. J., Barnola, J. M. and Morgan, V. I.: Natural and anthropogenic changes in atmospheric CO2 over the last 1000 years from air in Antarctic ice and firn, Journal of Geophysical

Research-Atmospheres, 101(D2), 4115–4128, doi:10.1029/95JD03410, 1996.

Etheridge, D. M., Steele, L. P., Francey, R. J. and Langenfelds, R. L.: Atmospheric methane between 1000 A.D. and present: Evidence of anthropogenic emissions and climatic variability, Journal of Geophysical Research, 103(D13), 15979, doi:10.1029/98JD00923, 1998.

Freeze, R. A. and Cherry, J. A.: Groundwater, Prentice-Hall, Inc., Englewood Cliffs, New Jersey., 1979.

Grachev, A. and Severinghaus, J. P.: Laboratory determination of thermal diffusion constants for 29N2 /28N2 in air at temperatures from -60 to 0° C for reconstruction of magnitudes of abrupt climate changes using the ice core fossil – air paleothermometer, Geochimica et cosmochimica Acta, 67(3), 345–360, 2003a.

Grachev, A. M. and Severinghaus, J. P.: Determining the Thermal Diffusion Factor for 40Ar/ 36Ar in Air To Aid Paleoreconstruction of Abrupt Climate Change, The Journal of Physical Chemistry A, 107, 4636–4642, doi:10.1021/jp027817u, 2003b.

Headly, M.: Krypton and xenon in air trapped in polar ice cores: paleo-atmospheric measurements for estimating past mean ocean temperature and summer snowmelt frequency, University of California, San Diego., 2008.

Headly, M. A. and Severinghaus, J. P.: A method to measure Kr/N2 ratios in air bubbles trapped in ice cores and its application in reconstructing past mean ocean temperature, Journal of Geophysical Research, 112(D19105), 1–12, doi:10.1029/2006JD008317, 2007.

Hörhold, M. W., Laepple, T., Freitag, J., Bigler, M., Fischer, H. and Kipfstuhl, S.: On the impact of impurities on the densification of polar firn, Earth and Planetary Science Letters, 325–326, 93–99, doi:10.1016/j.epsl.2011.12.022, 2012.

Johnsen, S. J.: Stable isotope profiles compared with temperature profiles in firn with historical temperature records, Isotopes and Impurities in Snow and Ice, 388–392, 1977.

Kawamura, K., Severinghaus, J. P., Albert, M. R., Courville, Z. R., Fahnestock, M. A., Scambos, T. A., Shields, E. and Shuman, C. A.: Kinetic fractionation of gases by deep air convection in polar firn, Atmospheric Chemistry and Physics, 13, 11141–11155, doi:10.5194/acp-13-11141-2013, 2013.

Keeling, C. D., Stephen, C., Piper, S. C., Bacastow, R. B., Wahlen, M., Whorf, T. P., Heimann, M. and Meijer, H. A.: Exchanges of atmospheric CO2 and 13CO2 with the terrestrial biosphere and oceans from 1978 to 2000., Global Aspects, SIO Reference Series. Scripps Institution of Oceangraphy, San Diego, 01–06, 83–113, doi:10.1007/b138533, 2001.

Lazzara, M. A., Weidner, G. A., Keller, L. M., Thom, J. E. and Cassano, J. J.: Antarctic Automatic Weather Station Program: 30 Years of Polar Observation, Bulletin of the American Meteorological Society, 93, 1519–1537, doi:10.1175/BAMS-D-11-00015.1, 2012.

Lüthi, D., Le Floch, M., Bereiter, B., Blunier, T., Barnola, J.-M., Siegenthaler, U., Raynaud, D., Jouzel, J., Fischer, H., Kawamura, K. and Stocker, T. F.: High-resolution carbon dioxide concentration record 650,000-800,000 years before present., Nature, 453, 379–382, doi:10.1038/nature06949, 2008.

Mitchell, L. E., Buizert, C., Brook, E. J., Breton, D. J., Fegyveresi, J., Baggenstos, D., Orsi, A., Severinghaus, J., Alley, R. B., Albert, M., Rhodes, R. H., McConnell, J. R., Sigl, M., Maselli, O., Gregory, S. and Ahn, J.: Observing and modeling the

influence of layering on bubble trapping in polar firn, Journal of Geophysical Research Atmospheres, 120, 2558–2574, doi:10.1002/2014JD022766, 2015.

Van Ommen, T. D., Morgan, V. I., Jacka, T. H., Woon, S. and Elcheikh, A.: Near-surface temperatures in the Dome Summit South (Law Dome, East Antarctica) borehole, Annals of Glaciology, 29, 141–144, doi:doi:10.3189/172756499781821382, 1999.

Orsi, A. J., Cornuelle, B. D. and Severinghaus, J. P.: Little Ice Age cold interval in West Antarctica: Evidence from borehole temperature at the West Antarctic Ice Sheet (WAIS) Divide, Geophysical Research Letters, 39(L09710), 1–7, doi:10.1029/2012GL051260, 2012.

Orsi, A. J., Kawamura, K., Fegyveresi, J. M., Headly, M. A., Alley, R. B. and Severinghaus, J. P.: Differentiating bubble-free layers from Melt layers in ice cores using noble gases, Journal of Glaciology, 61(227), 585–594, doi:10.3189/2015JoG14J237, 2015.

Petit, R. J., Jouzel, J., Raynaud, D., Barkov, N. I., Barnola, J.-M., Basile, I., Bender, M., Chappellaz, J., Davis, M., Delaygue, G., Delmotte, M., Kotyakov, V. M., Legrand, M., Livenkov, V. Y., Lorius, C., Pépin, L., Ritz, C., Saltzman, E. and Stievenard, M.: Climate and atmospheric history of the past 420,000 years from the Vostok ice core, Antarctica, Nature, 399, 429–413, doi:10.1038/20859, 1999.

Ritz, S. P., Stocker, T. F. and Severinghaus, J. P.: Noble gases as proxies of mean ocean temperature: Sensitivity studies using a climate model of reduced complexity, Quaternary Science Reviews, 30, 3728–3741, doi:10.1016/j.quascirev.2011.09.021, 2011.

Rommelaere, V., Arnaud, L. and Barnola, J.-M.: Reconstructing recent atmospheric trace gas concentrations from polar firn and bubbly ice data by inverse methods, Journal of Geophysical Research, 102(D25), 30069–30083, 1997.

Sapart, C. J., Martinerie, P., Witrant, E., Chappellaz, J., Van De Wal, R. S. W., Sperlich, P., Van Der Veen, C., Bernard, S., Sturges, W. T., Blunier, T., Schwander, J., Etheridge, D. and Röckmann, T.: Can the carbon isotopic composition of methane be reconstructed from multi-site firn air measurements?, Atmospheric Chemistry and Physics, 13, 6993–7005, doi:10.5194/acp-13-6993-2013, 2013.

Schwander, J.: The Transformation of Snow to Ice and the Occlusion of Gases, The Environmental Record in Glaciers and Ice Sheets, 53–67, 1989.

Schwander, J., Stauffer, B. and Sigg, A.: Air mixing in firn and the age of the air at pore close-off, Annals of Glaciology, 10, 141–145, 1988.

Schwander, J., Barnola, J.-M., Andrié, C., Leuenberger, M., Ludin, A., Raynaud, D. and Stauffer, B.: The age of the air in the firn and the ice at Summit, Greenland, Journal of Geophysical Research, 98, 2831–2838, doi:10.1029/92JD02383, 1993.

Severinghaus, J. P. and Battle, M. O.: Fractionation of gases in polar ice during bubble close-off: New constraints from firn air Ne, Kr and Xe observations, Earth and Planetary Science Letters, 244, 474–500, doi:10.1016/j.epsl.2006.01.032, 2006.

Severinghaus, J. P., Grachev, A. and Battle, M.: Thermal fractionation of air in polar firn by seasonal temperature gradients, Geochemistry, Geophysics, Geosystems, 2(2000GC000146), 1–24, doi:10.1029/2000GC000146, 2001.

Severinghaus, J. P., Albert, M. R., Courville, Z. R., Fahnestock, M. A., Kawamura, K., Montzka, S. A., Mühle, J., Scambos, T. A., Shields, E., Shuman, C. A., Suwa, M., Tans, P. and Weiss, R. F.: Deep air convection in the firn at a zero-accumulation site, central Antarctica, Earth and Planetary Science Letters, 293, 359–367, doi:10.1016/j.epsl.2010.03.003, 2010.

Sowers, T., Bender, M. and Raynaud, D.: Elemental and Isotopic Composition of Occluded O2 and N2 in Polar Ice, Journal of Geophysical Research, 94(D4), 5137–5150, doi:10.1029/JD094iD04p05137, 1989.

Trudinger, C. M., Enting, I. G., Etheridge, D. M., Francey, R. J., Levchenko, V. A., Steele, L. P., Raynaud, D. and Arnaud, L.: Modeling air movement and bubble trapping in firn, Journal of Geophysical Research: Atmospheres, 102(D6), 6747–6763, doi:10.1029/96JD03382, 1997.

Trudinger, C. M., Etheridge, D. M., Rayner, P. J., Enting, I. G., Sturrock, G. A. and Langenfelds, R. L.: Reconstructing atmospheric histories from measurements of air composition in firn, Journal of Geophysical Research Atmospheres, 107(24), 1–13, doi:10.1029/2002JD002545, 2002.

Trudinger, C. M., Enting, I. G., Rayner, P. J., Etheridge, D. M., Buizert, C., Rubino, M., Krummel, P. B. and Blunier, T.: How well do different tracers constrain the firn diffusivity profile?, Atmospheric Chemistry and Physics, 13, 1485–1510, doi:10.5194/acp-13-1485-2013, 2013.

WAIS Divide Project Members: Precise interpolar phasing of abrupt climate change during the last ice age, Nature, 520, 661–665, doi:10.1038/nature14401, 2015.

Weller, G. and Schwerdtfeger, P.: Thermal properties and heat transfer processes of low-temperature snow, in Meteorological Studies at Plateau Station, Antarctica, vol. 25, edited by P. C. Dalrymple, A. J. Riordan, A. Riordan, A. J. Riordan, and R. C. L. andUwe R. Weller, H. H. Lettau, H. Lettau, L. A. Stroschein, L. S. Kundla, Leander A. Stroschein, M. Kuhn, Peter Schwerdtfeger, American Geophysical Union., 1977.